Inaugural dissertation

for

obtaining the doctoral degree

of the

Combined Faculty of Mathematics, Engineering and Natural Sciences

of the

Ruprecht - Karls - University

Heidelberg

Presented by

Philipp Willnow, M.Sc.

Born in: Dallas, TX (USA)

Oral examination:

Nuclear positioning and a non-uniform metabolism exert epigenetic control of gene expression in the wing disc

Referees:

Prof. Dr. Michael Boutros

Prof. Dr. Aurelio Teleman

Table of Contents

List of Figures

List of Tables

Summary

In my PhD project, I used the pseudostratified epithelium of the wing imaginal disc of *Drosophila melanogaster* as a model system to study the significance of cellular metabolism and nuclear positioning for tissue development *in vivo*. The wing disc is a larval precursor tissue that mainly gives rise to the adult wing. It is surrounded by the larval hemolymph, providing metabolites, such as lipoprotein-bound lipids. As a read-out for the metabolic state of the wing disc, I investigated the disc epigenome as most histone modifying and de-modifying enzymes require metabolic co-factors or substrates. In this study, I identified a non-uniform distribution of histone acetylation in the wing disc with high acetylation levels specifically in nuclei facing the tissue surface. This rim pattern is not defined by cell cycle or cellular identity but by the position of the nucleus within the tissue. Accordingly, genetic ablation of the disc rim causes the formation of a new rim with high histone acetylation in the remaining, now outward facing, tissue region. High acetylation levels in nuclei in the disc rim correlate with hemolymph-exposure as indicated by accumulation of lipoproteins on outward-facing membranes. The acetylation pattern persists during wing disc development suggesting a continuous regulatory role in tissue growth. The non-uniform distribution of histone acetylation is achieved by local activity of the acetyltransferase nejire in the rim of the disc. Spatially restricted nejire activity in the rim is not determined by non-uniform intrinsic activity or expression of the enzyme but by local availability of its metabolic substrate acetyl-CoA. Required acetyl-CoA is specifically generated in outward-facing nuclei due to increased levels of nuclear acetyl-CoA synthase which converts acetate to acetyl-CoA. Metabolically, this rim acetylation pattern depends on acetate derived from fatty acid β-oxidation, which is also non-uniform and increased in the rim of the wing disc, as evidenced by a high mitochondrial membrane potential in this tissue region. Rim histone acetylation epigenetically impacts expression of genes in the wing disc implicated in developmentally important signaling pathways, including Hippo, Notch, and Hedgehog. Jointly, my findings suggest a novel role for nuclear positioning and a concordantly aligned metabolism in determining cell fate and, consequently, wing disc development.

Zusammenfassung

In meiner Doktorarbeit habe ich die Flügelimaginalscheibe der Fruchtfliege *Drosophila melanogaster* als Modelsystem benutzt, um die regulatorische Rolle des zellulären Stoffwechsels und der Positionierung des Zellkerns in der Gewebeentwicklung *in vivo* zu untersuchen. Die Flügelimaginalscheibe ist ein pseudostratifiziertes Epithel, das während der Metamorphose im Wesentlichen den Flügel des adulten Tieres bildet. In der Larve ist die Imaginalscheibe von der Hämolymphe umgeben, welche wichtige Metabolite, wie lipidbeladene Lipoproteine, bereitstellt. Zur Charakterisierung des zellulären Stoffwechsels habe ich das Epigenom der Imaginalscheibe untersucht, da die meisten Histon-modifizierenden Enzyme metabolische Kofaktoren und Substrate für ihre Aktivität benötigen. In diesen Untersuchungen konnte ich eine nicht uniforme Verteilung der Histonacetylierung in der Flügelimaginalscheibe dokumentieren. Dieses nicht uniforme Muster zeichnet sich durch erhöhte Histonacetylierung in Zellkernen aus, die der Gewebsoberfläche zugewandt sind. Dieses Randmuster wird nicht durch Zellzyklus oder Zellidentität, sondern durch die Position des Zellkerns im Gewebe bestimmt. Entsprechend führt der genetisch induzierte Verlust des Randgewebes zur Bildung eines neuen Randes mit hoher Histonacetylierung in der verbleibenden nun außen liegenden Gewebsregion. Die Position der Kerne mit hoher Histonacetylierung korreliert mit deren Exposition mit Hämolymphe, was durch die Anreicherung von Lipoproteinen an nach außen gerichteten Zellmembranen deutlich wird. Dieses Randmuster bleibt während der Entwicklung der Flügelimaginalscheibe erhalten, was auf eine kontinuierliche regulatorische Rolle im Gewebewachstum schließen lässt. Das nicht uniforme Histonacetylierungsmuster entsteht auf Grund lokaler Aktivität der Acetyltransferase nejire im Rand der Imaginalscheibe. Diese örtlich begrenzte Aktivität von nejire wird nicht durch eine lokale, intrinsische Aktivität oder Expression des Enzymes, sondern durch die lokale Verfügbarkeit des metabolischen Substrates Acetyl-CoA bestimmt. Das benötigte Acetyl-CoA wird spezifisch in zur Zelloberfläche hin gerichteten Zellkernen durch eine erhöhte Menge nukleärer Acetyl-CoA Synthase generiert, welche Acetat in Acetyl-CoA umwandelt. Metabolisch ist das randspezifische Acetylierungsmuster von der mitochondrialen Fettsäureverbrennung abhängig, die ebenfalls verstärkt im Rand der Flügelimaginalscheibe stattfindet und das notwendige Acetat generiert. Die nicht uniforme Histonacetylierung beeinflusst die epigenetische Expressionskontrolle von Genen, die in zentralen, entwicklungsbiologischen Signalwegen, wie Hippo, Notch und Hedgehog, wirken.

Mechanismus der epigenetischen Regulation hin, der durch die Position des Zellkerns im Gewebe und durch einen adaptierten zellulären Stoffwechsel bestimmt wird und potentiell die Entwicklung der Flügelimaginalscheibe kontrolliert.

1. Introduction

1.1 Cellular metabolism is aligned with cell fate

Proper cell and tissue functions depend on a correctly aligned cellular metabolism. Different cellular states, being quiescent or proliferative, static or migrating, or exposed to varying cellular environments, such as hypoxia or normoxia, rely on distinct metabolic and energetic requirements. Therefore, cells have to constantly balance their anabolic and catabolic needs and adapt means of energy production accordingly. In principle, cells have two main pathways for energy production, namely glycolysis and oxidative phosphorylation (Fig. 1). During glycolysis ATP is generated through the conversion of glucose to pyruvate, which is eventually excreted as lactate in animals. For oxidative phosphorylation, redox-factors, such as nicotinamide adenine dinucleotide (NAD) and flavin adenine dinucleotide (FAD), are reduced in the tricarboxylic acid cycle (TCA) and used to establish a mitochondrial membrane potential via the electron transport chain for ATP production. The TCA cycle, in turn, is fueled by acetyl-CoA derived from pyruvate through pyruvate dehydrogenase (PDH), from fatty acid β-oxidation (FABO), or by α-ketoglutarate derived from glutaminolysis (Fig. 1).

Proliferative cells depend on fast ATP production but also require metabolic building blocks to synthesize macromolecules for rapid growth. Even though oxidative phosphorylation is the most efficient pathway for energy production, it also completely converts glucose to carbon dioxide, reducing the amounts of metabolic intermediates in the cell. Hence, proliferative cells typically use glycolysis for energy production, which, on the one hand, can produce ATP faster than oxidative phosphorylation and, on the other hand, does not deplete TCA cycle intermediates required for macromolecule biosynthesis. This phenomenon was first described in highly proliferative and glycolytic cancer cells and is known as the Warburg effect[1–3]. However, this metabolic switch is not unique to the aberrant growth of tumor cells but also occurs in physiological processes as in tissue growth and development. Among other processes, this phenomenon has been shown in the larvae of the fruit fly *Drosophila melanogaster*. There, larval growth is maintained through the induction of a transcriptional program by the estrogen-related receptor involving genes in glucose uptake and glycolysis to globally promote carbohydrate usage and to increase glycolytic flux[4]. Also, mammalian stem cells residing in hypoxic environments have to rely on a non-aerobic, glycolytic metabolism. However after differentiation, their daughter cells perform oxidative phosphorylation for energy production[5,6]. This concept is exemplified by glycolytic hematopoietic stem cells, which are located in a hypoxic niche in the bone marrow and display a metabolism distinct from their differentiated progeny[7].

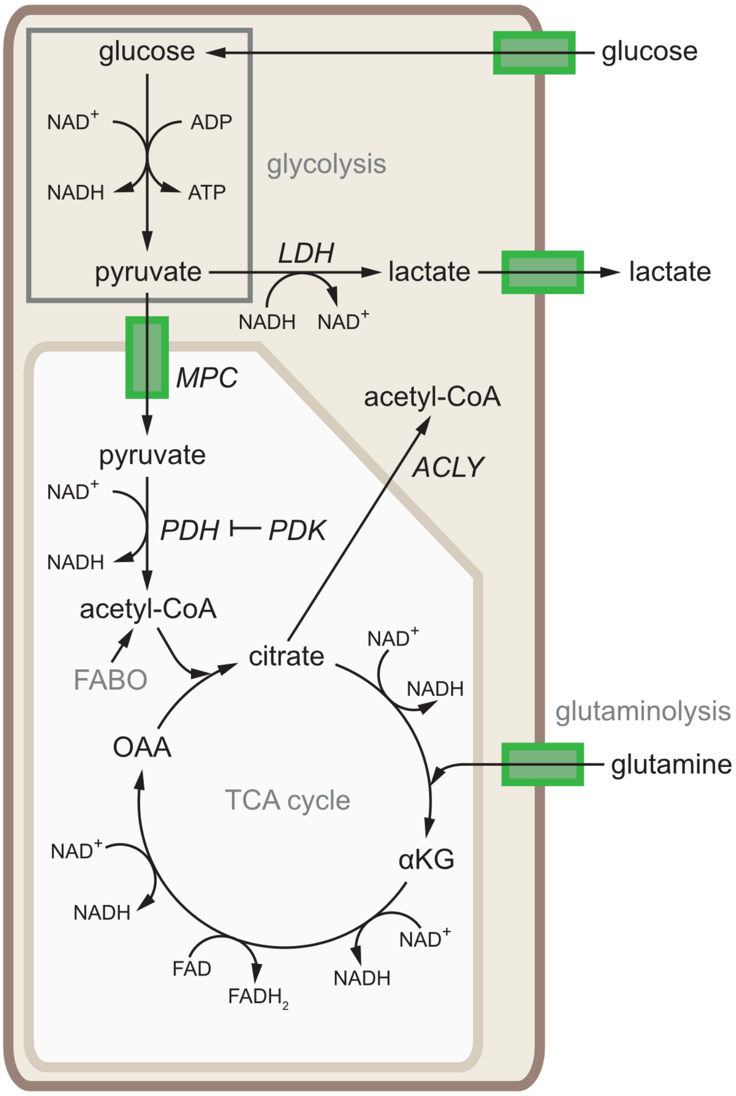

Fig. 1: Central carbon metabolism
For cellular energy production, imported glucose is metabolized into pyruvate and ATP through glycolysis. Pyruvate is then either converted to lactate by the lactate dehydrogenase (LDH) and excreted or used for acetyl-CoA production. For the later, pyruvate is imported into mitochondria via the mitochondrial pyruvate carrier (MPC) and converted into acetyl-CoA by pyruvate dehydrogenase (PDH), which is negatively regulated by pyruvate dehydrogenase kinase (PDK). Pyruvate-derived acetyl-CoA fuels the tricarboxylic acid (TCA) cycle producing redox-factors such as flavin adenine dinucleotide (FAD) or nicotinamide adenine dinucleotide (NAD). Alternatively, the TCA cycle can be driven by acetyl-CoA from fatty acid β-oxidation (FABO) or α-ketoglutarate (αKG) derived from glutaminolysis. Redox-factors generated in the tricarboxylic acid (TCA) cycle are subsequently used for ATP production through oxidative phosphorylation in mitochondria. To provide acetyl-CoA as metabolic substrate for cytoplasmic or nuclear enzymes, the TCA cycle intermediate citrate can be exported from mitochondria and converted to acetyl-CoA by the ATP citrate lyase (ACLY). OAA, oxaloacetate

It has been long believed that adaptations in cellular metabolism, such as the Warburg effect, are mere downstream effects of altered cell function and fate. In this view, proliferative cells undergo a glycolytic shift to respond to changed metabolic requirements imposed by an altered cellular fate[1–3]. However, recent studies have validated a new concept in which the cellular metabolism also has an instructive role on cell fate. For example, Ryall *et al.*[8] show that metabolic alterations during muscle stem cell activation regulate cell differentiation through epigenetic changes. Bulusu *et al.*[9] document a glycolytic activity gradient in the mouse embryo required for presomitic mesoderm cell differentiation, yet the underlying metabolic mechanisms remain unclear.

1.2 Metabolism exerts epigenetic control of cell fate

One mechanism whereby metabolites exert cellular control is through post-translational modifications, which, in turn, regulate protein and consequently cell functions[10]. Accordingly, concentrations of metabolites are mirrored in levels of the corresponding post-translational modifications. As described below, one prominent example on how such metabolically regulated protein modifications impact cell function is the epigenetic control of gene expression through histone modifications. Gene expression in a cell is strongly modulated by the ‘epigenetic code’, consisting of a combination of different histone modifications in specific genomic locations (Fig. 2)[11]. They affect DNA compaction and regulate expression through the recruitment of ‘readers’ to the genome, such as transcriptional co-activators or repressors. Histone acetylation causes more open and active chromatin, called euchromatin, as the acetyl group neutralizes the positive charge of the modified lysine which weakens the interaction between histones and the negatively charged DNA[12,13]. Furthermore, acetylation recruits transcription activators mostly to promoter and enhancer gene regions[11]. In contrast to histone acetylation, methylation mainly regulates gene expression through interaction with ‘readers’. Histone methylation is present throughout the genome and has been known to be associated with both active euchromatin (e.g. H3K9me1 and H3K36me3) as well as compacted, inactive heterochromatin (e.g. H3K9me2 and H3K9me3) depending on the site of the modification[11,13].

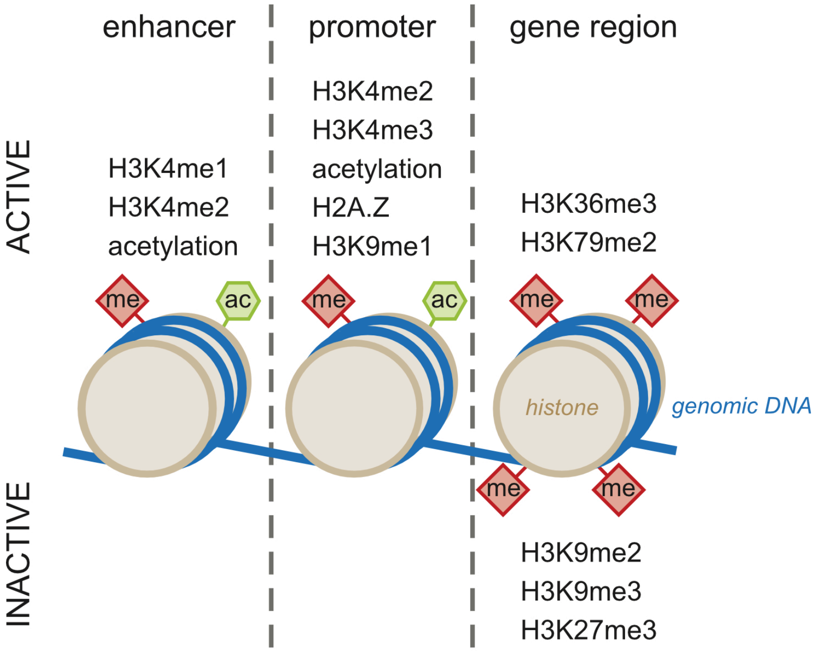

Fig. 2: Genomic distribution of histone modifications
Histone acetylation mainly occurs in enhancer and promoter gene regions and is associated with transcriptionally active chromatin, called euchromatin. In contrast, histone methylation marks can be found throughout the genome, associated with either euchromatin or inactive heterochromatin. Histone acetylation (ac) and methylation (me) marks are depicted as green and red symbols, respectively.

Histone modifications are a read-out of the metabolic state of a cell as most histone modifying and de-modifying enzymes require metabolic co-factors or substrates for their function (Fig. 3)[14,15]. Histone acetyltransferases (HAT) require acetyl-CoA while histone methyltransferases (HMT) use S-adenosyl methionine (SAM) for histone modification[14–17]. The class of metabolite-dependent histone deacetylases (HDAC), called sirtuins, needs NAD^+ for proper enzyme function[16,18,19]. FAD or α-ketoglutarate are required metabolic co-factors for histone demethylases (HDM) carrying a lysine-specific demethylase 1 domain or a Jumonji C domain, respectively (Fig. 3)[15–17]. Hence, changes in the cellular metabolism, that alter levels of these metabolites, consequently also affect the epigenetic landscape of a cell. For example, high glycolytic flux increases the acetyl-CoA concentration but decreases NAD^+ levels promoting acetylation while inhibiting deacetylation. Accordingly, increased glycolytic flux may lead to an increase in histone acetylation. Such metabolic regulation of the epigenetic state of the cell has been well documented in recent studies. Wellen *et al.*[20] link changes in the histone acetylation status of a cell to fluctuations in its glycolytic flux. In this study, histone acetylation levels depended on glucose-derived citrate, which was converted to acetyl-CoA by the ATP citrate lyase to promote HAT activity (Fig. 1). Studies by McDonnel *et al.*[21] and Ryall *et al.*[8] even go a step further by investigating the downstream effect of metabolically regulated histone modifications on cell function and fate. In detail, McDonnel *et al.*[21] document that fatty acid β-oxidation derived acetyl-CoA causes histone acetylation and reprograms the cellular metabolism through lipid-specific gene expression. Ryall *et al.*[8] show that the metabolic shift seen during muscle stem cell activation causes a drop in NAD^+ levels, which decreases deacetylase activity of sirtuin 1 (Sirt1). The resulting hyperacetylation induces muscle gene transcription and cellular differentiation.

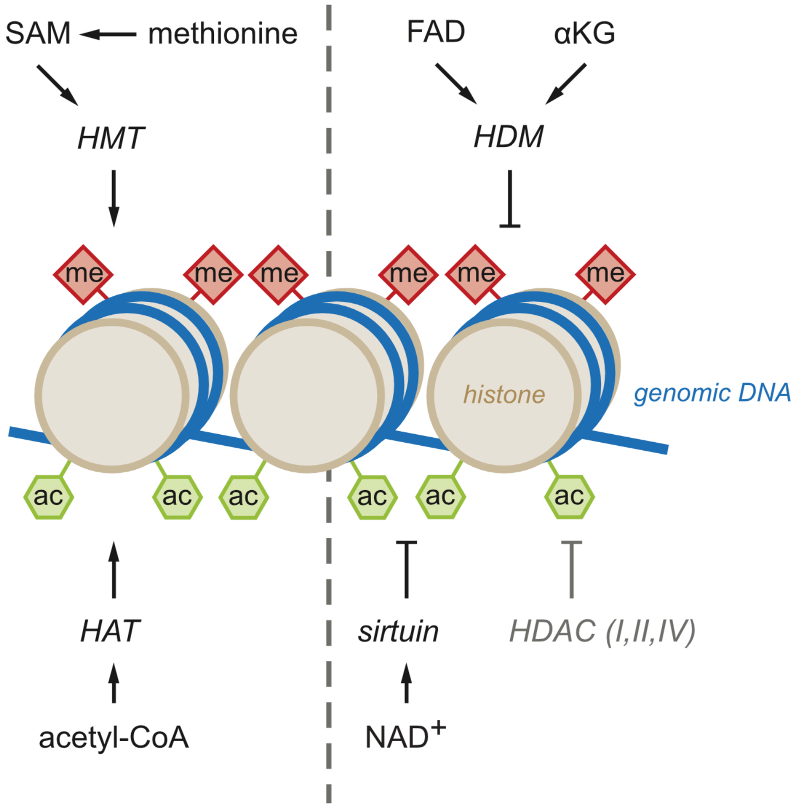

Fig. 3: Metabolic regulation of histone modifying and de-modifying enzymes
Histone modification by histone methyltransferases (HMT) or histone acetyltransferases (HAT) require methionine derived s-adenosylmethionine (SAM) or acetyl-CoA, respectively. Histone demethylases (HDM) need flavin adenine dinucleotide (FAD) or α-ketoglutarate (αKG) for enzyme function. Histone deacetylase (HDAC) classes I, II, and IV are metabolite-independent whereas class III HDACs (sirtuins) utilize NAD^+ for enzyme activity. Histone acetylation (ac) and methylation (me) marks are depicted as green and red symbols, respectively.

The importance of an instructive role of the metabolism on the epigenome, but also on protein function in general, is supported by the identification of novel types of post-translational modification dependent on metabolites[10]. The expanding list of newly documented modifications include various histone acylations as well as lactylation[12,22,23]. For example, Zhang *et al.*[22] show that cellular stress in bacterially challenged macrophages causes an increase in cellular lactate and, consequently, in histone lactylation levels, which modulates gene expression to support macrophage functions.

1.3 Nuclear positioning and cell fate

So far, most studies analyzing the metabolic regulation of the epigenome use cell lines as a simplified model system. However, principles of metabolic control of the epigenetic regulation of cell fate are likely more complex *in vivo*. Such principles are clearly less well understood and their elucidation requires the use of developing and adult tissue models. One aspect of tissue growth and development not recapitulated in cell models is the relevance of nuclear localization within a cell but also relative to tissue architecture. Nuclear localization can be dynamic and changes depending on cell type and state. In many somatic cells the nucleus is positioned in the center of the cell. However, some specialized cell types, including stem cells, neurons, or migratory cells display an asymmetric nuclear localization[24]. Also, the position of the nucleus in polarized epithelia or in proliferating cells changes depending on the cell cycle phase[24–26]. Correct alignment of nuclear localization with cell function is essential for proper tissue development. One prominent example is the nuclear movement during the cell cycle, called interkinetic nuclear migration, in a pseudostratified epithelium (Fig. 4)[24,25,27]. A pseudostratified epithelium, like the wing imaginal disc of *Drosophila melanogaster*, is a monolayered tissue in which each cell reaches from the basal to the apical tissue side. Such densely packed cells give the impression of a multilayered tissue. Here, interkinetic nuclear migration describes the phenomenon that the nucleus of each cell travels between the basal and the apical tissue side during the cell cycle, moving basally during G1 phase and having a basal position during S-phase before relocating apically again during G2 phase. The cell undergoes mitosis when the nucleus is apically as this position allows for the required space for the morphological changes (rounding up) of the cell during this process (Fig. 4). Correct nuclear positioning is important in tightly packed epithelia to ensure organized and correctly oriented cell division essential for proper tissue development[24–26]. The importance of nuclear positioning in cell division has also been shown for other processes, such as the formation of the neural tube in vertebrates or the ommatidium in flies, where the nuclear localization within the cell defines the plane of cell division and, consequently, cell fate and tissue organization[24,28,29]. The pathways regulating interkinetic nuclear migration are still enigmatic but seem to be driven by different molecular mechanisms dependent on cell and tissue contexts. Nuclear movement is mainly powered by actin filaments or microtubules and their associated motor proteins that interact with proteins in the nuclear envelope, called 'linkers of nucleoskeleton and cytoskeleton'[24]. Evidence suggests that the apical nuclear movement in the

Drosophila wing imaginal disc is active and dependent on actomyosin interaction[25]. In contrast, basal nuclear movement has been proposed to happen through passive, non-autonomous displacement[30].

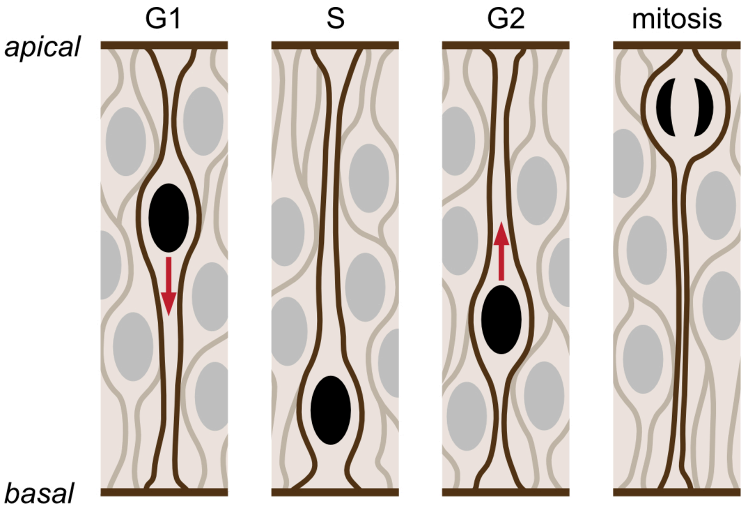

Fig. 4: Interkinetic nuclear migration Nuclei in pseudostratified epithelia move from the apical to the basal tissue side in the G1 and S-phase and back to the apical surface during the G2-phase. There, apical cells round up and go through mitosis. Direction of nuclear movement is indicated by red arrows.

As for metabolites, nuclear positioning has so far been mainly studied as a downstream effect of cell fate and functions, as during cell division. However, an emerging concept proposes a more instructive role of nuclear localization in biological processes, including in signaling, growth, and cell differentiation[24]. For instance, Del Bene *et al.*[31] use the neuroepithelium of the zebrafish, which displays an apico-basal Notch gradient, to study the instructive role of nuclear positioning. Aberrant nuclear movement due to a mutation in the motor protein Dynactin-1 in the neuroepithelium decreases nuclear exposure to Notch and leads to premature cell cycle exit. This causes an imbalance in neuroepithelial differentiation and proliferation.

Given the proposed roles for both metabolic control of the epigenome and nuclear positioning in instructing cell fate, interconnection of these two biological processes in the regulation of tissue development is an attractive hypothesis. I tested such an interconnection in my PhD project.

1.4 The wing imaginal disc as a model system to study cell fate

As mentioned above, most studies on metabolic and epigenetic regulation of cell fate focus on cells in culture. In my PhD project, I rather intended to study these processes in a living organism to more accurately recapitulate processes of tissue development *in vivo*. Accordingly, I chose the fruit fly *Drosophila melanogaster* as an experimental model system. *Drosophila* is widely used as a model system to study regulatory processes in development and adult tissue homeostasis. Especially, the wing imaginal disc is studied to investigate different aspects of tissue growth, such as tissue patterning and control of organ size. The wing imaginal disc (subsequently referred to as the wing disc) is one of several epithelial precursor tissues in the larva, called imaginal discs, that will later give rise to different adult structures, including wings, legs, eyes, and antennas. During larval development, the wing disc grows massively from a few dozen progenitor cells to a sac-like structure comprising 50,000-75,000 cells[32–34]. In the third and last larval stage, the wing disc consists of two continuous, mono-layered epithelia, the disc proper and the peripodial membrane (Fig. 5a-b). The disc proper is a pseudostratified epithelium with elongated columnar cells, whereas cells in the peripodium are squamous[35–37]. The disc proper is structurally divided along three main axis, namely anterior-posterior, dorsal-ventral, and distal-proximal (Fig. 5a). It comprises different tissue compartments defined according to the adult structures that they will give rise to. These entail the distal pouch (Fig. 5a-c , light green), giving rise to the adult wing and the proximal compartments of the hinge (blue), the notum (red) and the pleura (grey), forming the wing hinge as well as part of the thorax[32,33,35,38,39]. During metamorphosis, the pouch elongates along its dorsal-ventral boundary to develop into the adult wing through a process called eversion (Fig. 5d).

Extrinsic and intrinsic factors that control cell differentiation and tissue growth have been extensively studied in the wing disc. As in all growing tissues, wing disc development is regulated by intrinsic factors, such as morphogens and mechanical forces. Morphogens are secreted signaling molecules that are locally produced and spread from their patterning centers forming a tissue gradient to determine cell fate and differentiation in a dose-dependent manner. The wing disc is mainly patterned by three morphogens, Decapentapleigic (Dpp) and Hedgehog (Hh) along the anterior posterior boundary and Wingless (Wg) along the dorsal-ventral axis[34,40,41]. Especially the role of Dpp in wing disc growth has been studied extensively

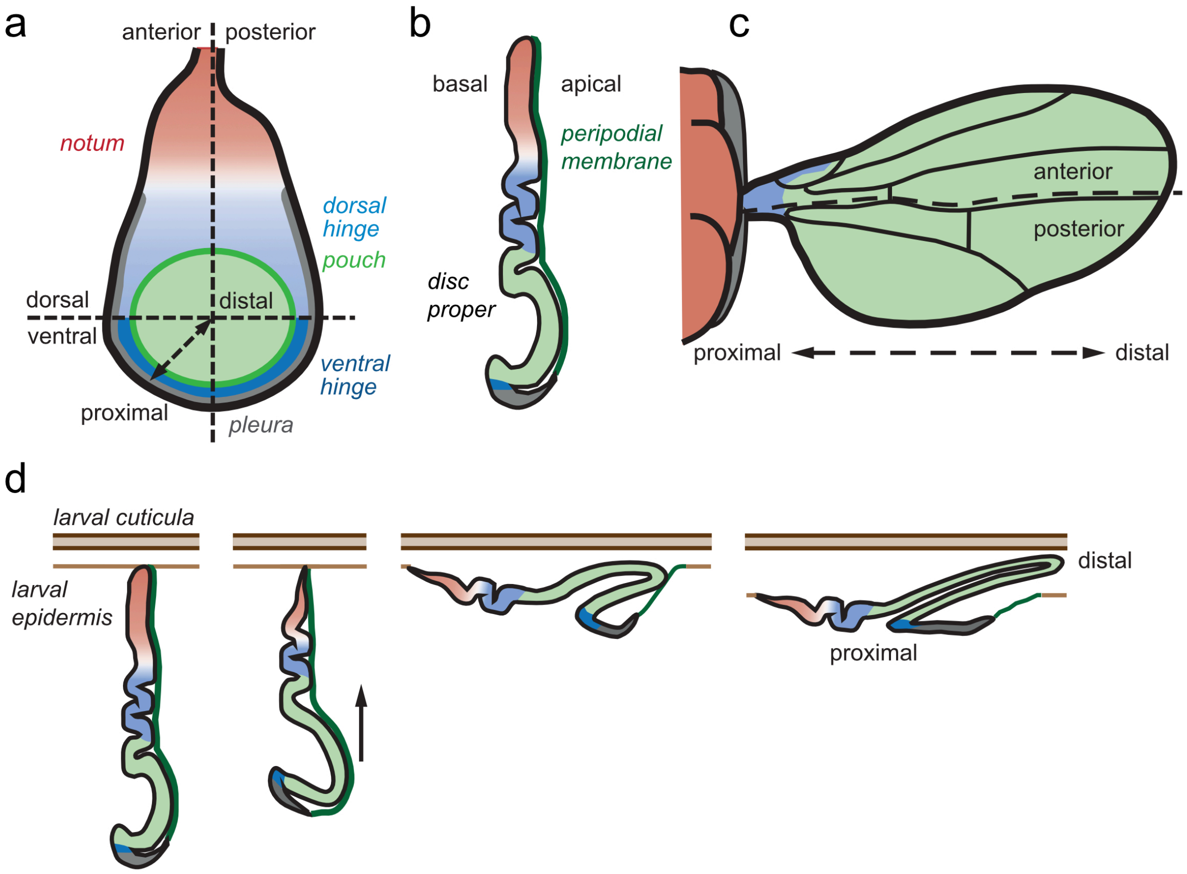

Fig. 5: Wing imaginal disc and wing of *Drosophila melanogaster*
The morphology and the different compartments of the wing imaginal disc are displayed in x-y section (**a**) or cross-section (**b**). The wing disc consists of the peripodial membrane (dark green) and the disc proper. The disc proper is further divided into the pouch (light green), the hinge (blue), the notum (red), and the pleura (grey), giving rise to the adult wing, hinge, and part of the thorax, respectively. The structure of the adult fly wing is illustrated in (**c**). The process of wing disc eversion is depicted in (**d**), during which the wing pouch (light green) elongates along the dorsal-ventral boundary to form the adult wing.

with impaired Dpp signaling reducing tissue size while increased Dpp signals leading to overgrowth[42,43]. Another important signaling pathway to regulate growth is Hippo signaling[38]. It integrates mechanical cues within the growing tissue, including information on cell adhesion, polarity, and the actin cytoskeleton, to regulate cell proliferation accordingly[44–46]. In addition to intrinsic factors, wing disc morphogenesis also requires external stimuli that prominently include nutrients. Thus, the nutritional status of the tissue is sensed by the insulin/insulin-like growth factor signaling (IIS) pathway. High nutrient availability promotes expression of insulin-like peptides which activate growth promoting pathways, such as target of rapamycint[33,47]. Interference with the IIS, similar to starvation, impairs tissue growth while enhanced signaling leads to an increased tissue size[48–53]. Even though many regulators of wing disc development have been identified, not all aspects of tissue growth are completely understood yet. Open questions include how tissues sense their size and how reproducible, ultimate organ size is achieved. But also, the intrinsic, regulatory role of the cellular metabolism and of the nuclear positioning in tissue development are not fully comprehended.

One of the many reasons why the wing disc of the fruit fly is an ideal model system to study intrinsic and extrinsic factors in tissue development is the high number of available genetic tools to introduce region- and time-specific genetic perturbations[54]. The genetic tool, which I frequently used in my PhD project, is the UAS/GAL4-system (Fig. 6). It consists of the transcriptional activator GAL4 and its recognition sequence, the upstream activating sequence (UAS), which controls expression of a downstream transgene (Fig. 6a). Depending on the selected GAL4 promoter, GAL4 and, consequently, transgene expression can be directed to defined tissues or even tissue compartments as well as to developmental stages, allowing e.g. for RNAi-induced knock down or overexpression of any target protein of choice[54,55]. For example, GAL4 under the control of the hh promoter is expressed exclusively in the posterior tissue compartment throughout development (Fig. 6c). Spatial transgene expression can be further refined by combining the UAS/GAL4-system with the transcriptional repressor GAL80, which binds and inhibits GAL4 (Fig. 6b)[55–57]. Overlapping expression of GAL80 and GAL4, hence, prevents UAS-dependent transgene induction to further specify expression domains (Fig. 6d). Finally, temporal transgene expression can be additionally regulated using a temperature-sensitive GAL80 ($G80^{ts}$)[58]. This mutant GAL80 becomes instable with increasing temperature and, consequently, allows repression or induction of transgene expression through a temperature shift (Fig. 6e).

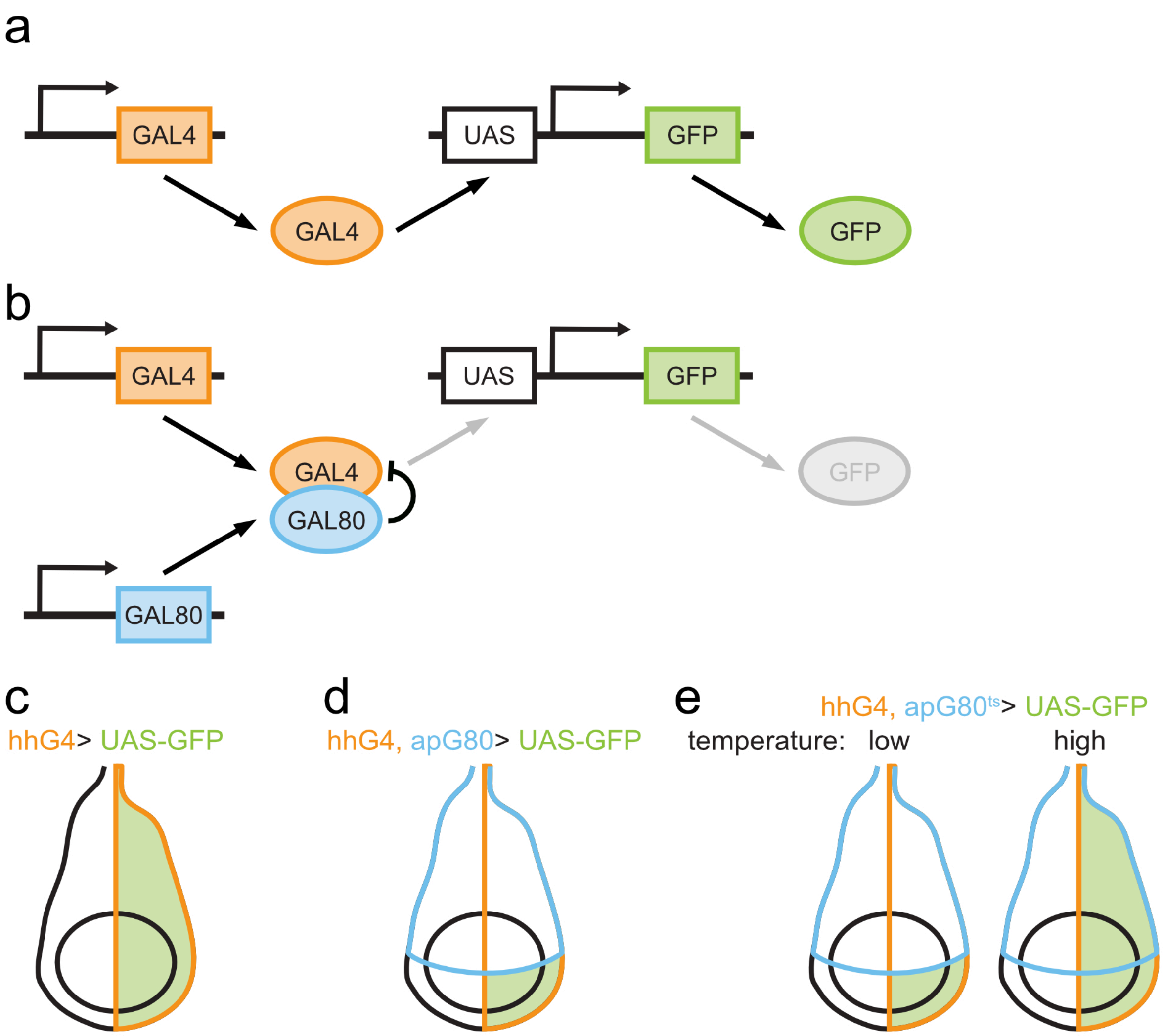

Fig. 6: UAS/GAL4/GAL80-system
(**a**) The transcriptional activator GAL4 binds to the upstream activating sequence (UAS) to induce target transgene expression, exemplified here by green fluorescent protein (GFP). (**b**) GAL4-dependent transcription is blocked by GAL80, which binds and inhibits GAL4. (**c-e**) Genetic tools for temporal and spatial control of GAL4 activity in the wing disc are depicted. GAL4 expression (orange) under the hedgehog (hh) promoter (hhG4) induces GAL4 and, consequently, GFP expression (green) in the posterior wing disc compartment (c). Co-expression GAL4 in the posterior compartment with GAL80 (blue) under control of the apterous (ap) promoter (apG80) in the dorsal compartment restricts GAL4-dependent GFP expression to the ventral posterior compartment (green; d). Expression of a temperature-sensitive GAL80 variant ($G80^{ts}$) blocks GAL4-dependent GFP expression (green) at low but not high temperatures (e).

1.5 Aim of the study

Control of tissue growth and development is essential for proper organ function but also for the integrity of the entire organism and misregulated tissue growth has been associated with severe medical conditions, such as cancer. Therefore, understanding the molecular mechanisms orchestrating tissue growth and development is an important topic in biomedical research. Exciting new concepts suggest instructive roles for the metabolism in the epigenetic regulation of cell fate. However, such processes have mainly been addressed in cultured cells *in vitro* and are, as yet, not well described in the context of a developing complex tissue *in vivo*. Especially, it is poorly understood if and how the cellular metabolism adapts to changes during tissue morphogenesis as well as to tissue architecture and how this impacts the epigenome accordingly to exert control of cell fate and development. Hence, the overall aim of this PhD project was to investigate the relevance of cellular metabolism and nuclear positioning as novel regulators of cell fate during tissue development using the wing imaginal disc of *Drosophila melanogaster* as an experimental model of a pseudostratified epithelium.

2. Material and Methods

2.1 Explant cultures

Ex vivo explant cultures were used for drug treatments as well as live stainings of wing discs. In detail, third-instar larvae were dissected in explant medium (Schneider's Drosophila medium (Gibco 21720024) containing 100 U/ml penicillin, 100 µg/ml streptomycin (Gibco 15140122), 1.6 nM juvenile hormone (Sigma -Aldrich 333725), 5 nM ecdysone (Enzo Life Sciences LKT-E0813-M010), 8.3 ng/ml adenosine deaminase (Roche 10102105001), and 10 µg/ml insulin (Sigma-Aldrich I0516)), which was previously shown to maintain wing discs stress-free and proliferative for up to 6 hours[59]. Incubations were performed in explant chambers (mash basket in small glass vial) containing explant medium under constant stirring for oxygenation. Concentration and duration of drug treatments are indicated in the corresponding figure legends (see Tab. 1 for compounds used).

Tab. 1: List of used compounds
ACSS2, acetyl-CoA synthase

compound	company	product number	solvent
ACSS2 inhibitor (ACSS2i)	Biozol	SEL-S8588	DMSO
A485	Cayman	Cay24119-1	DMSO
BMS303141	Sigma-Aldrich	SML0784	DMSO
carbonyl cyanide-p-trifluoromethoxyphenylhydrazone (FCCP)	Biomol	Cay15218-10	ethanol
etomoxir	Sigma-Aldrich	E1905	H2O
glutaminase inhibitor 968 (968)	Sigma-Aldrich	SML1327	DMSO
nicotinamide (NAM)	Sigma-Aldrich	72340	H2O
panobinostat (PB)	Cayman	Cay13280-5	DMSO
sodium acetate	Roth	6773.2	H2O
sodium butyrate	AlfaAesar	A11079	H2O
sodium citrate	MP	199635	H2O
sodium octanoate	Sigma-Aldrich	C5038	H2O
splitomicin (split)	Biotrend	10-2615-5	DMSO
trichostatin A (TSA)	Sigma-Aldrich	T1952	DMSO
2-deoxy-glucose (2DG)	Sigma-Aldrich	D8375	H2O
6-diazo-5-oxo-L-norleucin (DON)	Sigma-Aldrich	D2141	H2O

2.2 Live staining of mitochondrial membrane potential and lipid droplets in the wing disc

For live imaging of the mitochondrial membrane potential using tetramethylrhodamine-methylester (TMRM), wing discs from third-instar larvae ubiquitously expressing a mitochondrially-targeted GFP (mitoGFP) driven by tubulinG4 (tubG4) were dissected in explant medium and transferred into an explant chamber containing explant medium supplemented with TMRM (50 nM, Biomol ABD-22221) and the indicated compounds. Concentration and duration of treatments are indicated in the corresponding figure legends (see Tab.1 for compounds used). After incubation in the dark, wing discs were mounted on slides in explant medium and imaged using a Leica SP8 confocal microscope.

The genetically encoded, mitochondrial pH Sensor Sypher3s-dmito[60] allows visualization of the mitochondrial pH and, hence, serves as an indicator of the mitochondrial membrane potential, which is established through a proton gradient. SypHer3s-dmito is based on the hydrogen peroxide sensor Hyper, consisting of a circularly permutated yellow fluorescent protein inserted into the regulatory domain of the bacterial hydrogen peroxide sensor OxyR, which features a mutation rendering the sensor insensitive to hydrogen peroxide but retaining sensitivity towards pH[61]. The sensor has two excitation maxima around 405 nm with a pH-insensitive emission and around 488 nm with an emission showing increased intensity with higher pH.

To analyze the mitochondrial membrane potential in the wing disc using SypHer3s-dmito, a transgenic fly line expressing this sensor was generated first. To do so, the sensor-coding sequence was transferred from a mammalian expression vector (Addgene 108119[60]) into a pUAST-attB vector[62], allowing site-directed insertion of the transgene into the fly genome and expression under control of the UAS/GAL4-system (see Tab. 2 for primers used). The transgene was inserted into the VK33 docking site by phiC31-mediated recombination.

For live imaging of mitochondrial membrane potential using SypHer3s-dmito, wing discs from third-instar larvae expressing the sensor under control of tubG4 were dissected in explant medium and transferred into an explant chamber containing explant medium and the indicated inhibitors. Concentration and duration of drug treatments are indicated in the corresponding figure legends (see Tab. 1 for compounds used). After incubation in the dark, wing discs were mounted on slides in phosphate-buffered saline (PBS) and imaged using a Leica SP8 confocal microscope. Images are shown in ratiometric configuration as a ratio of emission with 488 nm excitation (pH-sensitive) and 405 nm excitation (pH-insensitive). Darker colors (blue-violet) indicate lower pH and lower mitochondrial membrane potential while brighter colors (yellow-white) represent higher pH and higher membrane potential.

Tab. 2: List of used primers
drm, drumstick; FISH, fluorescence *in situ* hybridization; Gapdh2, glyceraldehyde 3 phosphate dehydrogenase 2; grn, grain; hth, homothorax; mamo, maternal gene required for meiosis; mirr, mirror; nej, nejire; nt, nucleotide, Sox15, Sox box protein 15; zfh2, Zn finger homeodomain 2

purpose	target	orientation	sequence	notes
cloning	SypHer3s-dmito	forward	aaccgtcagatccagatctatgtccgtcct	BgIII restriction site
cloning	SypHer3s-dmito	reverse	gatatctcgagttaaaccgcctgttttaaaac	XhoI restriction site
FISH	E5	forward	cgacgagtccttttgtgagc	length: 424 nt
FISH	E5	reverse	ccggtaatacgactcactatagggcggatgagggttggaggatt	
FISH	drm	forward	ctcttcaccgaccaatcagc	length: 305 nt
FISH	drm	reverse	ccggtaatacgactcactataggggcaaacattttgacaggcgg	
FISH	Gapdh2	forward	accaagaacactacccaccc	length: 200 nt
FISH	Gapdh2	reverse	ccggtaatacgactcactatagggtgtggctggtaattgaagagc	
FISH	grn	forward	acaacatggacacctctcga	length: 400 nt
FISH	grn	reverse	ccggtaatacgactcactatagggttcggtgccactgtcaattg	
FISH	hth	forward	catgcacggctaccattcg	length: 307 nt
FISH	hth	reverse	ccggtaatacgactcactataggggacttcgggatctgcggtat	
FISH	mamo	forward	tactacaagacgggagcctg	length: 305 nt
FISH	mamo	reverse	ccggtaatacgactcactatagggcagcgtcgtattctggttcg	
FISH	mirr	forward	ataaccacccagagctaccg	length: 350 nt
FISH	mirr	reverse	ccggtaatacgactcactatagggctgtcctccactcgatccac	
FISH	nej (probe 1)	forward	ccaaatctgcgtactctggc	length: 307 nt
FISH	nej (probe 1)	reverse	ccggtaatacgactcactatagggtttggctcggtatgggaact	
FISH	nej (probe 2)	forward	gcggtgctgtggacataaaa	length: 368 nt
FISH	nej (probe 2)	reverse	ccggtaatacgactcactatagggatagacccgcgatgttttgc	
FISH	Sox15	forward	tgggatgcaatacgaggact	length: 351 nt
FISH	Sox15	reverse	ccggtaatacgactcactatagggccctcgtatccgccatagtt	
FISH	zfh2	forward	tacaatcttgatggcagcgc	length: 431 nt
FISH	zfh2	reverse	ccggtaatacgactcactatagggagtcggtgttcagtgtttgc	

Lipid droplets in the wing disc were visualized using BODIPY staining. For this purpose, wing discs from third-instar larvae were dissected in explant medium and transferred into explant chambers containing explant medium supplemented with BODIPY (10 µM, Sigma-Aldrich 790389) and Hoechst 33342 (10 µg/ml, Sigma-Aldrich B2261). After incubating for 10 or 30 min in the dark, carcasses were rinsed once with PBS before fixation for 20 min in 4% formaldehyde (FA). Before mounting the wing discs in mounting medium (80% glycerol, 1x

PBS, 20 mM n-propyl gallate (Sigma-Aldrich P3130)), the carcasses were rinsed twice and then washed two times for 10 min each with PBS. Fluorescence signals in the tissue were detected by confocal microscopy (Leica SP8 confocal microscope).

To align wing disc orientations in the figure panels, some disc images were rotated. The resulting empty corners of the squares were underlaid with solid black boxes for a more consistent panel layout.

2.3 Immunofluorescence staining of wing discs

Unless indicated otherwise, immunostainings were performed on wing discs from third-instar larvae. In detail, larvae were either dissected in PBS or incubated in explant cultures and, thereafter, fixed for 20 min in 4% FA. All subsequent washing and incubation steps were performed while gently rocking the carcasses on a shaking platform. The carcasses were rinsed twice followed by two washes for 10 min in PBS containing 0.3% Triton (PBTr). Carcasses were blocked for 45 min in PBTr containing 5% BSA (BBT) before incubation with primary antibodies alone or together with Alexa Fluor™ 488 Phalloidin (Invitrogen A12379) or Alexa Fluor™ 633 Phalloidin (Invitrogen A22284) in BBT overnight at 4°C (see Tab. 3 for antibodies used). To remove the primary antibodies, carcasses were rinsed twice, followed by two washing steps for 60 and 30 min in BBT. The carcasses were then incubated in BBT containing DAPI (2.5 µg/ml, AppliChem A1001) and secondary antibodies (1:250) at room temperature in the dark (see Tab. 3 for antibodies used). Before mounting the wing discs in mounting medium, the carcasses were rinsed twice and then washed two times for 30 min each with BBT. Immunofluorescence signals in the tissue were detected by confocal microscopy (Leica SP8 confocal microscope). Sum intensity projections were generated using FIJI.

To align wing disc orientations in the figure panels, some disc images were rotated. The resulting empty corners of the squares were underlaid with solid black boxes for a more consistent panel layout.

Tab. 3: List of used primary and secondary antibodies
The lpp #1 antibody was used in Figures 17 and 19. The lpp #2 antibody was used in Figure 18. AcCoAS, acetyl-CoA synthase; ac-K, total acetylated lysine; ATPCL, ATP citrate lyase; Cy5, cyanine 5; FITC, fluorescein isothiocyanate; H3, histone 3H3K18crot, H3K18 crotonylation; lpp, lipoprotein; PDH, pyruvate dehydrogenase; pH3 S10, phospho-H3 serine 10; pPDH S293, phospho-PDH serine 293; TRITC, tetramethylrhodamine; tubK40ac, α-tubulin lysine 40 acetylation

antibody	**species**	**source**	**product number**	**LOT**	**dilution**
primary antibodies					
AcCoAS	rabbit	Abcam	Ab264391	GR3350114-1	1:200
ac-K	rabbit	Cell Signaling	9814S	5	1:200
ATPCL	rabbit	Novus Biologicals	NBP1-90266	R09359	1:200
H3	rabbit	Cell Signaling	2650S	3, 4	1:200
H3K9ac	rabbit	Active Motif	39137	9811002	1:500
H3K9me1	rabbit	Abcam	Ab9045	GR323589-1	1:500
H3K9me2	mouse	Abcam	Ab1220	GR183500-3	1:500
H3K9me3	rabbit	Abcam	Ab8898	GR3176468-1	1:500
H3K18ac	rabbit	Abcam	Ab1191	GR300534-1, GR3287957-1	1:500
H3K18crot	rabbit	Cusabio	CSB-PA010418OA18crHU	G0822A	1:100
H3K27ac	rabbit	Abcam	Ab4729	GR323154	1:500
H3K36me3	rabbit	Abcam	Ab9050	GR166781-1	1:500
H4K8ac	rabbit	Abcam	Ab15823	GR3209076-1, GR3294416-1	1:500
lpp #1	guinea pig	Eaton Lab[63]			1:100
lpp #2	rabbit	Eaton Lab[63]			1:100
pH3 S10	mouse	Cell Signaling	9706S	17	1:200
pPDH S293	rabbit	Abcam	Ab92696	GR319281-1	1:200
tubK40ac	rabbit	Cell Signaling	5335	6	1:200
secondary antibodies					
anti-rabbit TRITC	donkey	Jackson ImmunoResearch	711-025-152		1:250
anti-mouse TRITC	donkey	Jackson ImmunoResearch	715-025-150		1:250
anti-mouse FITC	donkey	Jackson ImmunoResearch	715-095-151		1:250
anti-guinea pig FITC	goat	Jackson ImmunoResearch	106-095-003		1:250
anti-guinea pig Cy5	donkey	Jackson ImmunoResearch	706-175-148		1:250

2.4 Image quantification and data analysis

All quantifications were performed using FIJI. For quantification of histone acetylation and total acetylated lysine (ac-K) immunosignals, measured integrated intensities were normalized against the corresponding DAPI signal and displayed as the ratio of signal of the rim versus center of the wing disc. The rim was defined as a region of 10 pixels in thickness starting from the edge of the disc and moving inwards. For quantification of the TMRM signal, measured integrated intensities were normalized against the corresponding mitoGFP signal and displayed as the ratio of signal of the rim versus center of the wing disc. The rim was defined as a region of 13 pixels in thickness starting from the edge of the disc and moving inwards. For quantification of α-tubulin lysine 40 acetylation (tubK40ac) immunosignal, sum projections were generated for tubK40ac and DAPI images in FIJI and used to measure integrated intensities. Intensities of tubK40ac were normalized against the corresponding DAPI signals. To combine data from biological replicates of the above-mentioned quantifications, intensities of each replicate were normalized against the average control intensity.

For quantification of nuclear acetyl-CoA synthase (AcCoAS) immunosignal, the DAPI signal was used to outline the nucleus, and mean nuclear intensities were measured in this region using FIJI. Additionally, the distance between the most basal part of each nucleus and the outward-facing tissue surface was determined. The values were then sorted into three bins: <5 μm, 5-10 μm, and >10 μm and normalized to the average of the '< 5 μm' bin.

Statistical significance was determined either by Kruskal-Wallis test with Dunn's multiple comparisons test or by Mann-Whitney test as indicated in the respective figure legends. All significant differences are indicated (*<0.05, **<0.01, ***<0.001, ****<0.0001).

2.5 Fluorescent *in situ* hybridization

The fluorescent *in situ* hybridization (FISH) probes were designed to encompass between 200 and 450 nucleotides of the desired gene transcripts (see Tab. 2 for primers used). Addition of a T7 promoter sequence (ccggtaatacgactcactataggg) to the 5' end of the reverse primer allowed for transcription directly from PCR-amplified fragments using the digoxigin RNA labling kit (Roche 11277073910) according to the manufacturer's protocol. RNA probes were purified (RNA Clean-up, Macherey-Nagel 740948) and stored at -20°C in 50% formamide until use.

For FISH, wandering third-instar larvae were dissected in PBS and fixed for 30 min in 4% FA. Following a rinse in PBS containing 0.1% Tween-20 (PBTw), carcasses were washed twice for 10 min and 20 min in PBTw. Carcasses were incubated for 5 min in PBTw containing 50% methanol before transferring them to methanol, in which they could be stored for several days at -20°C. After 5 min incubation in PBTw containing 50% methanol, carcasses were fixed again for 20 min in 4% FA containing 0.1% Tween-20. FA was removed by three washes in PBTw for 5 min each. The wash buffer was changed to hybridization buffer (HS; 50% formamide, 5x SSC (0.75 M sodium chloride and 75 mM sodium citrate dehydrate), 50 µg/ml heparin, and 0.1% Tween-20) by serial wash steps of 5 min each in HS/PBTw dilutions of 30/70, 50/50, 70/30, and 100/0 (vol/vol). A 10 min wash in HS was followed by 2 h of blocking at 65°C in HS supplemented with 100 µg/ml salmon sperm DNA (Invitrogen 15632-011). In parallel, 15 ng of FISH probe was denatured in 100 µl blocking buffer for 3 min at 80°C. After 5 min on ice, the probe was added to the carcasses and incubated overnight at 65°C. To remove unbound probe, carcasses were rinsed once and washed twice for 5 min and 15 min in HS. The buffer was changed back to PBTw through serial wash steps of 5 min each in HS/PBTw dilutions of 70/30, 50/50, and 30/70 (vol/vol). Subsequently, carcasses were rinsed and washed three times for 15 min each in PBTw before blocking for 60 min in maleic acid buffer (1 M maleic acid, 1.5 M NaCl; pH 7.5) supplemented with 0.5% (w/vol) blocking reagent for nucleic acid hybridization and detection (Roche 11096176001). Carcasses were incubated overnight at 4°C with pre-absorbed (2-3 h incubation with carcasses in the absence of FISH probe) anti-digoxigenin Fab fragments conjugated to horseradish peroxidase (Roche 11207733910). Unbound Fab fragments were removed by three rinses and a 10 min wash in PBTw. Nuclei were counterstained for 15 min in PBTw containing DAPI (2.5 µg/ml), followed by a wash for 10 min in PBTw. To visualize localization of the FISH probes, the TSA Plus Fluorescein Kit

(Akoya Biosciences NEL741001KT) was used according to the manufacturer's protocol. Lastly, carcasses were rinsed once and washed twice for 15 min each with PBT before mounting the wing discs in mounting medium. Fluorescent signals in the tissue were detected by confocal microscopy (Leica SP8 confocal microscope). Sum intensity projections were generated using FIJI.

To align wing disc orientations in the figure panels, some disc images were rotated. The resulting empty corners of the squares were underlaid with solid black boxes for a more consistent panel layout.

2.6 Cleavage under targets and release using nuclease (Cut&Run)

To identify fatty acid β-oxidation-dependent H3K18ac peaks in the Drosophila genome, cleavage under targets and release using nuclease (Cut&Run)[64] was performed on wing discs of wandering third-instar larvae. Cut&Run is a method to analyze DNA-protein interaction, similar to chromatin immunoprecipitation sequencing. It is based on a fusion protein consisting of protein A, able to bind the primary antibody, and a micrococcal nuclease (MNase), which cuts genomic DNA around the binding site. The resulting DNA fragments are then isolated and sequenced.

In this study, the *Drosophila*-optimized Cut&Run protocol by Ahmad and Spens was applied[65] (https://protocols.io/private/D6B0AD2DC1431A513994A2A05AC59CDA). In brief, wandering third-instar larvae were either incubated for 2 h in the presence or absence of 500 µM etomoxir in explant cultures or directly dissected. Wing discs were then bound to Concanavalin A-coated magnetic beads (Polysciences 86057-3) to prevent loss of the discs during subsequent wash steps on a magnetic rack. To allow antibody binding (H3K18ac 1:500; Tab. 3), wing discs were permeabilized with digitonin. After overnight incubation, bound antibodies were decorated with the protein A-MNase fusion protein (Cell Signaling 40366). DNA digestion was induced by addition of calcium to activate MNAse. Samples were supplemented with yeast spike-in DNA. Released DNA fragments were purified using AmpureXP beads (Agencourt A63880).

Libraries were prepared using the KAPA Hyper Prep Kit (Roche 7962312001) following the manufacturer's protocol. In deviation from the protocol, KAPA Pure Beads were replaced by AmpureXP beads. Due to low sample input in Cut&Run, adapter ligation (TruSeq single indexed DNA adapter (Illumina 20015960)) was performed for 3 h. The PCR protocol was altered according to Skene *et al.* to more rapid PCR cycles (10 s at 60°C) favoring exponential amplification of shorter DNA fragments produced during Cut&Run[66]. For efficient removal of the primer peak from the library, a second post-amplification clean-up was included in the protocol, as suggested by the manufacturer. Sequencing (125 nt paired-end reads, HiSeq2000, Illumina) was performed by the DKFZ Genomics and Proteomics Core Facility (Heidelberg, Germany).

The galaxy server platform[67] was used for data analysis. In detail, adapter sequences were trimmed using Trim Galore! (https://www.bioinformatics.babraham.ac.uk/projects/trim_galore/; version 0.6.3) before aligning read sequences to the Drosophila genome (dm6) by Bowtie2[68,69] (version 2.4.2). Bowtie2 settings were adjusted according to Skene *et al.*[66] as follows: --local --very-sensitive-local --no-unal --no-mixed --no-discordant --phred33 -I 10 -X 700. Next, read duplicates were removed using MarkDuplicates (https://broadinstitute.github.io/picard/; version 2.18.2.2). Peak calling was performed by MACS2 callpeak[70,71] (version 2.1.1.20160309.6). Finally, differential binding was evaluated using DiffBind[72] (version 2.10.0) by grouping the samples according to treatment. Peaks were annotated by ChIPseeker[73] (version 1.18.0) using the genome annotation file from Ensembl (dm6, genes and gene prediction). Gene ontology (GO) enrichment analysis was performed with the online tool: http://www.webgestalt.org.

2.7 *Drosophila* stocks and clone induction in the wing disc

Typically, fly stocks were maintained at 25 °C with a 12 h light/dark cycle. Alternatively, crosses used in temperature-sensitive knockdown experiments using UAS/GAL4/tubulinG80^{ts} system were maintained at 18 °C and shifted to 29 °C to induce transgene expression. Crosses used for clone-induction experiments were kept at 18 °C before heat-shock for 20-25 min during mid third-instar larval stages at 33 °C. The high temperature activates the heat-shock-inducible promoter of a flipase (hsFLP) in random wing disc cells, resulting in removal of a stop cassette in the actin-promoter of a GAL4 (actin flip-out GAL4, AFG). This, in turn, induces stable transgene expression in the target cells and all subsequent daughter cells. After heat-shock, crosses were kept at 25 °C to allow for efficient gene expression. Fly lines used in this study are given in tables 4 and 5.

Tab. 4: List of used fly lines

AFG, actin flip-out GAL4; G4, GAL4; G80^{ts}, temperature-sensitive GAL80; GFP, green fluorescent protein; hh, hedgehog; hsFLP, heat-shock-inducible flipase; IFP, infra-red protein; mitoGFP, mitochondrially-targeted GFP; tsh, teashirt

fly line	source	product number
AFG;;UAS-GFP	Cohen lab	
hsFLP; sp;+/S-T	Cohen lab	
;tshG4	Fernando Casares	
;;tubulinG4/TM6b	Cohen lab	
;;tubulinG80^{ts}	Cohen lab	
UAS-AcCoAS	Bloomington	20761
;UAS-GFP	Cohen lab	
;UAS-GFP; hhG4/TM6b	Cohen lab	
;;UAS-IFP	Bloomington	64182
;UAS-mitoGFP/Cyo	Bloomington	8442
;;UAS-reaper/TM6b	Cohen lab	
;;UAS-SypHer3s-dmito	generated	
w[1118]	Bloomington	3605

Tab. 5: List of used RNAi fly lines

Numbering of the RNAi lines (#) used in this study is indicated. ATPCL, ATP citrate lyase; Elp3, Elongator complex protein 3; Gcn5, general control non-repressed protein 5; HDAC, histone deacetylase; nej, nejire; PDHa, pyruvate dehydrogenase α; PDK, pyruvate dehydrogenase kinase; Sirt, sirtuin

RNAi line	#	company	product number
ATPCL	1	Bloomington	65175
Elp3	1	VDRC	KK106128
Gcn5	1	VDRC	KK108943
HDAC1	1	Bloomington	33725
HDAC1	2	Bloomington	34846
HDAC1	3	Bloomington	31616
HDAC1	4	Bloomington	36800
HDAC3	1	VDRC	KK107073
HDAC3	2	Bloomington	64476
HDAC3	3	Bloomington	31633
HDAC3	4	Bloomington	34778
HDAC4	1	Bloomington	34774
HDAC4	2	Bloomington	34774
HDAC6	1	VDRC	KK108831
HDAC6	2	Bloomington	31053
HDAC6	3	Bloomington	34072
HDAC11	1	VDRC	KK108098
HDAC11	2	Bloomington	B32480
nej	1	VDRC	KK102885
nej	2	VDRC	KK105115
PDHa	1	VDRC	KK107209
PDK	1	VDRC	KK106641
Sirt1 (KK105502)	1	VDRC	KK105502
Sirt1 (B53697)	2	Bloomington	53697
Sirt1 (B31636)	3	Bloomington	31636
Sirt1 (B32481)	4	Bloomington	32481
Sirt1 (KK108241)	5	VDRC	KKK108241
Sirt2 (KK103790)	1	VDRC	KK103790
Sirt2 (B36868)	2	Bloomington	36868
Sirt2 (B31613)	3	Bloomington	31613
Sirt4 (KK110639)	1	VDRC	KK110639
Sirt 4 (B31638)	2	Bloomington	31638
Sirt 4 (B36588)	3	Bloomington	36588
Sirt 4 (B33984)	4	Bloomington	33984
Sirt6 (B34530)	1	Bloomington	34530
Sirt6 (B31399)	2	Bloomington	31399
Sirt6 (B36801)	3	Bloomington	36801
Sirt7 (B32483)	1	Bloomington	32483
Sirt7 (B31093)	2	Bloomington	31093
Sirt7 (B36802)	3	Bloomington	36802

3. Results

3.1 Non-uniform histone acetylation in the wing disc

Changes in cellular metabolism alter the concentrations of metabolic co-factors and substrates, which, in turn, impact the level of posttranslational protein modifications as shown for histones[74–77]. To investigate a potential non-uniform metabolism in the *Drosophila* wing imaginal disc, I analyzed the levels of histone acetylation and methylation, as metabolic read-outs, by immunostaining of discs of wandering third-instar larvae. H3K9 and H3K27 acetylation marks were uniformly distributed in the wing disc, whereas H3K18ac and H4K8ac showed a striking enrichment in the rim of the tissue (Fig. 7). Of note, this pattern was conserved throughout wing disc development as evidenced by comparable patterns for both non-uniform histone acetylation marks in early, mid, and late third-instar larval stages (Fig. 8). I excluded a non-uniform distribution of total histone 3 (H3) as the underlying reason for the observed H3K18ac pattern as the H3 immunosignal was uniform in the wing disc (Fig. 7).

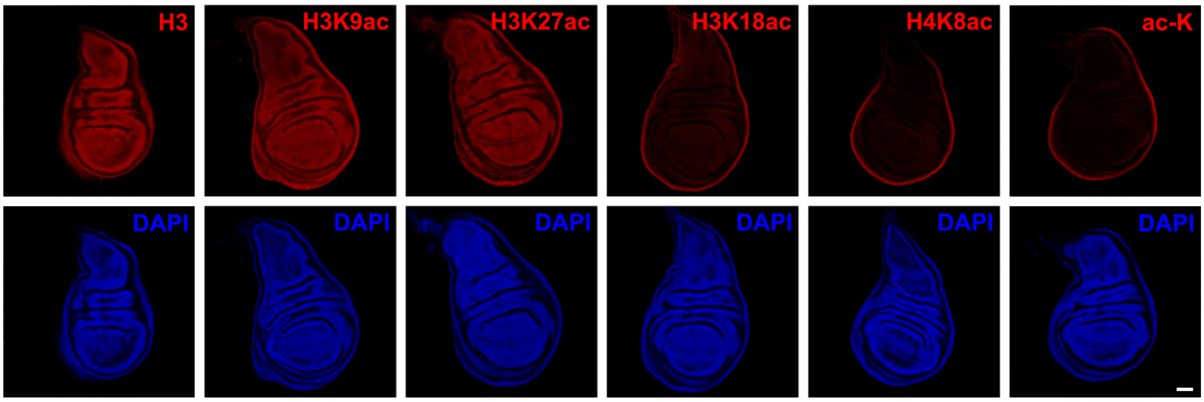

Fig. 7: Non-uniform histone acetylation in the wing disc
H3K18ac and H4K8ac as well as total acetylated lysine (ac-K) are enriched in the rim of the wing disc whereas total histone 3 (H3), H3K9ac, and H3K27ac are uniformly distributed. Acetylation levels (red) were assessed by immunostaining of the respective acetylation site in wing discs of wandering third-instar larvae. Nuclei were counterstained with DAPI (blue). Scale bar: 50 µm

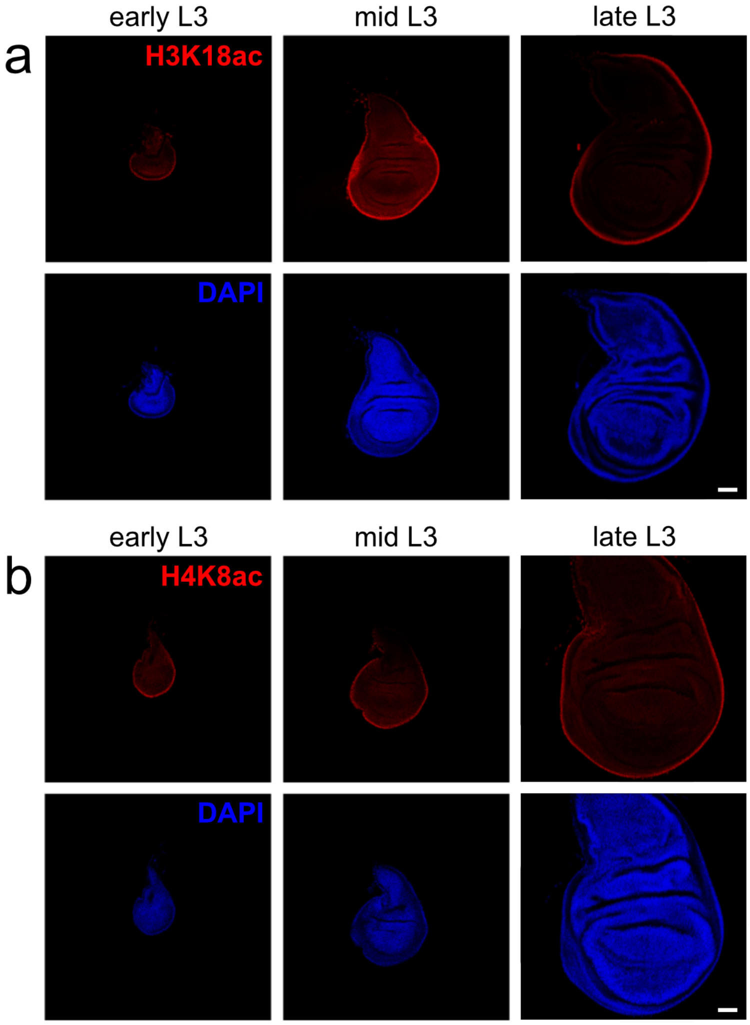

Fig. 8: Non-uniform histone acetylation during wing disc development
(**a**) H3K18ac and (**b**) H4K8ac marks are enriched in the wing disc rim throughout third-instar larval stages (early to late L3). Histone acetylation levels (red) were assessed by immunostaining of the respective acetylation site in wing discs. Nuclei were counterstained with DAPI (blue). Scale bars: 50 µm

Histone acetylation is associated with euchromatin, as this modification neutralizes the positive charge of the modified lysine which weakens the interaction between these proteins and the negatively charged genomic DNA[12,13,23]. It also regulates gene expression by affecting the recruitment of DNA-binding proteins such as transcriptional co-activators. As predicted for histone acetylation, and confirming the specificity of the used antibodies, all tested histone acetylation marks in peripodial nuclei were excluded from highly compacted genomic DNA (i.e., heterochromatin), characterized by high DAPI signal (Fig. 9). Next, I tested whether a uniform or a non-uniform distribution of histone acetylation, as shown by H3K9ac and H3K27ac or H3K18ac and H4K8ac, respectively, is the predominant pattern in the wing disc. Hence, I used immunostaining for total acetylated lysine (ac-K) to visualize general acetylation levels in this tissue (Fig. 7). Enrichment of ac-K specifically in the rim of the disc suggested a general trend for higher acetylation in this tissue region, while uniform patterns for H3K9ac and H3K27ac likely represented only a minor form of histone acetylation. Of note, the ac-K immunosignal was mainly nuclear and, similar to histone acetylation, displayed a preferential association with euchromatin (Fig. 9).

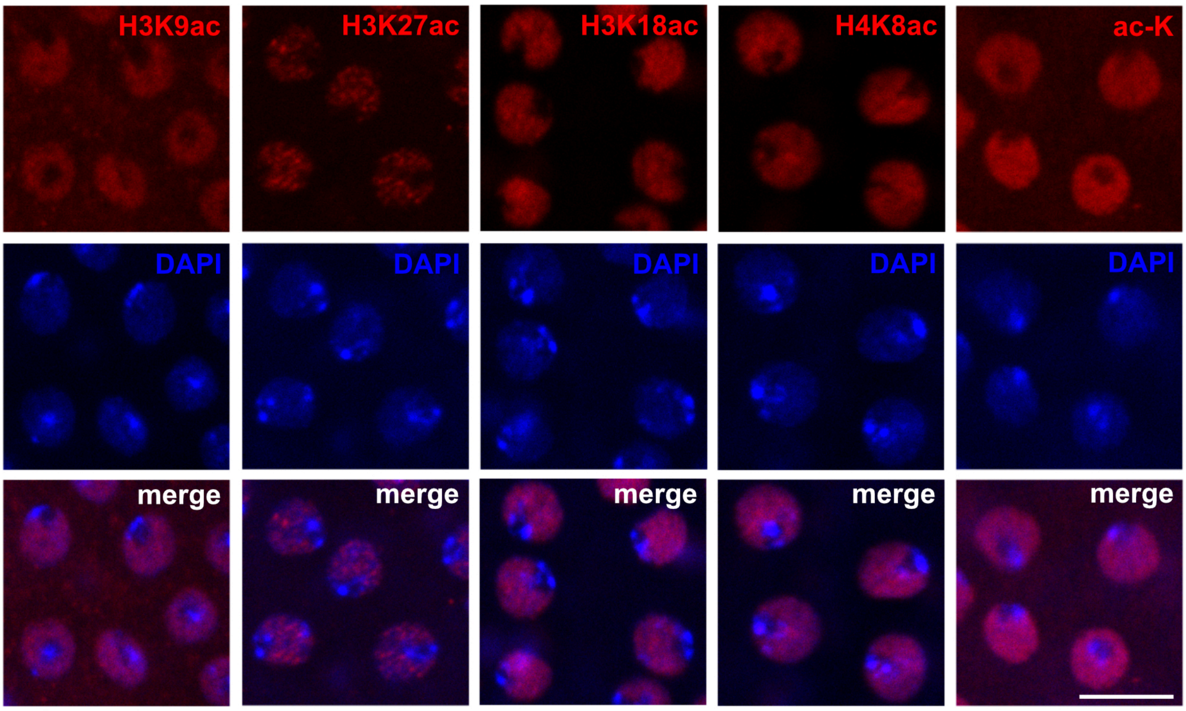

Fig. 9: Euchromatin-enrichment of acetylation marks
Images of peripodial nuclei show enrichment of H3K9ac, H3K27ac, H3K18ac, and H4K8ac as well as total acetylated lysine (ac-K) in euchromatin as their immunosignals are excluded from highly compacted DNA regions indicated by high DAPI signal. Acetylation levels (red) were assessed by immunostaining of the respective acetylation site in wing discs of wandering third-instar larvae. Nuclei were counterstained with DAPI (blue). Images are given in single or merged channel configurations. Scale bar: 10 µm

Immunostaining of histone methylation marks, including mono-, di-, and tri-methylation of H3K9 as well as H3K36me3, displayed a rather uniform distribution in the wing disc (Fig. 10). Contrasting euchromatin-associated histone acetylation, methylation can be associated with hetero- or euchromatin, depending on the methylation mark. Performing co-staining for DAPI and methylation marks, I documented that H3K9me1 was present throughout the nucleus, whereas heterochromatin-associated H3K9me2 and H3K9me3 co-localized with highly compacted DNA (Fig. 11)[78]. In contrast, euchromatin-associated H3K36me3 was excluded from compacted genomic DNA, similar to the distribution of histone acetylation marks[78]. Interestingly, the patterns for heterochromatin-associated H3K9me2 and euchromatin-associated H3K36me3 anti-correlated in the rim of the wing disc, showing slightly decreased and increased levels in this part of the tissue, respectively (Fig. 10).

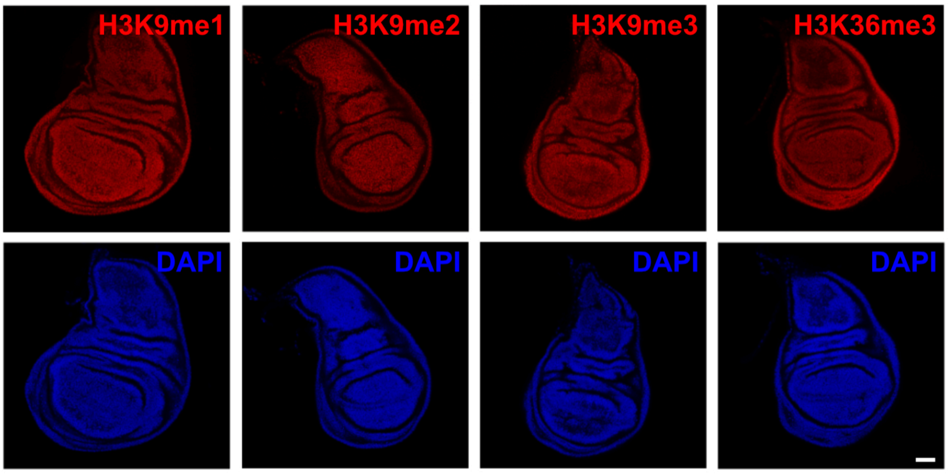

Fig. 10: Uniform histone methylation in the wing disc
Histone methylation marks H3K9me1, H3K9me2, H3K9me3, and H3K36me3 show a rather uniform distribution in the wing disc. Euchromatin-associated H3K36me3 is slightly enriched while heterochromatin-associated H3K9me2 is slightly decreased in the rim of the disc compared to the rest of the tissue, suggesting a more open chromatin state in the rim. Histone methylation levels (red) were assessed by immunostaining of the respective methylation site in wing discs of wandering third-instar larvae. Nuclei were counterstained with DAPI (blue). Scale bar: 50 µm

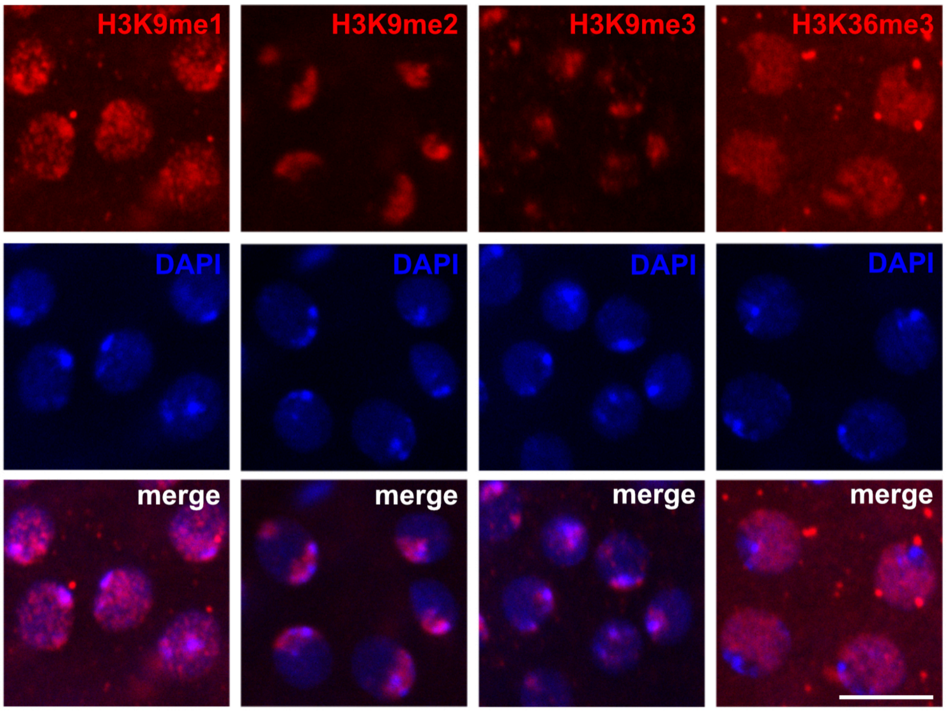

Fig. 11: Distinct subnuclear localizations of histone methylation marks
Images of peripodial nuclei suggest enrichment of H3K36me3 in euchromatin as its immunosignal is excluded from highly compacted DNA regions characterized by high DAPI signal. By contrast, H3K9me2 and H3K9me3 are associated with these heterochromatic regions. H3K9me1 is present throughout the nucleus. Histone methylation levels (red) were assessed by immunostaining of the respective methylation site in wing discs of wandering third-instar larvae. Nuclei were counterstained with DAPI (blue). Images are given in single or merged channel configurations. Scale bar: 10 µm

Taken together, non-uniform patterns of H3K18ac and H4K8ac as well as of total ac-K with high levels in the rim of the wing disc argued for a non-uniform cellular metabolism affecting histone acetylation in this tissue. Nuclear localization of ac-K immunosignal further indicated that histones represent the major portion of proteins acetylated in the rim of the wing disc. Finally, enrichment of euchromatin-associated histone marks H3K18ac, H4K8ac, and H3K36me3 but decreased levels of heterochromatin-associated H3K9me2 in the rim of the wing disc, suggested a generally open and, hence, transcriptionally more active chromatin state in these cells. For the further course of my PhD project, I mainly focused on H3K18ac as a representative example of the non-uniform histone acetylation marks observed in the wing disc.

3.2 Nuclear positioning in the wing disc tissue defines H3K18ac levels

To understand the cellular mechanisms underlying a non-uniform H3K18ac pattern in the wing disc, I studied cross-sections of this tissue immunostained for H3K18ac. Schematic representation of wing disc x-y sections and cross-sections are shown in figure 12. Immunostained cross-sections revealed a distinct pattern, in which not all nuclei in the proximal rim (Fig. 12, green) displayed high levels of H3K18ac, but only nuclei that faced towards the outside surface of the wing disc (Fig. 13a, solid arrowheads). In contrast, nuclei that were localized in folds facing the tissue interior or that were generally more inward-facing, had low levels of H3K18ac (Fig. 13a, open arrowheads). High H3K18ac was also observed in the peripodial membrane and mildly elevated in the apical pouch, both facing the tissue exterior. A schematic representation of this H3K18ac pattern in the wing disc is displayed in figure 13b.

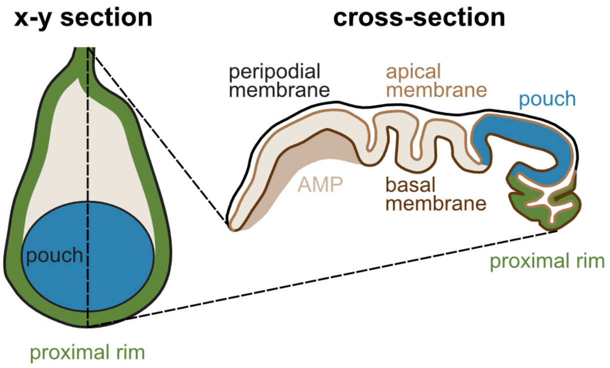

Fig. 12: Schematic representations of a wing disc of a third-instar larvae
Schematic representations of a wing disc of a third-instar larvae in x-y section or cross-section. Wing pouch and proximal rim are shown in blue and green, respectively. The schematics also illustrate the positions of peripodial membrane (black), apical (light brown) and basal membranes (dark brown), as well as the localization of adult muscle precursors (AMP; beige). Dashed lines indicate the position of the cross-section.

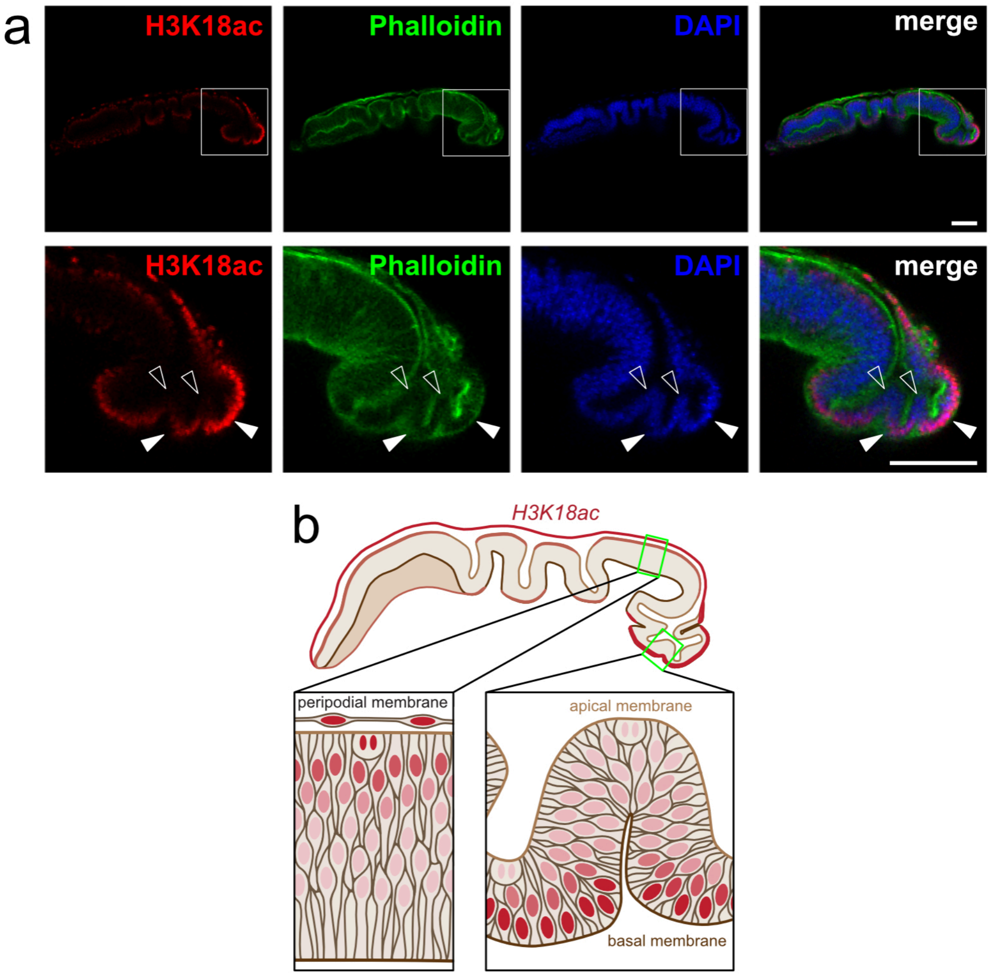

Fig. 13: High H3K18ac in outward-facing nuclei
(**a**) Cross-sections of wing discs show increased H3K18ac (red) in nuclei facing the surface of the disc tissue (solid arrowheads) but not in nuclei facing the tissue interior (open arrowheads). The white boxes in the overview images indicate the zoomed-in areas shown in the panels below. H3K18ac levels were assessed by immunostaining in wing discs of wandering third-instar larvae (red). Nuclei were counterstained with DAPI (blue). The disc outline is visualized by Phalloidin staining (green). Images are given in single or merged channel configurations. Scale bars: 50 µm (**b**) Schematic representation of the H3K18ac pattern in a cross-section of the entire wing disc (above) or zoom-ins of the pouch and rim (below left and right, respectively). Intensities of red from light to dark indicate increasing levels of H3K18ac in the respective nuclei.

Several mechanisms may be envisioned to cause the observed non-uniform H3K18ac pattern in the wing disc, including regulation by the cell cycle, the clonal heritage, or the localization of the nucleus within this tissue. The *Drosophila* wing disc is a pseudostratified epithelium, a monolayer of cells in which each cell stretches from the basal to the apical side of the tissue. Like in all pseudostratified epithelia, nuclei in the wing disc move between basal and apical sides of the cell during the cell cycle, undergoing mitosis apically. This position allows for the space required for the morphological changes (rounding up) of the cell during mitosis[25,79]. However, the relative position of apical mitotic nuclei within the wing disc is not fixed as it depends on the position of the cell in the tissue folds facing towards the tissue interior or exterior (Fig. 14b). I tested the correlation of H3K18ac levels with the cell cycle by co-immunostaining for mitotic marker phospho-H3 serine 10 (pH3 S10). However, apical pH3 S10-positive cells display higher H3K18ac levels in the wing pouch (Fig. 14a, solid arrowheads) but low levels in the proximal rim (Fig. 14a, open arrowhead). These results excluded a correlation of H3K18ac levels with the cell cycle.

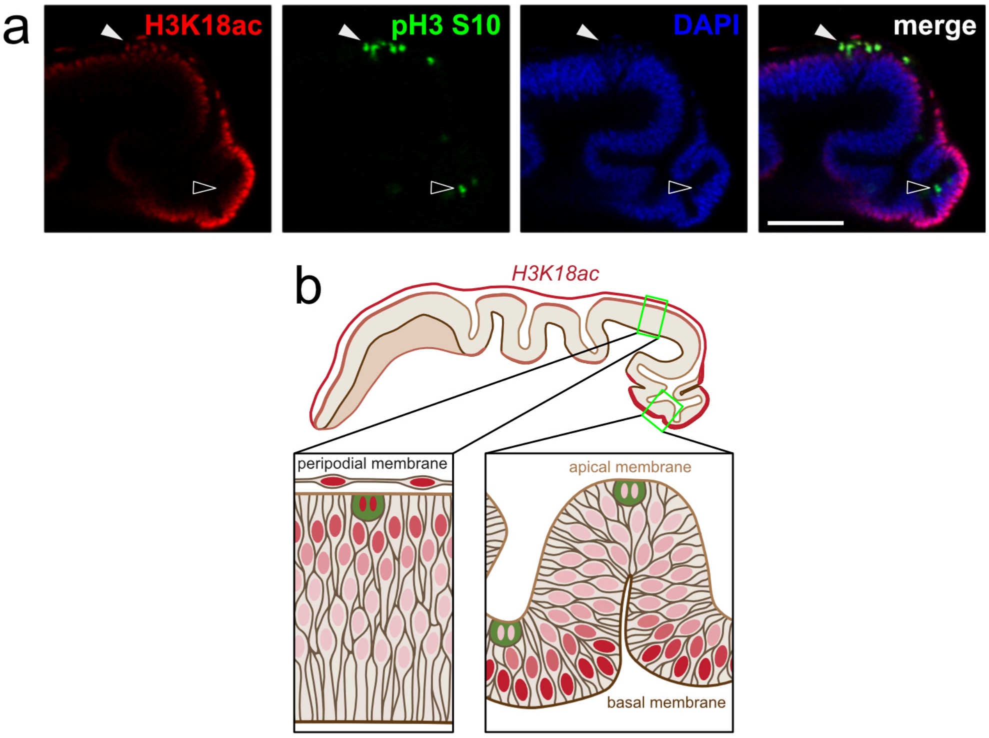

Fig. 14: Cell cycle phase does not define H3K18ac levels
(**a**) H3K18ac levels (red) do not correlate with the cell cycle phase, as exemplary mitotic phospho-H3 serine 10 (pH3 S10)-positive nuclei (green) have higher H3K18ac in the wing pouch (solid arrowhead) but low H3K18ac in proximal regions (open arrowhead). H3K18ac and pH3 S10 levels were assessed by immunostaining in wing discs of wandering third-instar larvae. Nuclei were counterstained with DAPI (blue). Images are given in single or merged channel configurations. Scale bar: 50 µm (**b**) Schematic representation of the H3K18ac pattern (red) in a cross-section of the entire wing disc (above) or zoom-ins of the pouch and rim (below left and right, respectively). Intensities of red from light to dark indicate increasing levels of H3K18ac in the respective nuclei. Mitotic cells are highlighted in green.

To investigate the importance of clonal heritage in generating a non-uniform acetylation pattern, I traced the lineage of individual cells in the wing disc. To do so, I exposed larvae encoding a flipase with a heat shock-inducible promoter to heat shock, activating transgene expression in random cells (see Material and Methods section 2.7 for details). Induced flipase expression resulted in removal of a stop cassette in the promoter of actinGAL4, causing stable expression of GFP in the target cell and all subsequent daughter cells. As exemplified in a cross-section of a wing disc (Fig. 15a), I identified individual clones with nuclei having high (lower arrowhead), medium (middle arrowhead), or low levels of H3K18ac (upper arrowhead). Even though being in the same disc compartment and just one or two cell cycles apart, the acetylation levels markedly differ between these clonal cells depending on the nuclear position within the tissue (Fig. 15b). The observation that cells with the same cell identity show differing levels of histone acetylation excluded a regulatory role for clonal heritage in establishing a non-uniform H3K18ac pattern. Rather, the result argued for nuclear positioning within the tissue as the determining factor for the observed non-uniform pattern. To further corroborate this conclusion, I induced expression of reaper in the teashirt (tsh)-expression domain (Fig. 16a, GFP+) that encompasses the majority of cells with high H3K18ac. Reaper activates apoptosis by preventing proteasomal degradation of caspases[80,81]. Eliminating the rim of the wing disc in the proximal compartment exposed the underlying cells of a different cellular origin to the outside of the tissue and caused the formation of a new H3K18ac rim in the remaining disc (Fig. 16b).

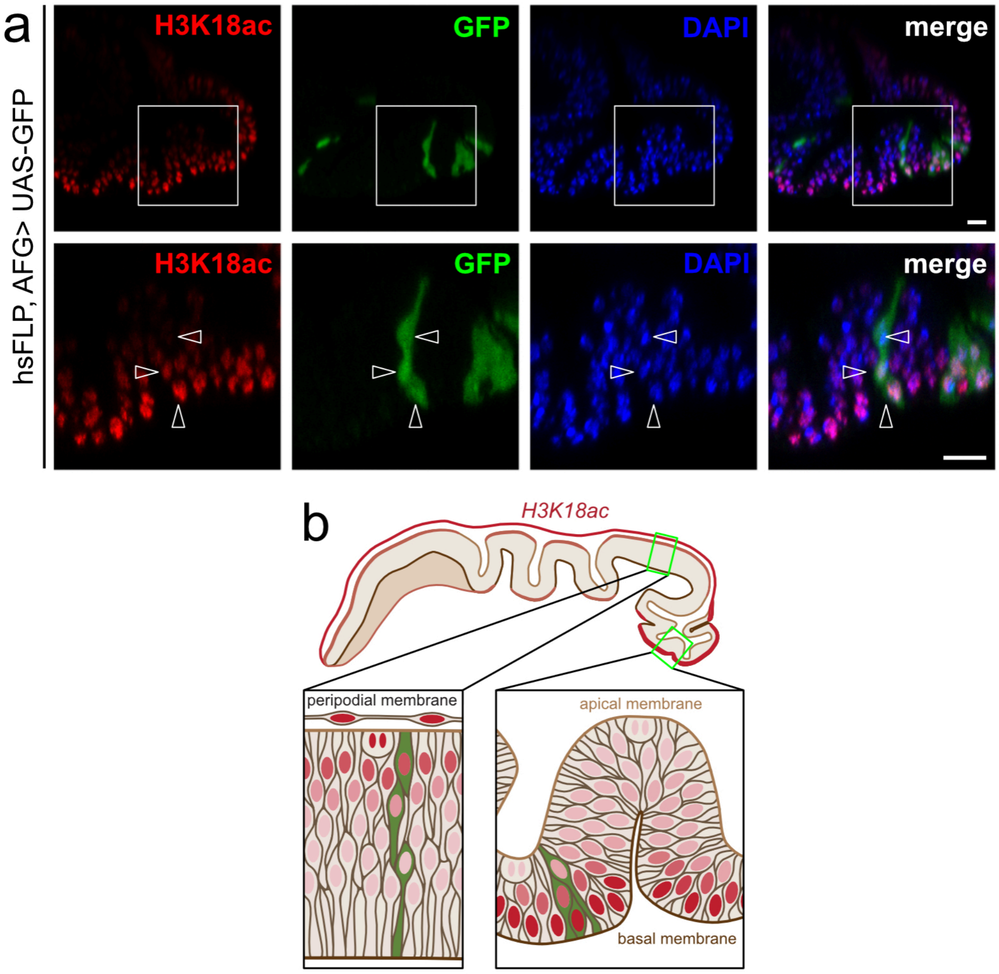

Fig. 15: Clonal heritage does not define H3K18ac levels
(**a**) H3K18ac levels (red) do not depend on clonal heritage. Arrowheads indicate 3 nuclei of a GFP-expressing clone (green) with high (lower arrowhead), medium (middle arrowhead) or low levels of H3K18ac (upper arrowhead) depending on the nuclear position within the wing disc tissue. Clonal labeling in the wing disc was performed by heat shock induced expression of GFP (green; see Material and Methods section 2.7 for details). H3K18ac levels were assessed by immunostaining in wing discs of wandering third-instar larvae. Nuclei were counterstained with DAPI (blue). The white boxes in the overview images indicate the zoomed-in areas shown in the panels below. Images are given in single or merged channel configurations. Scale bars: 10 µm (**b**) Schematic representation of the H3K18ac pattern (red) in a cross-section of the entire wing disc (above) or zoom-ins of the pouch and rim (below left and right, respectively). Intensities of red from light to dark indicate increasing levels of H3K18ac in the respective nuclei. Clonal cells are highlighted in green.

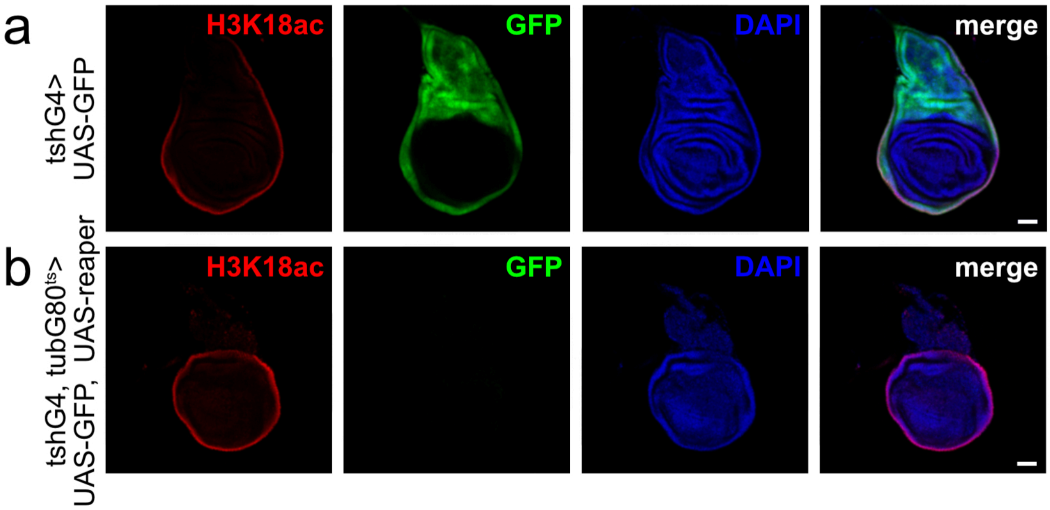

Fig. 16: Nuclear positioning in the tissue defines H3K18ac levels
H3K18ac levels (red) do not depend on cell identity but rather nuclear position within the tissue. (**a**) High H3K18ac signal is seen in cells in the teashirt (tsh)-expression domain (GFP+, green). (**b**) Elimination of this domain by tshGAL4 (tshG4)-driven expression of reaper causes the formation of a new rim of H3K18ac-positive nuclei. These cells do not express tshG4 and, hence, lack GFP expression. Cell death was induced by temperature-sensitive expression of reaper for 1 day at 29°C. H3K18ac levels were assessed by immunostaining in wing discs of wandering third-instar larvae. Nuclei were counterstained with DAPI (blue). Images are given in single or merged channel configurations. Scale bars: 50 µm

So far, my data suggested that high levels of H3K18ac were not dependent on cell cycle or cellular lineage but reflected an outward-facing position of nuclei within the wing disc tissue. A possible mechanism how cells sense nuclear position in the wing disc may be through positional cues from the hemolymph. My hypothesis that exposure to the hemolymph might act as an instructive signal for histone acetylation was supported by immunostaining of wing discs for lipoproteins (lpp). Lipoproteins are synthesized in the fat body and circulate in the hemolymph, before being taken up by hemolymph-exposed tissue regions of the wing disc[12,1382]. Immunosignal of lpp on outward-facing membranes correlated with high levels of H3K18ac, as seen with two independent lpp antibodies (Figs. 17 and 18). This correlation persisted even when a new rim was formed in wing discs after reaper-induced apoptosis in the tsh-expression domain (Fig. 19).

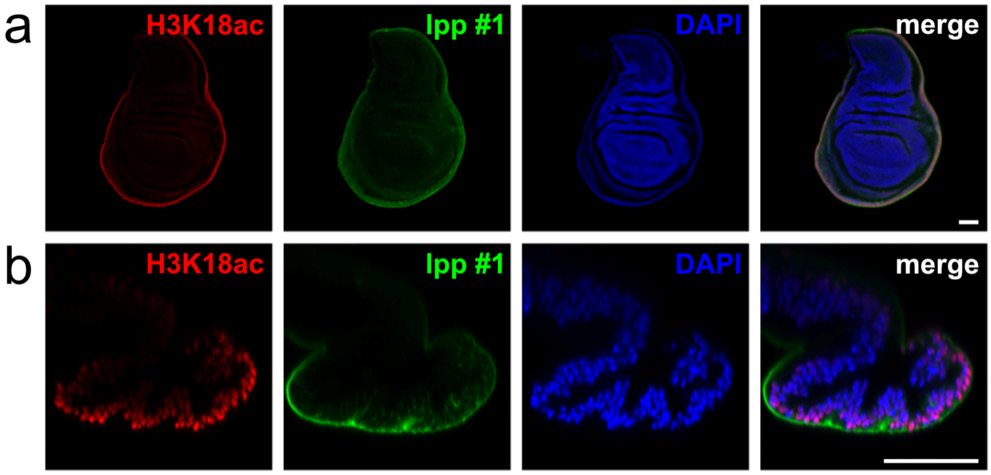

Fig. 17: Exposure of cells to the hemolymph correlates with H3K18ac levels
Nuclei with high H3K18ac (red) face the surface of the wing disc tissue and are in contact with the hemolymph, as seen by immunostaining for hemolymph-derived lipoproteins (lpp, green). Images are depicted in (**a**) x-y section or (**b**) cross-section. H3K18ac and lpp levels were assessed by immunostaining in wing discs of wandering third-instar larvae. Nuclei were counterstained with DAPI (blue). Images are given in single or merged channel configurations. Scale bars: 50 µm

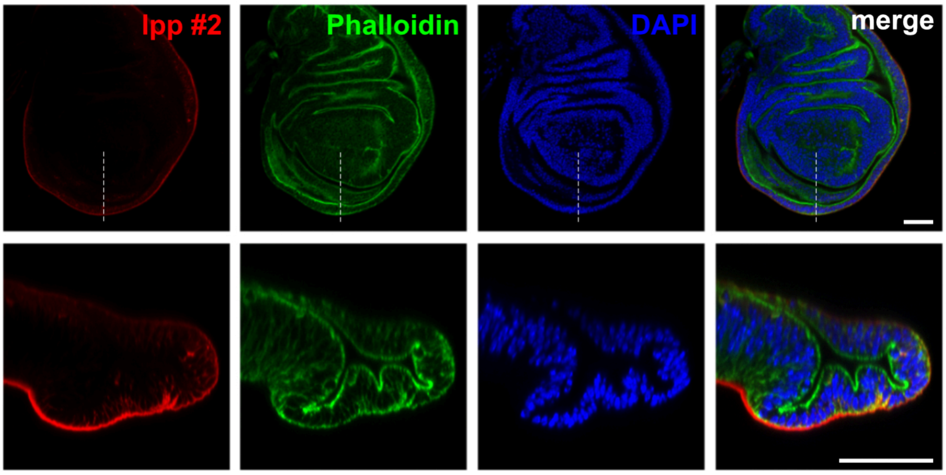

Fig. 18: Enrichment of lipoproteins on outward-facing membranes of the wing disc
Immunosignal of lipoproteins (lpp, red), detected using a second antibody (#2), is also enriched on outward-facing cell membranes of the wing disc. The dashed lines in the overview images indicate the position of the cross-section shown in the panels below. Levels of lpp were assessed by immunostaining in wing discs of wandering third-instar larvae. Nuclei were counterstained with DAPI (blue). The disc outline is visualized by Phalloidin staining (green). Scale bars: 50 µm

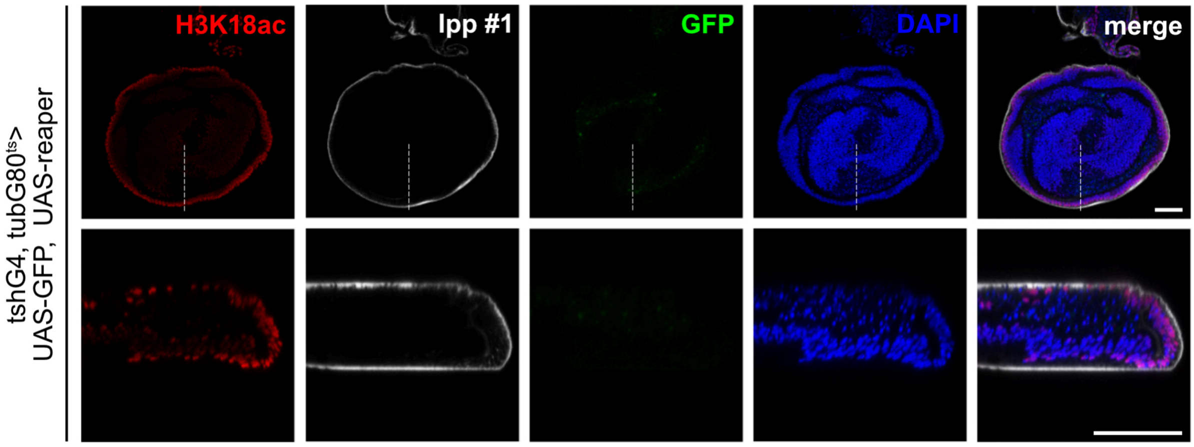

Fig. 19: Exposure to the hemolymph correlates with H3K18ac levels after formation of new disc rim
The formation of a new rim of H3K18ac-positive nuclei (red) following elimination of the teashirt (tsh)-expression domain (GFP+, green) by reaper expression correlates with high levels of lipoproteins (lpp, white) on outward-facing cell membranes. Cell death was induced by temperature-sensitive expression of reaper for 1 day at 29°C. The dashed lines in the overview images indicate the position of the cross-section shown in the panels below. H3K18ac and lpp levels were assessed by immunostaining in wing discs of wandering third-instar larvae. Nuclei were counterstained with DAPI (blue). Images are given in single or merged channel configurations. Scale bars: 50 µm

3.3 Non-uniform histone acetylation is caused by localized acetylation

Conceptually, a non-uniform acetylation pattern with high levels of H3K18ac in the rim of the discs may be achieved by two different mechanisms, namely by uniform acetylation and local deacetylation in the center of the disc or by local acetylation in the rim. To be able to distinguish between these two possibilities, I first identified the enzymes involved in modifying and de-modifying H3K18.

To determine the H3K18-specific histone acetyltransferase, I knocked down the histone acetyltransferases nejire (nej), general control non-repressed protein 5 (Gcn5), and Elongator complex protein 3 (Elp3) individually in the posterior compartment of the wing disc and analyzed the consequences for the histone acetylation by immunostaining (Figs. 20-22). I chose these enzymes as they had been implicated previously in acetylation of H3K18 in human and yeast[83–85]. Knockdown of nej caused loss of H3K18ac, H4K8ac, and H3K27ac but did not impact H3K9ac (Fig. 20). Enzyme knockdown also strongly reduced the size of the posterior wing disc compartment, marked by GFP expression, suggesting an essential role for nej activity in cell viability. In contrast, knockdown of Gcn5 did not impact H3K18ac but caused loss of H3K9ac and slightly decreased H3K27ac and posterior compartment size, marked by GFP expression (Fig. 21). Knockdown of Elp3 neither impacted H3K18ac nor H3K9ac (Fig. 22). As prolonged nej knockdown affected wing disc morphology, I wanted to exclude secondary effects as the reason for reduced H3K18ac levels upon enzyme knockdown. Temperature-sensitive expression of two independent nej RNAi lines for only one day using the GAL4/G80^{ts}-system did not impact wing disc morphology but still caused loss of the H3K18ac immunosignal (Fig. 23). Interestingly, temperature-sensitive knockdown of nej with two independent RNAi lines for only one day also strongly decreased ac-K levels, indicating a central role for nej in the acetylation of nuclear proteins in the wing disc (Fig. 24).

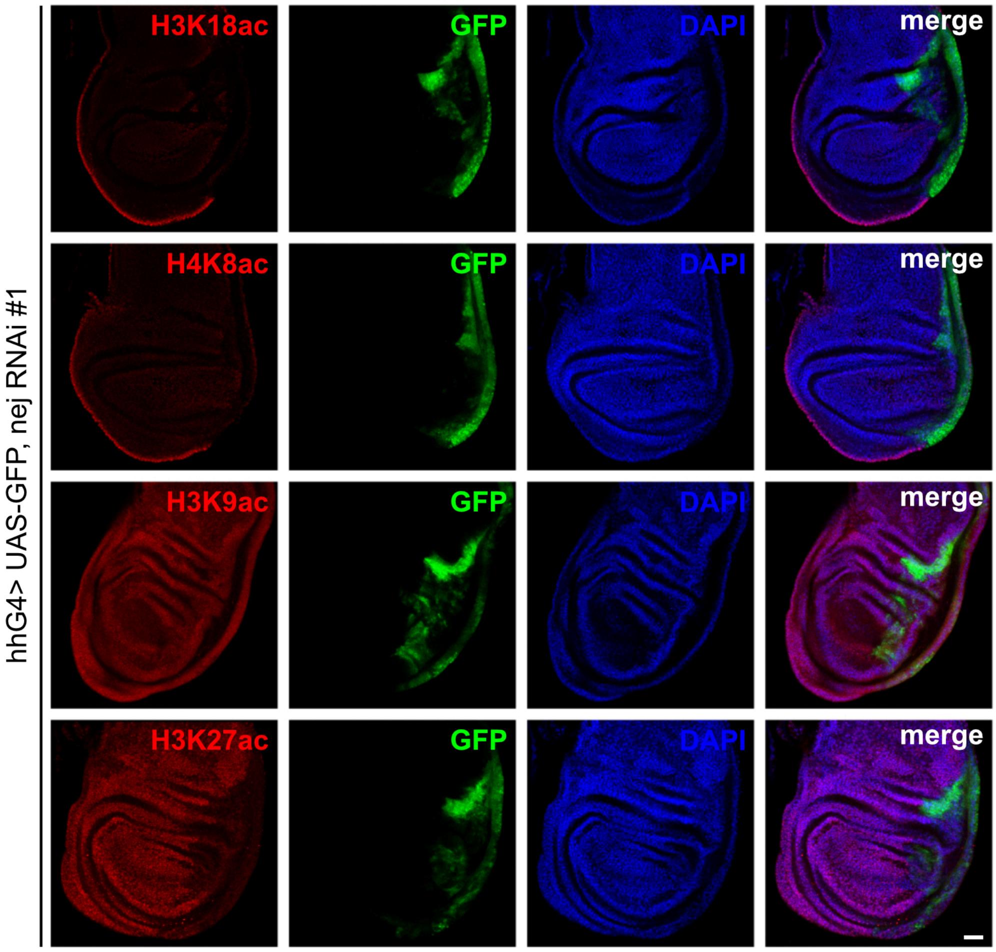

Fig. 20: Knockdown of nejire decreases H3K18ac, H4K8ac, and H3K27ac
Knockdown of nejire (nej) in the posterior compartment (GFP+, green), driven by hedgehogGAL4 (hhG4), strongly decreases acetylation of H3K18, H4K8, and H3K27, but not of H3K9. Additionally, the size of the posterior wing disc is strongly reduced upon enzyme knockdown. Histone acetylation levels (red) were assessed by immunostaining of the respective acetylation site in wing discs of wandering third-instar larvae. Nuclei were counterstained with DAPI (blue). Images are given in single or merged channel configurations. Scale bar: 50 µm

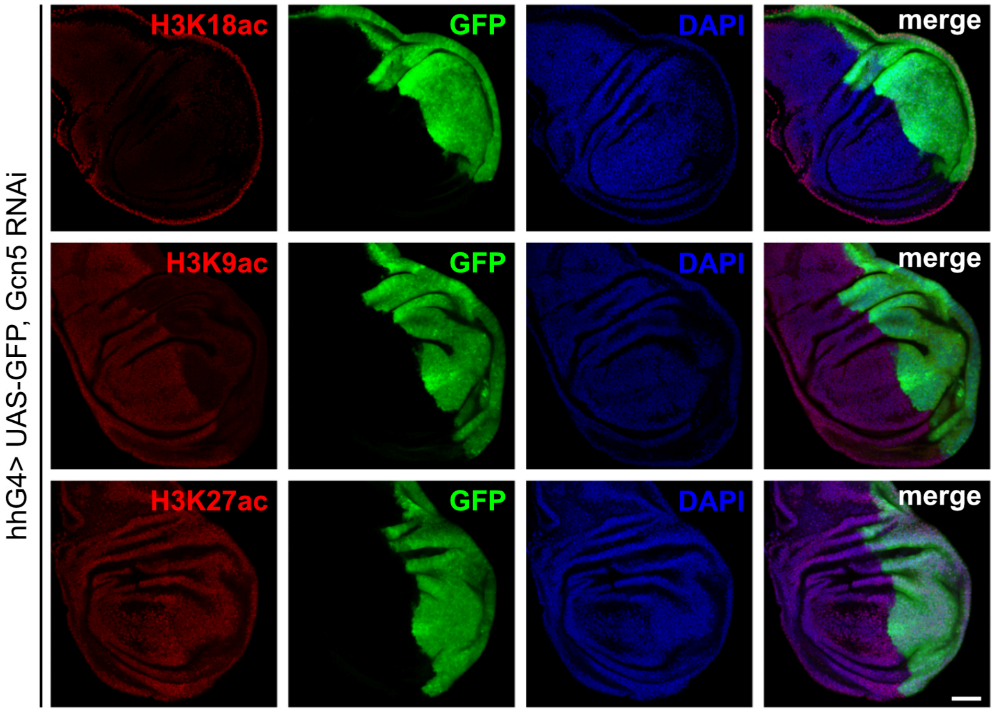

Fig. 21: Knockdown of general control non-repressed protein 5 decreases H3K9ac and H3K27ac
Knockdown of general control non-repressed protein 5 (Gcn5) in the posterior compartment (GFP+, green), driven by hedgehogGAL4 (hhG4), strongly decreases acetylation of H3K9 and mildly of H3K27 but does not impact H3K18ac. Additionally, the size of the posterior wing disc (GFP+, green) is slightly reduced upon enzyme knockdown. Histone acetylation levels (red) were assessed by immunostaining of the respective acetylation site in wing discs of wandering third-instar larvae. Nuclei were counterstained with DAPI (blue). Images are given in single or merged channel configurations. Scale bar: 50 µm

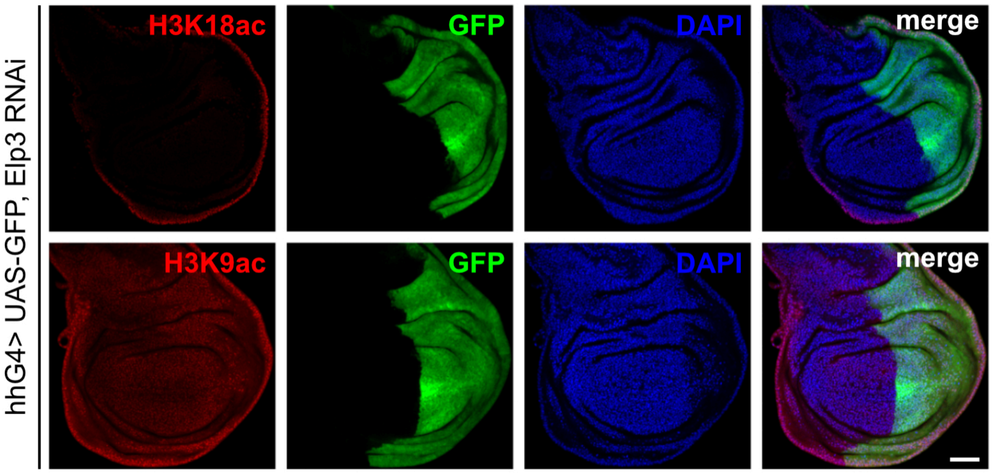

Fig. 22: Knockdown of Elongator complex protein 3 does not affect histone acetylation
Knockdown of Elongator complex protein 3 (Elp3) in the posterior compartment (GFP+, green), driven by hedgehogGAL4 (hhG4), does not affect acetylation of H3K18 or H3K9. Histone acetylation levels (red) were assessed by immunostaining of the respective acetylation site in wing discs of wandering third-instar larvae. Nuclei were counterstained with DAPI (blue). Images are given in single or merged channel configurations. Scale bar: 50 µm

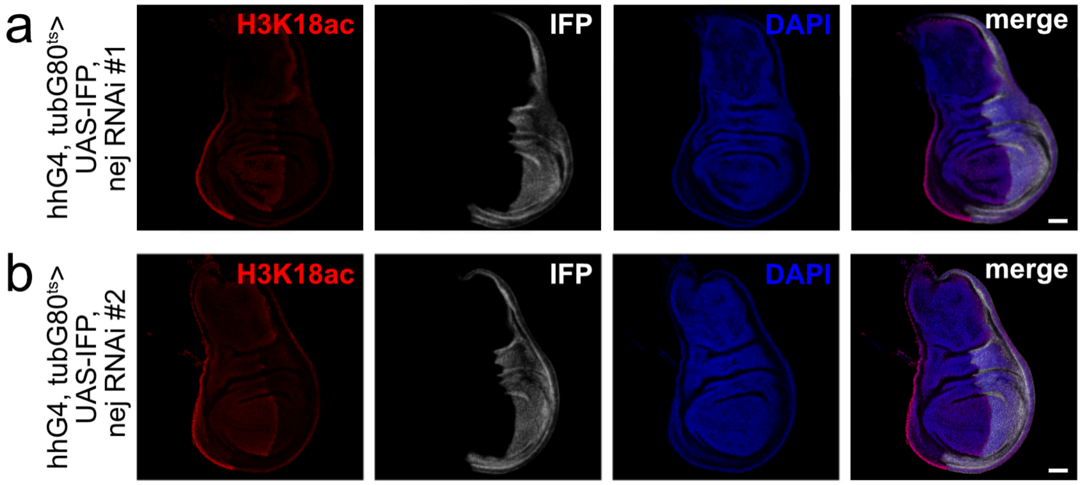

Fig. 23: Knockdown of nejire decreases H3K18ac
Knockdown of nejire (nej) in the posterior compartment (infra-red protein+, IFP+, white), driven by hedgehogGAL4 (hhG4), strongly decreases acetylation of H3K18 (red). This effect is seen for two independent RNAi lines (**a**, **b**). Temperature-sensitive knockdown of nej was induced for 1 day at 29°C. H3K18ac levels were assessed by immunostaining in wing discs of wandering third-instar larvae. Nuclei were counterstained with DAPI (blue). Images are given in single or merged channel configurations. Scale bars: 50 µm

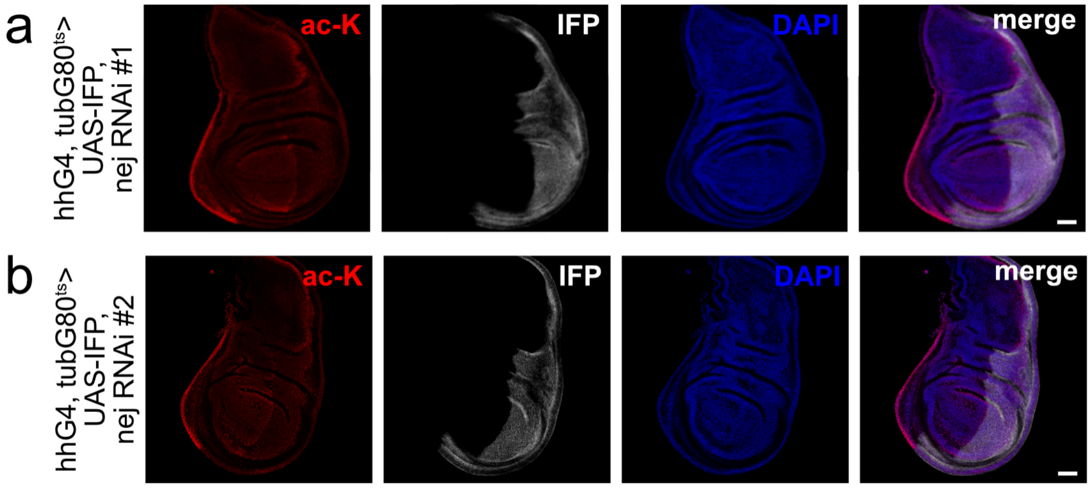

Fig. 24: Knockdown of nejire decreases total acetylated lysine levels
Knockdown of nejire (nej) in the posterior compartment (infra-red protein+, IFP+, white), driven by hedgehogGAL4 (hhG4), strongly decreases total acetylated lysine (ac-K) levels (red). This effect is seen for two independent RNAi lines (**a**, **b**) and indicates a central role for nej in protein acetylation in the wing disc. Temperature-sensitive knockdown of nej was induced for 1 day at 29°C. Levels of ac-K were assessed by immunostaining in wing discs of wandering third-instar larvae. Nuclei were counterstained with DAPI (blue). Images are given in single or merged channel configurations. Scale bars: 50 µm

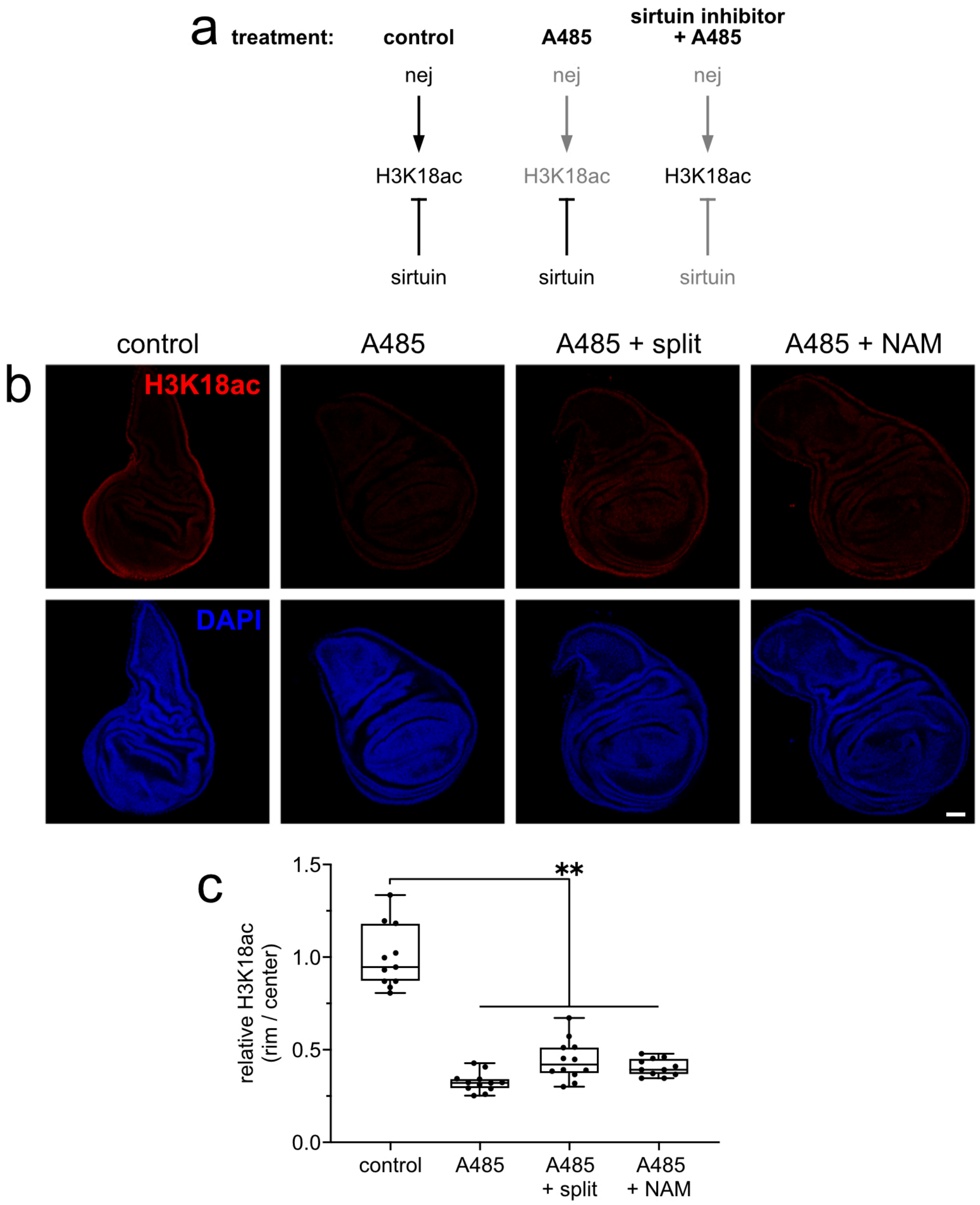

Fig. 25: Sirtuins do not deacetylate H3K18ac
(**a**) Experimental strategy to test the role of sirtuins (class III histone deacetylases) in the deacetylation of H3K18ac. Under control conditions, nej acetylates H3K18, which is deacetylated at a lower rate by a deacetylase, resulting in H3K18ac marks. Inhibition of nej by A485 prevents new H3K18ac, resulting in loss of the histone mark due to active deacetylation. Co-treatment of discs with the nej inhibitor and a sirtuin inhibitor should prevent loss of H3K18ac, if this mark is deacetylated by a sirtuin. (**b-c**) H3K18ac (red) is not deacetylated by sirtuins as pharmacological inhibition with splitomycin (split, 50 µM) or nicotinamide (NAM, 20 mM) does not prevent loss of H3K18ac upon nejire (nej) inhibition by A485 (20 µM). Wing discs of wandering third-instar larvae were incubated for 2 h in explant cultures with the indicated inhibitors before immunostaining of H3K18ac and nuclear counterstain with DAPI (blue). Representative images are shown in (b) and quantified in (c) with relative H3K18ac signal intensity expressed as a ratio of signal in the rim versus center of the disc. Statistical significance was determined by Kruskal-Wallis test with Dunn's multiple comparisons test (n=11-12 discs from 2 independent experiments; ** <0.01). Scale bar: 50 µm

Next, I wished to determine the HDAC that deacetylates H3K18ac. HDACs either belong to the metabolite-dependent sirtuins (HDAC class III) or to the metabolite-independent HDAC classes I, II, and IV[18,19]. As a non-uniform histone acetylation pattern suggested a non-uniform metabolism in the wing disc, I first considered metabolite-dependent sirtuins as candidate deacetylases. Thus, I treated discs with the nej inhibitor A485 in the absence or presence of sirtuin inhibitors splitomicin (split) or nicotinamide (NAM). I reasoned that inactivation of sirtuin should prevent loss of H3K18ac upon nej inhibition if H3K18ac was deacetylated by a class III HDAC (Fig. 25a). Nej inhibition with A485 caused loss of H3K18ac (Fig. 25b-c). However, no rescue of H3K18ac levels upon A485 treatment by splitomicin or nicotinamide was observed in these experiments.

In line with these results, knockdown of neither member of the sirtuins, namely Sirt1, Sirt2, Sirt4, Sirt6, or Sirt7 affected H3K18ac levels (Figs. 26-30). I validated these findings with at least three independent RNAi lines for each sirtuin. Knockdown of the different sirtuins also did not impact H3K9ac or H3K27ac levels. Only knockdown of Sirt1 with RNAi #2 strongly reduced posterior compartment size, marked by GFP expression (Fig. 26b).

Fig. 26 (next page): Knockdown of sirtuin 1 does not affect histone acetylation
(**a**) Knockdown of sirtuin 1 (Sirt1) in the posterior compartment (GFP+, green), driven by hedgehogGAL4 (hhG4), does not affect acetylation of H3K18, H3K9, or H3K27. (**b**-**e**) The effect of Sirt1 knockdown on H3K18ac was validated with four additional independent RNAi lines, none showing an impact on H3K18ac levels. Histone acetylation levels (red) were assessed by immunostaining of the respective acetylation site in wing discs of wandering third-instar larvae. Nuclei were counterstained with DAPI (blue). Images are given in single or merged channel configurations. Scale bars: 50 µm

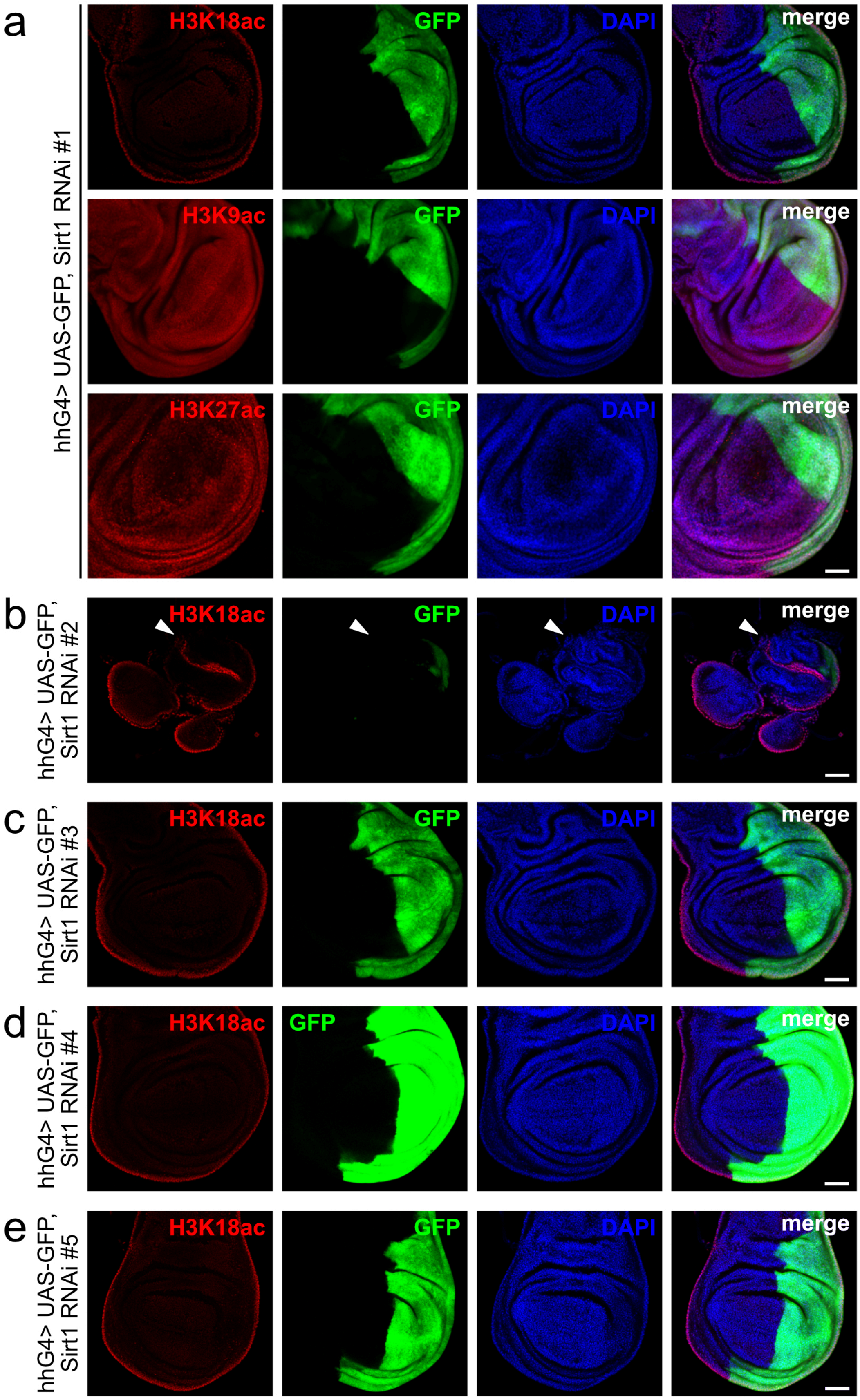
a
hhG4> UAS-GFP, Sirt1 RNAi #1
H3K18ac
GFP
DAPI
merge
H3K9ac
GFP
DAPI
merge
H3K27ac
GFP
DAPI
merge
b
hhG4> UAS-GFP, Sirt1 RNAi #2
H3K18ac
GFP
DAPI
merge
c
hhG4> UAS-GFP, Sirt1 RNAi #3
H3K18ac
GFP
DAPI
merge
d
hhG4> UAS-GFP, Sirt1 RNAi #4
H3K18ac
GFP
DAPI
merge
e
hhG4> UAS-GFP, Sirt1 RNAi #5
H3K18ac
GFP
DAPI
merge

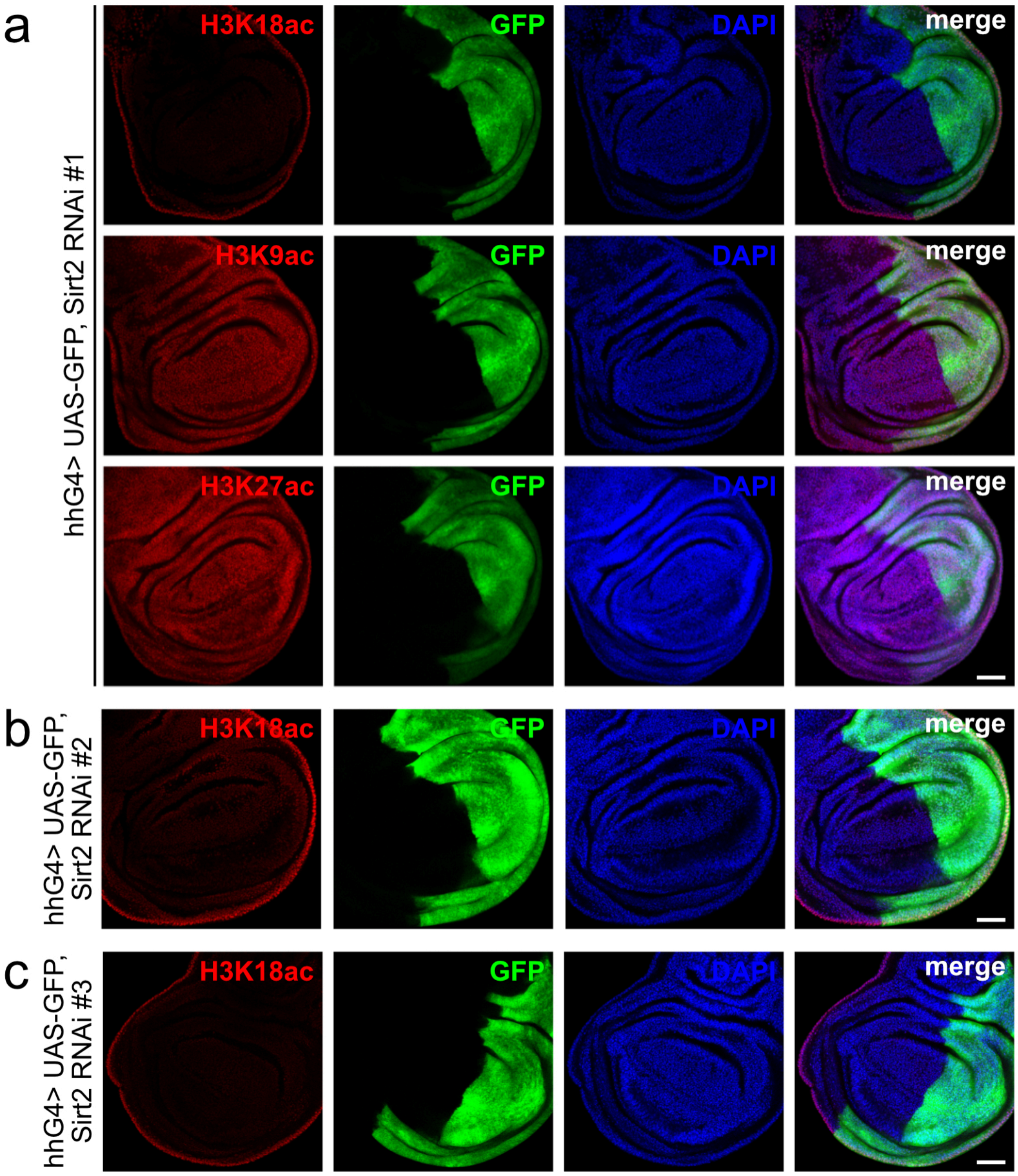

Fig. 27: Knockdown of sirtuin 2 does not affect histone acetylation

(**a**) Knockdown of sirtuin 2 (Sirt2) in the posterior compartment (GFP+, green), driven by hedgehogGAL4 (hhG4), does not affect acetylation of H3K18, H3K9, or H3K27. (**b**-**c**) The effect of Sirt2 knockdown on H3K18ac was validated with two additional independent RNAi lines, none showing an impact on H3K18ac levels. Histone acetylation levels (red) were assessed by immunostaining of the respective acetylation site in wing discs of wandering third-instar larvae. Nuclei were counterstained with DAPI (blue). Images are given in single or merged channel configurations. Scale bars: 50 µm

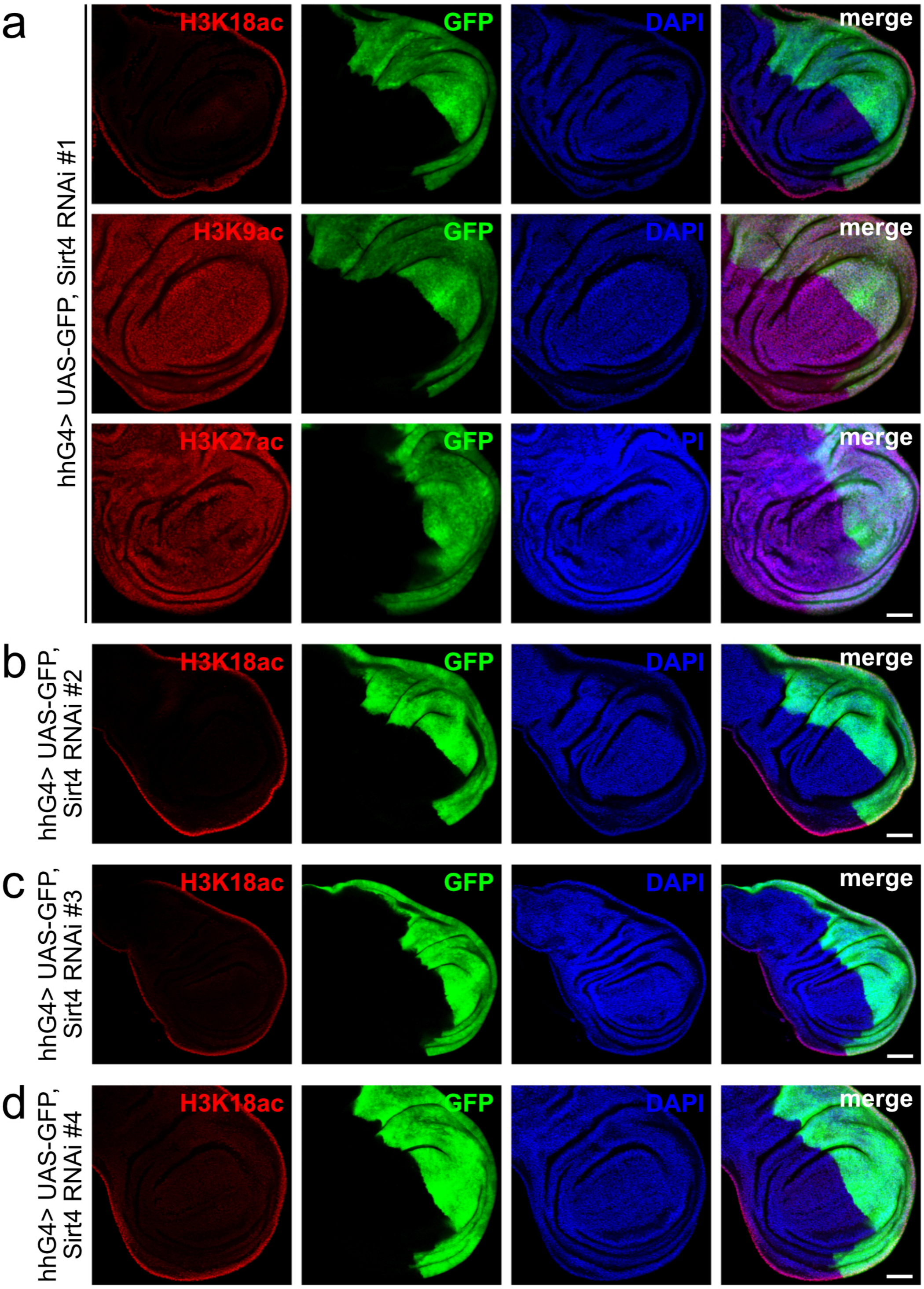

Fig. 28: Knockdown of sirtuin 4 does not affect histone acetylation

(**a**) Knockdown of sirtuin 4 (Sirt4) in the posterior compartment (GFP+, green), driven by hedgehogGAL4 (hhG4), does not affect acetylation of H3K18, H3K9, or H3K27. (**b-d**) The effect of Sirt4 knockdown on H3K18ac was validated with three additional independent RNAi lines, none showing an impact on H3K18ac levels. Histone acetylation levels (red) were assessed by immunostaining of the respective acetylation site in wing discs of wandering third-instar larvae. Nuclei were counterstained with DAPI (blue). Images are given in single or merged channel configurations. Scale bars: 50 µm

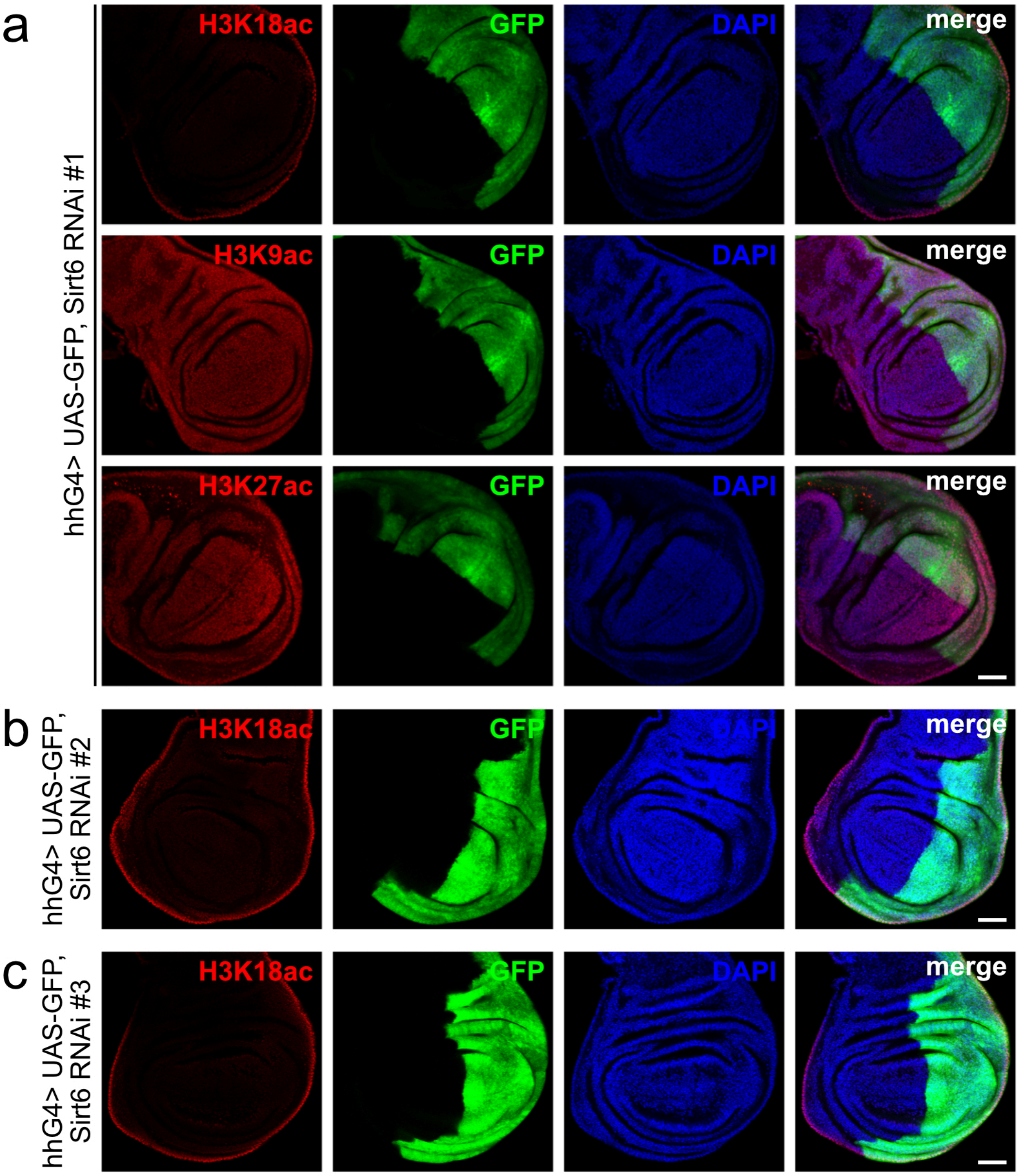

Fig. 29: Knockdown of sirtuin 6 does not affect histone acetylation
(**a**) Knockdown of sirtuin 6 (Sirt6) in the posterior compartment (GFP+, green), driven by hedgehogGAL4 (hhG4), does not affect acetylation of H3K18, H3K9, or H3K27. (**b-c**) The effect of Sirt6 knockdown on H3K18ac was validated with two additional independent RNAi lines, none showing an impact on H3K18ac levels. Histone acetylation levels (red) were assessed by immunostaining of the respective acetylation site in wing discs of wandering third-instar larvae. Nuclei were counterstained with DAPI (blue). Images are given in single or merged channel configurations. Scale bars: 50 µm

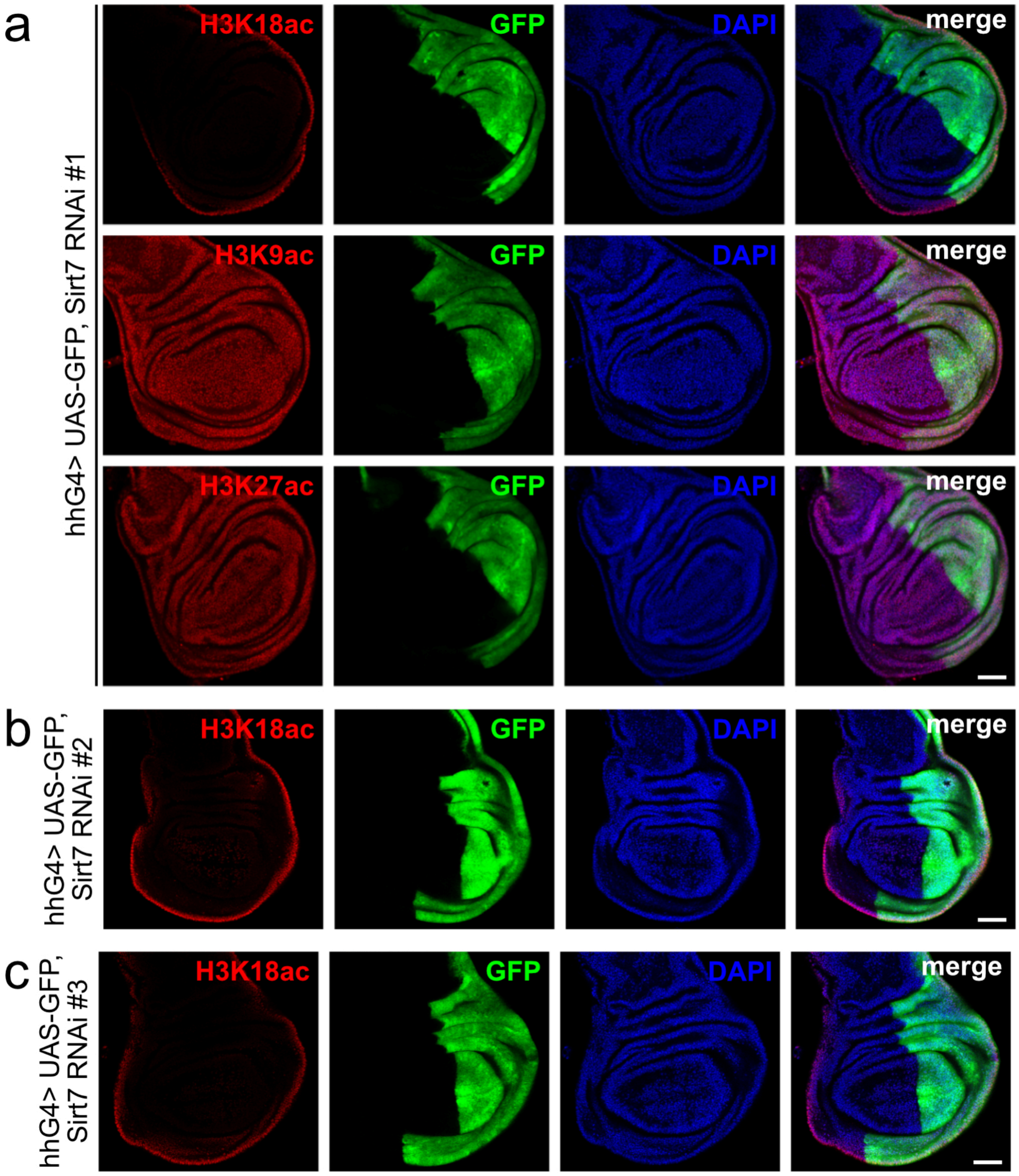

Fig. 30: Knockdown of sirtuin 7 does not affect histone acetylation
(**a**) Knockdown of sirtuin 7 (Sirt7) in the posterior compartment (GFP+, green), driven by hedgehogGAL4 (hhG4), does not affect acetylation of H3K18, H3K9, or H3K27. (**b-c**) The effect of Sirt7 knockdown on H3K18ac was validated with two additional independent RNAi lines, none showing an impact on H3K18ac levels. Histone acetylation levels (red) were assessed by immunostaining of the respective acetylation site in wing discs of wandering third-instar larvae. Nuclei were counterstained with DAPI (blue). Images are given in single or merged channel configurations. Scale bars: 50 µm

Contrary to the findings with sirtuins, pharmacological inhibition of metabolite-independent HDACs with butyrate, trichostatin A (TSA), or panobinostat (PB) prevented loss of H3K18ac in the rim of the wing disc in the presence of the nej inhibitor A485 (Fig. 31), indicating that H3K18ac is deacetylated by a class I, II, or IV HDAC. To identify the specific HDAC responsible for H3K18ac deacetylation, I knocked down all metabolite-independent HDACs individually, namely HDAC1, HDAC3, HDAC4, HDAC6, and HDAC11 (Figs. 32-37) revealing HDAC1 as the deacetylase for H3K18ac. Knockdown of HDAC1 mildly increased levels of H3K18ac and slightly those of H4K8ac in the rim of the wing disc but did not change their non-uniform pattern (Figs. 32-33). HDAC1 knockdown also increased levels of H3K9ac and H3K27ac throughout the disc and caused a reduction in posterior compartment size, marked by GFP. The extend of this effect varied, depending on the RNAi line used but suggested an essential role for HDAC1 in control of cell viability. Knockdown of HDAC3 only increased acetylation of H3K9 and H3K27, but not of H3K18, and reduced the size of the posterior wing disc, marked by GFP, with 3 out of 4 RNAi lines (Fig. 34). Reduced tissue size suggested an essential role for HDAC3 activity in control of cell viability. The effect of HDAC knockdown on the H3K18ac signal was validated with at least two independent RNAi lines for each enzyme. To exclude secondary effects of prolonged HDAC1 knockdown on H3K18ac levels, I induced temperature-sensitive RNAi expression for two days. This condition did not impact disc morphology but still caused a mild increase in H3K18ac signal specifically in the rim of the disc as seen in x-y section as well as sum projection of the wing disc (Fig. 38).

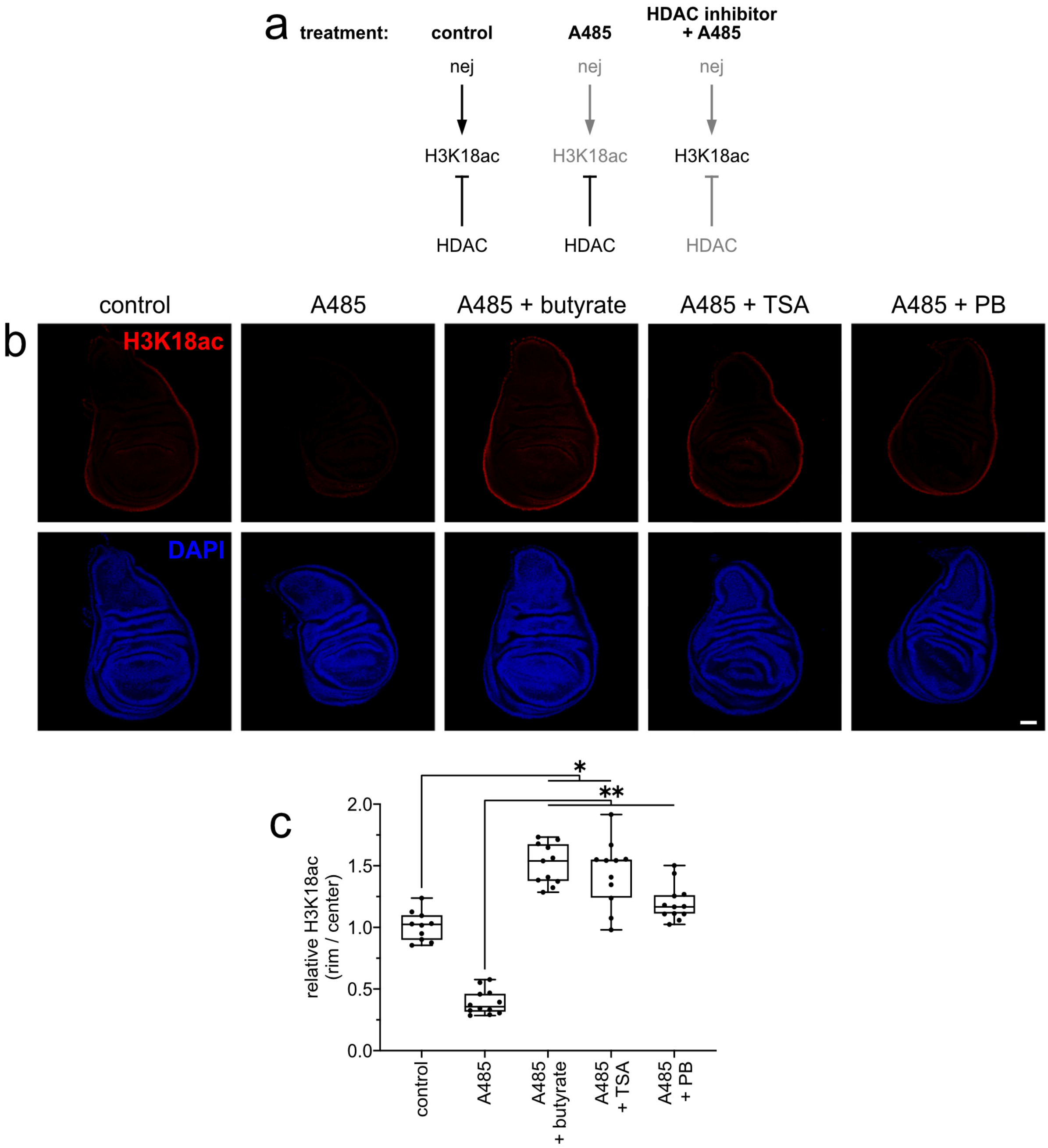

Fig. 31: H3K18ac is deacetylated by a class I, II, or IV histone deacetylase
(**a**) Experimental strategy to test the role of metabolite-independent histone deacetylases (HDAC) in the deacetylation of H3K18ac. Under control conditions, nejire (nej) acetylates H3K18, which is deacetylated at a lower rate by a deacetylase, resulting in H3K18ac. Inhibition of nej by A485 prevents new H3K18ac, resulting in loss of the histone mark due to active deacetylation. Co-treatment of discs with the nej inhibitor and a HDAC inhibitor should prevent loss of H3K18ac, if this mark is deacetylated by a class I, II, or IV histone deacetylase. (**b-c**) H3K18ac (red) is deacetylated by a class I, II, or IV histone deacetylase as their inhibition with butyrate (20 mM), trichostatin A (TSA, 500 nM), or panobinostat (PB, 100 nM) causes retention of high H3K18ac levels upon nej inhibition by A485 (20 µM). Wing discs of wandering third-instar larvae were incubated for 2 h in explant cultures with the indicated inhibitors before immunostaining of H3K18ac (red) and nuclear counterstain with DAPI. Representative images are shown in (b) and quantified in (c) with relative H3K18ac signal intensity expressed as a ratio of signal in the rim versus center of the disc. Statistical significance was determined by Kruskal-Wallis test with Dunn's multiple comparisons test (n=10-12 discs from 2 independent experiments; * <0.05, ** <0.01). Scale bar: 50 µm.

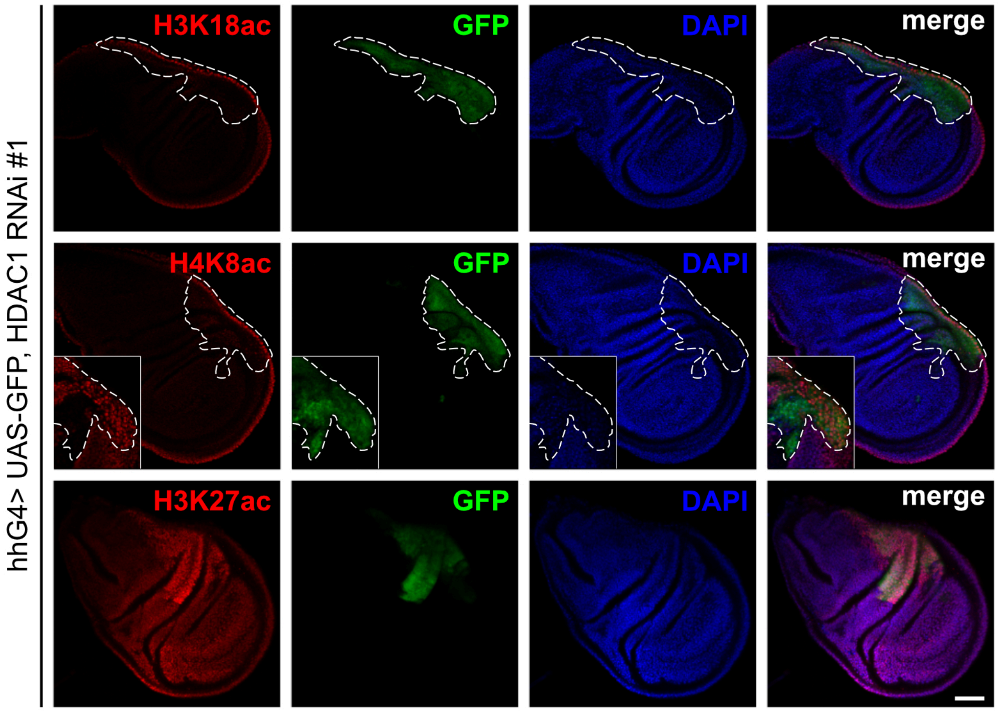

Fig. 32: Knockdown of histone deacetylase 1 increases H3K18ac, H4K8ac, and H3K27ac
Knockdown of histone deacetylase 1 (HDAC1) in the posterior compartment (GFP+, green), driven by hedgehogGAL4 (hhG4), mildly increases acetylation of H3K18 and H4K8 specifically in the rim of the disc but strongly increases H3K27ac in the entire posterior disc. Additionally, the size of the posterior wing disc is strongly reduced upon enzyme knockdown. The dashed lines mark the posterior wing disc (GFP+, green). Insets show a different x-y section from the same disc. Histone acetylation levels (red) were assessed by immunostaining of the respective acetylation site in wing discs of wandering third-instar larvae. Nuclei were counterstained with DAPI (blue). Images are given in single or merged channel configurations. Scale bar: 50 µm

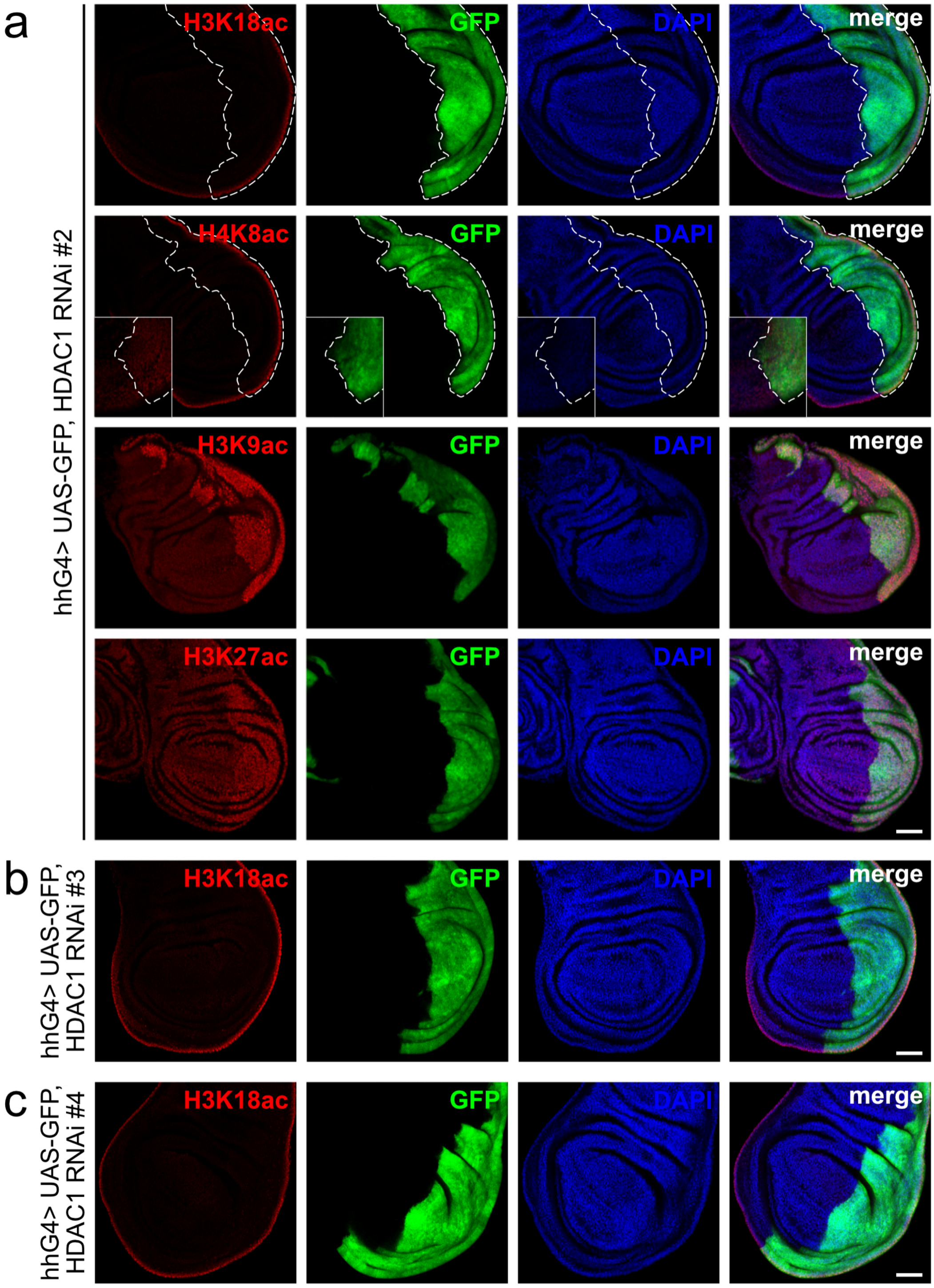

Fig. 33: Knockdown of histone deacetylase 1 increases H3K18ac, H4K8ac, H3K9ac, and H3K27ac
(**a**) Knockdown of histone deacetylase 1 (HDAC1) with a second independent RNAi line in the posterior compartment (GFP+, green), driven by hedgehogGAL4 (hhG4), mildly increases acetylation of H3K18 and H4K8 specifically in the rim of the disc but strongly increases H3K27ac and H3K9ac in the entire posterior disc. Additionally, the size of the posterior wing disc is slightly reduced upon enzyme knockdown. The dashed lines mark the posterior wing disc (GFP+, green). Insets show a different x-y section from the same disc. (**b-c**) The effect of HDAC1 knockdown on H3K18ac was validated with two additional independent RNAi lines, also showing a mild increase in H3K18ac levels in the rim of the disc. Histone acetylation levels (red) were assessed by immunostaining of the respective acetylation site in wing discs of wandering third-instar larvae. Nuclei were counterstained with DAPI (blue). Images are given in single or merged channel configurations. Scale bars: 50 µm

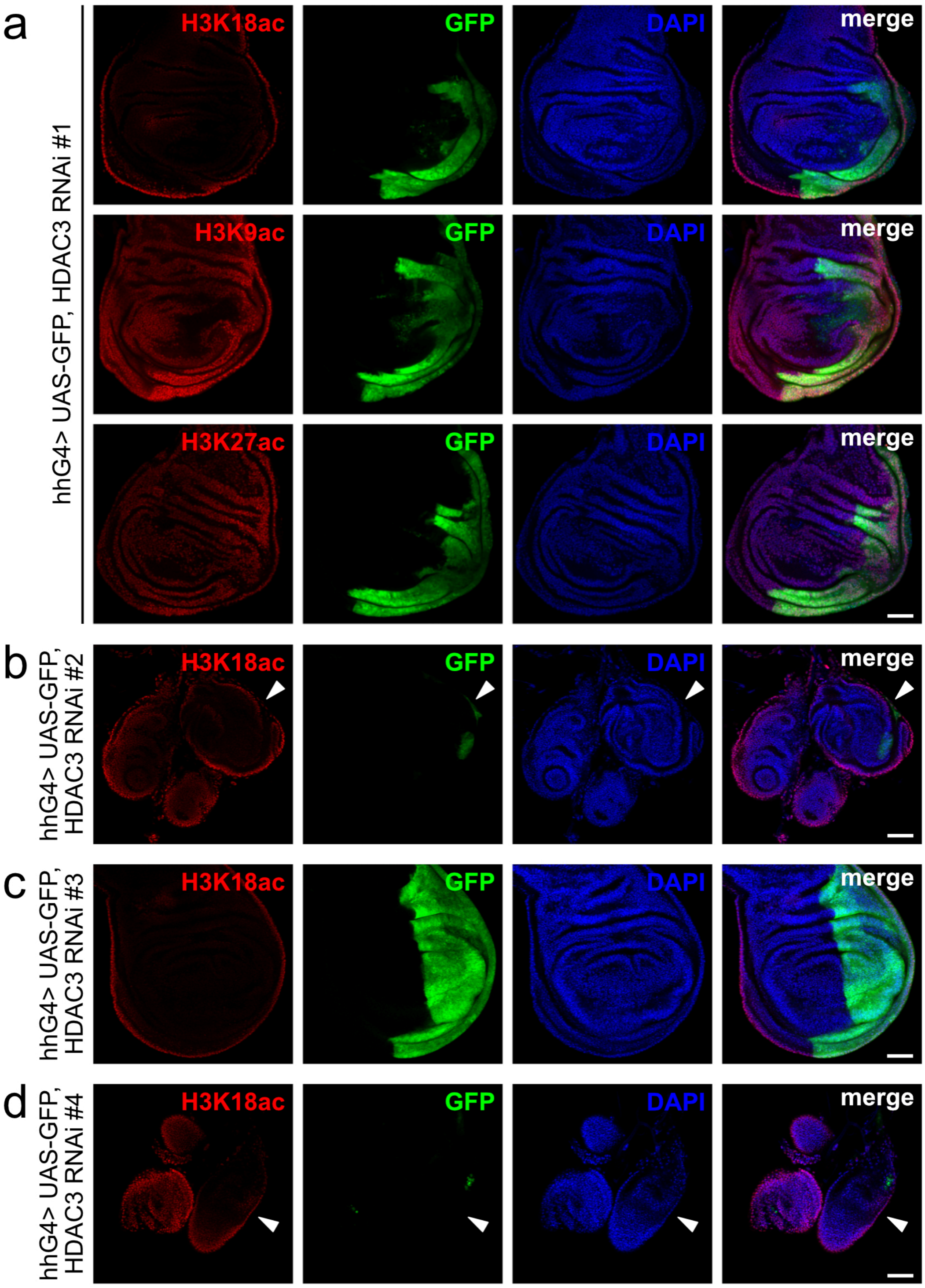

Fig. 34: Knockdown of histone deacetylase 3 increases H3K9ac but not H3K18ac
(**a**) Knockdown of histone deacetylase 3 (HDAC3) in the posterior compartment (GFP+, green), driven by hedgehogGAL4 (hhG4), increases acetylation of H3K9 and H3K27ac but does not impact H3K18ac. Additionally, the size of the posterior wing disc is reduced upon enzyme knockdown. (**b-d**) The effect of HDAC3 knockdown on H3K18ac was validated with three additional independent RNAi lines, none showing an impact on H3K18ac levels. The decrease in the posterior compartment was more pronounced with RNAi #2 and #4 compared to #1, but absent in #3. Histone acetylation levels (red) were assessed by immunostaining of the respective acetylation site in wing discs of wandering third-instar larvae. Nuclei were counterstained with DAPI (blue). Images are given in single or merged channel configurations. Scale bars: 50 µm

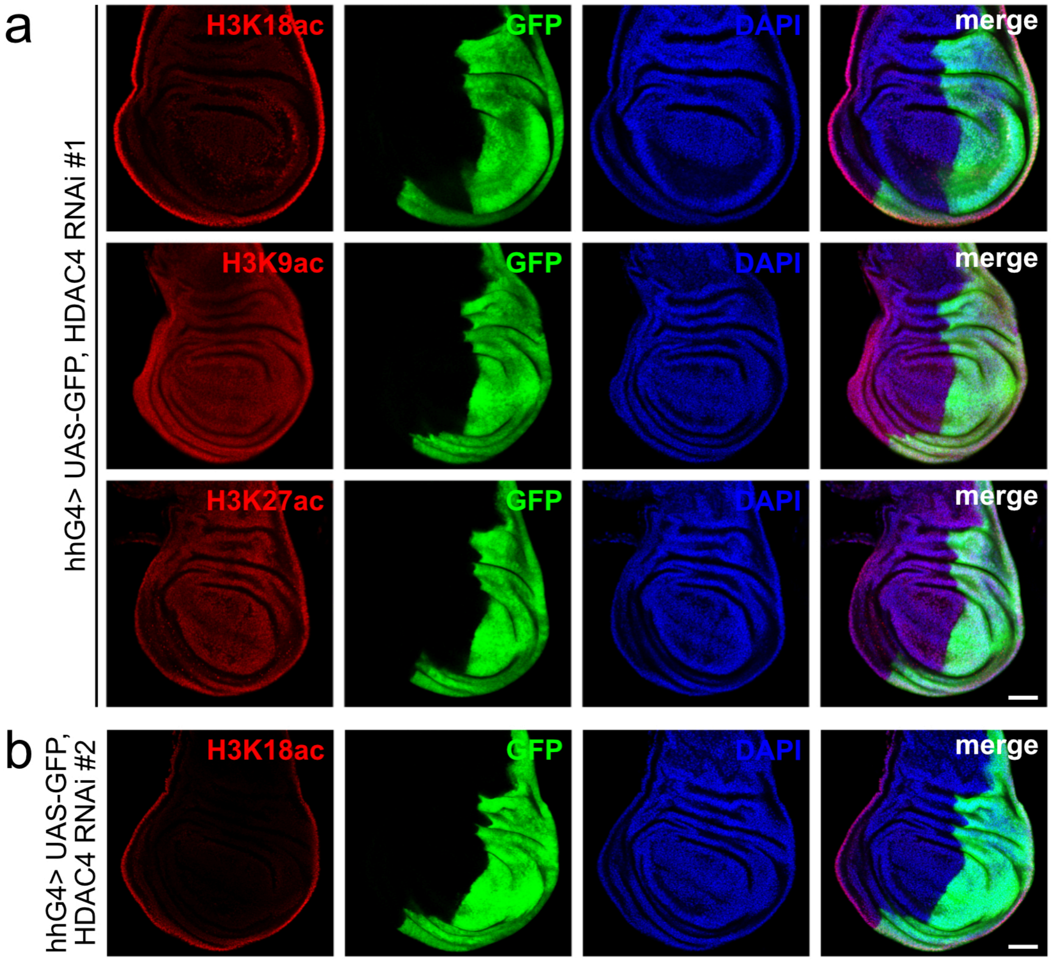

Fig. 35: Knockdown of histone deacetylase 4 does not affect histone acetylation
(**a**) Knockdown of histone deacetylase 4 (HDAC4) in the posterior compartment (GFP+, green), driven by hedgehogGAL4 (hhG4), does not affect acetylation of H3K18, H3K9, or H3K27. (**b**) The effect of HDAC4 knockdown on H3K18ac was validated with a second independent RNAi line, showing no impact on H3K18ac levels. Histone acetylation levels (red) were assessed by immunostaining of the respective acetylation site in wing discs of wandering third-instar larvae. Nuclei were counterstained with DAPI (blue). Images are given in single or merged channel configurations. Scale bars: 50 µm

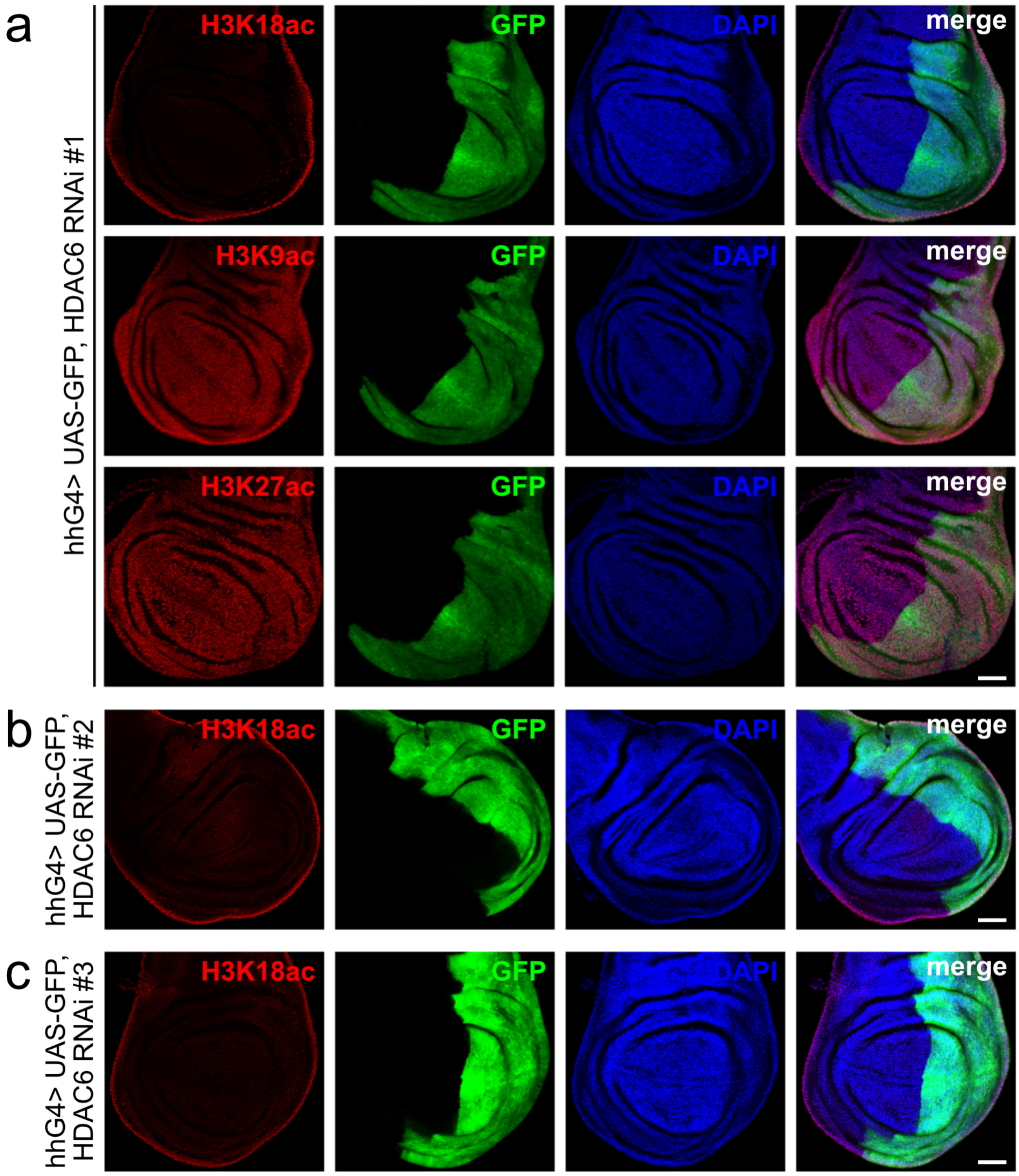

Fig. 36: Knockdown of histone deacetylase 6 does not affect histone acetylation
(**a**) Knockdown of histone deacetylase 6 (HDAC6) in the posterior compartment (GFP+, green), driven by hedgehogGAL4 (hhG4), does not affect acetylation of H3K18, H3K9, or H3K27. (**b-c**) The effect of HDAC6 knockdown on H3K18ac was validated with two additional independent RNAi lines, none showing an impact on H3K18ac levels. Histone acetylation levels (red) were assessed by immunostaining of the respective acetylation site in wing discs of wandering third-instar larvae. Nuclei were counterstained with DAPI (blue). Images are given in single or merged channel configurations. Scale bars: 50 µm

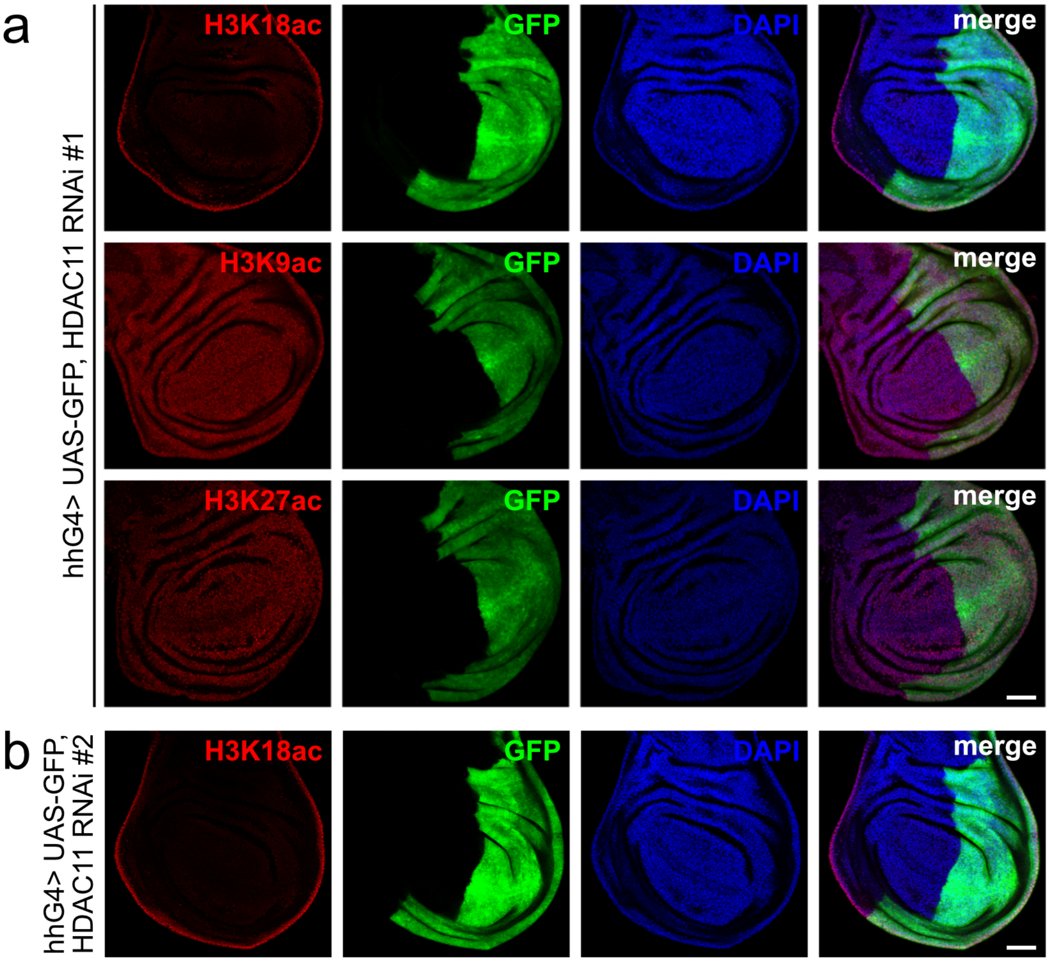

Fig. 37: Knockdown of histone deacetylase 11 does not affect histone acetylation
(**a**) Knockdown of histone deacetylase 11 (HDAC11) in the posterior compartment (GFP+, green), driven by hedgehogGAL4 (hhG4), does not affect acetylation of H3K18, H3K9, or H3K27. (**b**) The effect of HDAC11 knockdown on H3K18ac was validated with a second independent RNAi line, showing no impact on H3K18ac levels. Histone acetylation levels (red) were assessed by immunostaining of the respective acetylation site in wing discs of wandering third-instar larvae. Nuclei were counterstained with DAPI (blue). Images are given in single or merged channel configurations. Scale bars: 50 µm

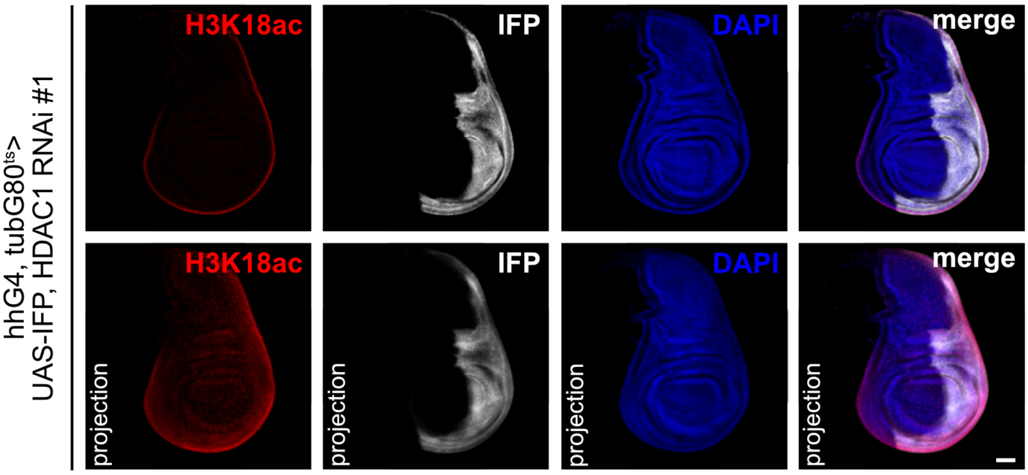

Fig. 38: Knockdown of histone deacetylase 1 increases H3K18ac
Knockdown of histone deacetylase 1 (HDAC1) in the posterior compartment (infra-red protein+, IFP+, white), driven by hedgehogGAL4 (hhG4), mildly increases acetylation of H3K18 (red) specifically in the rim of the wing disc, as shown in x-y section (upper panels) or sum projection (lower panels). Temperature-sensitive knockdown of HDAC1 was induced for 2 days at 29°C. H3K18ac levels were assessed by immunostaining in wing discs of wandering third-instar larvae. Nuclei were counterstained with DAPI (blue). Images are given in single or merged channel configurations. Scale bar: 50 µm

Increased acetylation of H3K18 upon HDAC1 knockdown verified the ability of HDAC1 to deacetylate H3K18ac but it did not exclude deacetylation by other enzymes. If HDAC1 was the main H3K18ac deacetylase, knockdown of the enzyme should prevent loss of H3K18ac upon nej inhibition (Fig. 39a), similar to the observed rescue upon pharmacological inhibition of all metabolite-independent HDACs (Fig. 31). When tested experimentally, rescue of H3K18ac levels upon A485 treatment in the posterior compartment was observed in discs expressing an HDAC1 RNAi in this tissue region, verifying HDAC1 as the main H3K18ac deacetylase (Fig. 39b).

The effect of knockdown of different acetyltransferases and deacetylases on H3K9ac, H3K18ac, H3K27ac, and H4K8ac as well as on disc morphology are summarized in table 6. The fact that knockdown of the main H3K18ac deacetylase HDAC1 caused a mild increase in H3K18ac signal but did not change its pattern, indicated that the non-uniform H3K18ac distribution was achieved by local histone acetylation by nej in the wing disc rim (Fig. 40b) rather than by local deacetylation by HDAC1 in the disc interior (Fig. 40a).

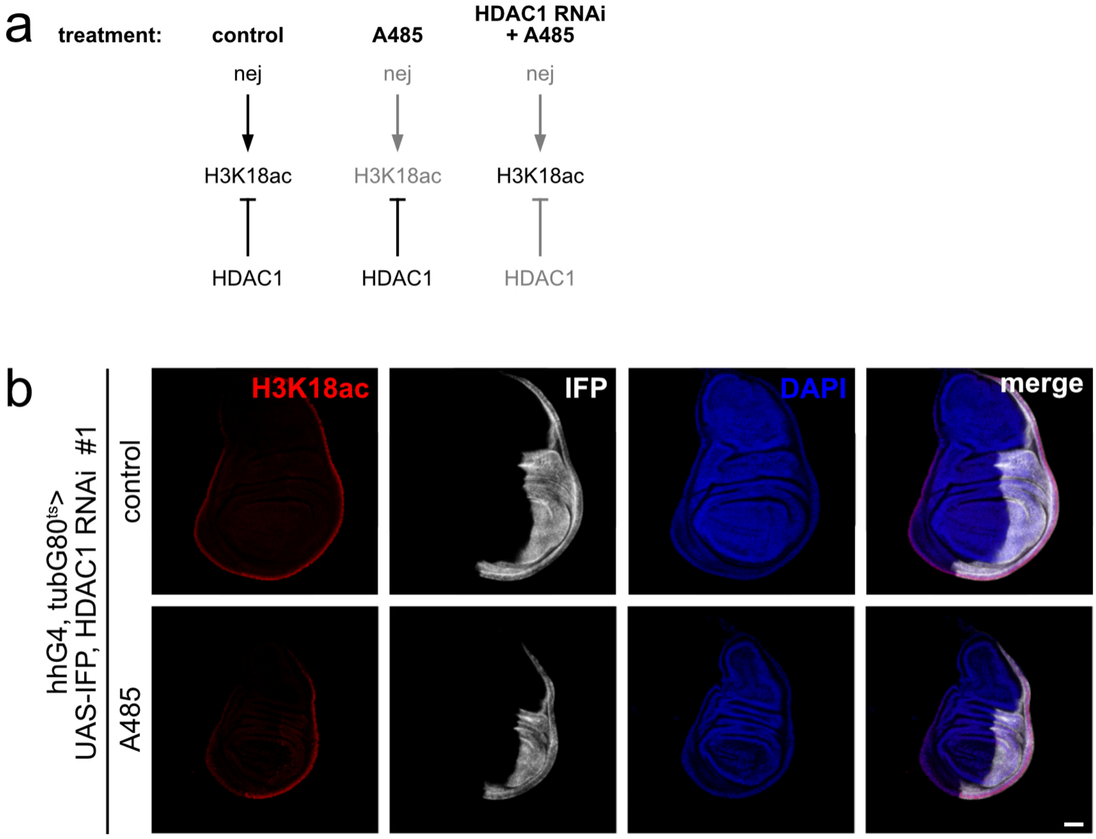

Fig. 39: Histone deacetylase 1 is the main deacetylase of H3K18ac
(**a**) Experimental strategy to test the role of histone deacetylases 1 (HDAC1) in the deacetylation of H3K18ac. Under control conditions, nej acetylates H3K18, which is deacetylated at a lower rate by a deacetylase, resulting in H3K18ac marks. Inhibition of nej by A485 prevents new H3K18ac, resulting in loss of the histone mark due to active deacetylation. Treatment of discs, which express a HDAC1 RNAi, with the nej inhibitor should prevent loss of H3K18ac, if the mark is mainly deacetylated by HDAC1 (**b**) HDAC1 is the main H3K18ac deacetylase as HDAC1 knockdown, driven by hedgehogGAL4 (hhG4), prevents loss of H3K18ac (red) upon nej inhibition by A485 (20 µM) in the posterior compartment (infra-red protein+, IFP+, white; lower panels). As negative control, a disc with HDAC1 knockdown in the absence of A485 is shown (upper panel). Temperature-sensitive knockdown of HDAC1 was induced for 2 days at 29°C. Wing discs of wandering third-instar larvae were incubated for 1 h in explant cultures in the presence or absence of A485 before immunostaining of H3K18ac and nuclear counterstain with DAPI (blue). Images are given in single or merged channel configurations. Scale bar: 50 µm

Tab. 6: Effect of histone acetyltransferase and deacetylase knockdowns on histone acetylation and wing disc morphology

This table summarizes the effect of knockdown of the given histone acetyltransferases and deacetylases on H3K18ac, H4K8ac, H3K9ac, and H3K27ac levels as well as wing disc morphology (primary data shown in Figs. 20-22, 26-30, and 32-37). For all lines, RNAi as well as GFP expression were driven by hedgehogGAL4 (hhG4). Bloomington (B) and VDRC (KK) stock numbers of lines as well as the numbering (#) used in this PhD project are stated.

gene	RNAi line	#	H3K18ac	H4K8ac	H3K9ac	H3K27ac	morphology
nej	KK102885	1	🟦	🟦	🟨	🟦	🟦
Gcn5	KK108943	1	🟨	▨	🟦	🔷	🔷
Elp3	KK106128	1	🟨	▨	🟨	▨	🟨
Sirt1	KK105502	1	🟨	▨	🟨	🟨	🟨
Sirt1	B53697	2	🟨	▨	▨	▨	🟦
Sirt1	B31636	3	🟨	▨	▨	▨	🟨
Sirt1	B32481	4	🟨	▨	▨	▨	🟨
Sirt1	KK108241	5	🟨	▨	▨	▨	🟨
Sirt2	KK103790	1	🟨	▨	🟨	🟨	🟨
Sirt2	B36868	2	🟨	▨	▨	▨	🟨
Sirt2	B31613	3	🟨	▨	▨	▨	🟨
Sirt4	KK110639	1	🟨	▨	🟨	🟨	🟨
Sirt4	B31638	2	🟨	▨	▨	▨	🟨
Sirt4	B36588	3	🟨	▨	▨	▨	🟨
Sirt4	B33984	4	🟨	▨	▨	▨	🟨
Sirt6	B34530	1	🟨	▨	🟨	🟨	🟨
Sirt6	B31399	2	🟨	▨	▨	▨	🟨
Sirt6	B36801	3	🟨	▨	▨	▨	🟨
Sirt7	B32483	1	🟨	▨	🟨	🟨	🟨
Sirt7	B31093	2	🟨	▨	▨	▨	🟨
Sirt7	36802	3	🟨	▨	▨	▨	🟨
HDAC1	B33725	1	🟥	🟧	▨	🟥	🟦
HDAC1	B34846	2	🟥	🟧	🟥	🟥	🔷
HDAC1	B31616	3	🟥	▨	▨	▨	🟨
HDAC1	B36800	4	🟧	▨	▨	▨	🟨
HDAC3	KK107073	1	🟨	▨	🟥	🟥	🟦
HDAC3	B64476	2	🟨	▨	▨	▨	🟦
HDAC3	B31633	3	🟨	▨	▨	▨	🟨
HDAC3	B34778	4	🟨	▨	▨	▨	🟦
HDAC4	B28549	1	🟨	▨	🟨	🟨	🟨
HDAC4	B34774	2	🟨	▨	▨	▨	🟨
HDAC6	KK108831	1	🟨	▨	🟨	🟨	🟨
HDAC6	B31053	2	🟨	▨	▨	▨	🟨
HDAC6	B34072	3	🟨	▨	▨	▨	🟨
HDAC11	KK108098	1	🟨	▨	🟨	🟨	🟨
HDAC11	B32480	2	🟨	▨	▨	▨	🟨

🟥 mild/strong increase

🟧 weak increase

🟨 no change

🔷 weak decrease

🟦 mild/strong decrease

▨ not tested

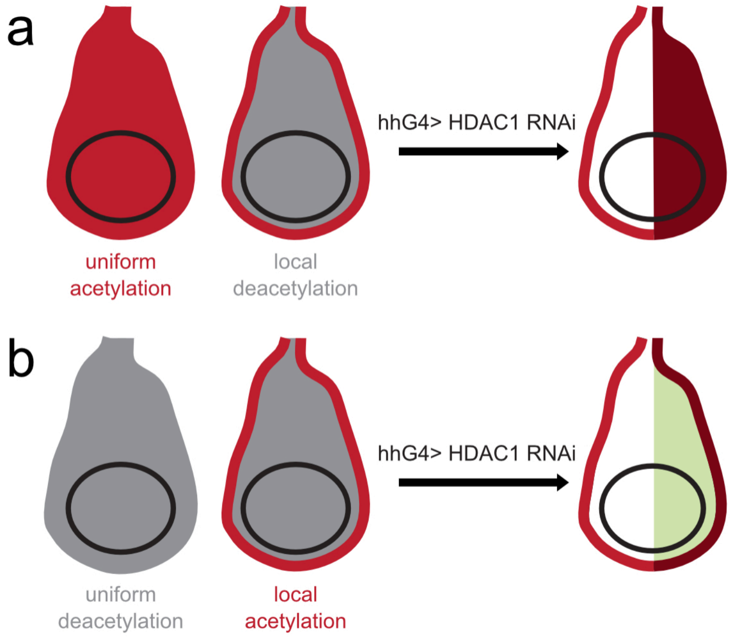

Fig. 40: Potential mechanisms to establish a non-uniform H3K18ac pattern in the wing disc
High H3K18ac (red) in the rim of the wing disc may be achieved (**a**) by uniform acetylation and local deacetylation in the tissue interior or (**b**) by uniform deacetylation and local acetylation in the tissue rim. Depending on the mechanism, knockdown of histone deacetylase 1 (HDAC1) in the posterior compartment (green) should (a) increase H3K18ac levels in the entire compartment (dark red) and result in a uniform acetylation pattern or (b) only increase levels of the histone mark in the rim (dark red).

3.4 Non-uniform fatty acid β-oxidation provides acetyl-CoA for non-uniform histone acetylation

Local acetylation by nej as the underlying mechanism for the non-uniform histone acetylation pattern in the wing disc raised the question how nej activity may be locally regulated. Potential mechanisms may be non-uniform nej expression, spatial differences in intrinsic enzyme activity, or locally restricted availability of the metabolic substrate acetyl-CoA required for acetylation.

I excluded non-uniform expression of nej based on the uniform distribution of nej transcripts in the wing disc, as visualized by two independent fluorescence *in situ* hybridization (FISH) probes (Fig. 41a-b). I validated the specificity of both probes by nej knockdown in the posterior compartment, causing a decrease in fluorescence signals (Fig. 41c-d). To test intrinsic nej activity independently of acetyl-CoA levels, I compared the non-uniform pattern of H3K18ac with the distribution of crotonylated H3K18 (H3K18crot), another histone modification conferred by nej[86]. If nej was generally more active in the rim, a similar non-uniform pattern for H3K18crot as for H3K18ac was to be expected. However, immunostaining for H3K18crot showed a uniform distribution in the wing disc (Fig. 42a). I verified the ability of nej to crotonylate H3K18 by nej knockdown in the posterior compartment, causing a drop in this histone mark (Fig. 42b). Uniform nej-dependent H3K18crot suggested that nej was expressed and enzymatically active throughout the entire disc.

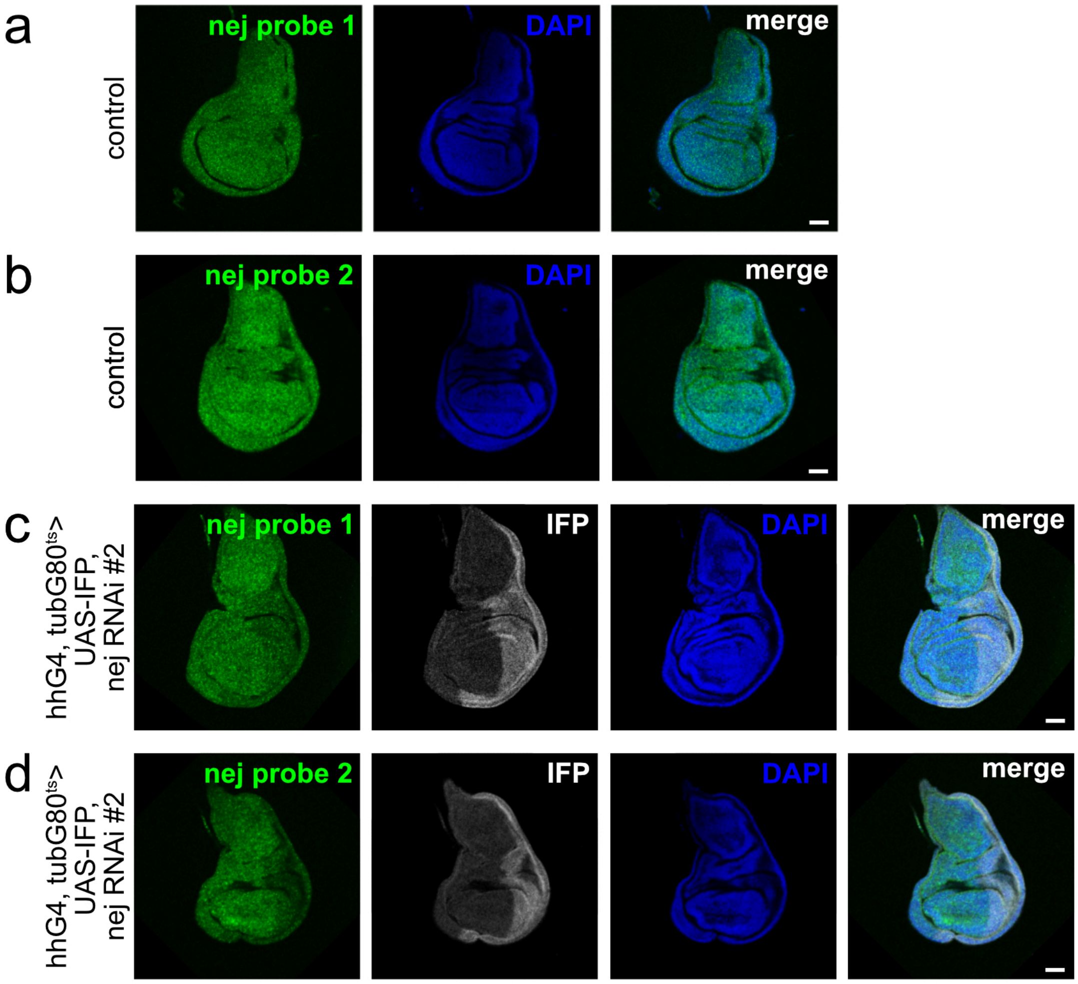

Fig. 41: Uniform transcription of nejire in the wing disc
(**a**, **b**) Fluorescence *in situ* hybridization (FISH) reveals uniform distribution of nejire (nej) transcripts (green) in the wing disc as shown for two different probes. (**c**, **d**) Specificity of both probes was validated by nej knockdown in the posterior compartment (infra-red protein+, IFP+, white), driven by hedgehogGAL4 (hhG4), causing decreased fluorescence signals. Temperature-sensitive knockdown of nej was induced for 1 day at 29°C. Nuclei were counterstained with DAPI (blue). Images are given in single or merged channel configurations. Scale bars: 50 µm

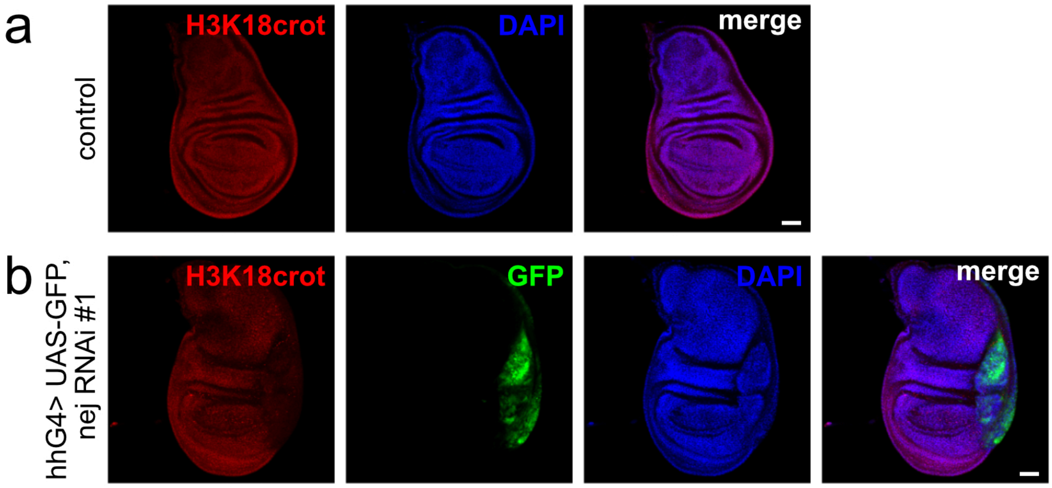

Fig. 42: Uniform, intrinsic nejire activity in the wing disc
(**a**) Crotonylation of H3K18 (H3K18crot, red), as a readout for nejire (nej) activity, is uniform in the wing disc. (**b**) Knockdown of nej in the posterior compartment (GFP+, green), driven by hedgehogGAL4 (hhG4), decreases levels of the histone mark, validating the ability of nej to generate H3K18crot. Crotonylation levels were assessed by immunostaining in wing discs of third-instar wandering larvae. Nuclei were counterstained with DAPI (blue). Images are given in single or merged channel configurations. Scale bars: 50 µm

Having excluded localized expression or a non-uniform, intrinsic activity of nej, I investigated spatially restricted availability of acetyl-CoA as the reason for high histone acetylation in the wing disc rim. Therefore, I first identified the metabolic pathway generating acetyl-CoA used for the acetylation of H3K18. Several metabolic pathways, directly or indirectly, produce this metabolic substrate, including glycolysis, glutaminolysis, and fatty acid β-oxidation. Pharmacological inhibition of glycolysis with 2-deoxyglucose (2DG) or glutaminolysis with glutaminase inhibitor 968 (968) or 6-diazo-5-oxo-L-norleucin (DON) did not affect H3K18ac levels in the wing disc (Fig. 43). To further exclude glycolysis, a major metabolic pathway in most growing tissues[1–3], as a source for acetyl-CoA for H3K18ac, I knocked down pyruvate dehydrogenase α (PDHa) and pyruvate dehydrogenase kinase (PDK), decreasing or increasing the glycolytic flux into the TCA cycle , respectively. Knockdown of both enzymes in the posterior compartment, validated by loss of immunostaining of the PDK-dependent target phospho-PDH serine 293 (pPDH S293; Fig. 44a-b), failed to impact H3K18ac levels (Fig. 44c-d). Contrary to perturbation of glycolysis or glutaminolysis, inhibition of fatty acid β-oxidation with etomoxir strongly decreased H3K18ac marks in the wing disc as compared to the control condition (Fig. 43), identifying fatty acid β-oxidation as the source of acetyl-CoA for acetylation of H3K18.

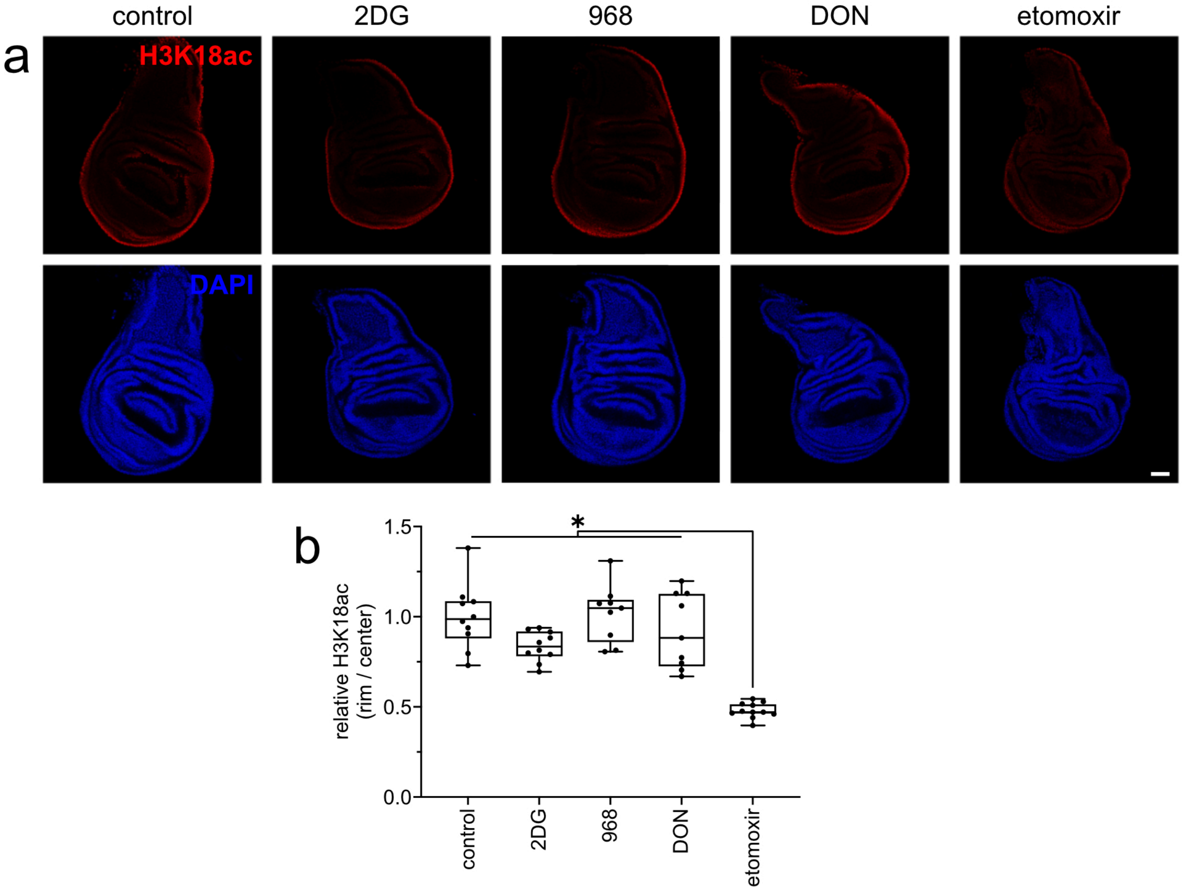

Fig. 43: H3K18ac depends on fatty acid β-oxidation
H3K18ac (red) in the rim of the wing disc is reduced upon inhibition of fatty acid β-oxidation (500 µM etomoxir) but not glycolysis (10 mM 2-deoxy-glucose, 2DG) or glutaminolysis (50 µM glutaminase inhibitor 968 (968) or 500 µM 6-diazo-5-oxo-L-norleucin (DON)). Wing discs of wandering third-instar larvae were incubated for 2 h in explant cultures with the indicated inhibitors before immunostaining of H3K18ac and nuclear counterstain with DAPI (blue). Representative images are shown in (**a**) and quantified in (**b**) with relative H3K18ac signal intensity expressed as a ratio of signal in the rim versus center of the disc. Statistical significance was determined by Kruskal-Wallis test with Dunn's multiple comparisons test (n=9-11 discs from 2 independent experiments; * <0.05). Scale bar: 50 µm

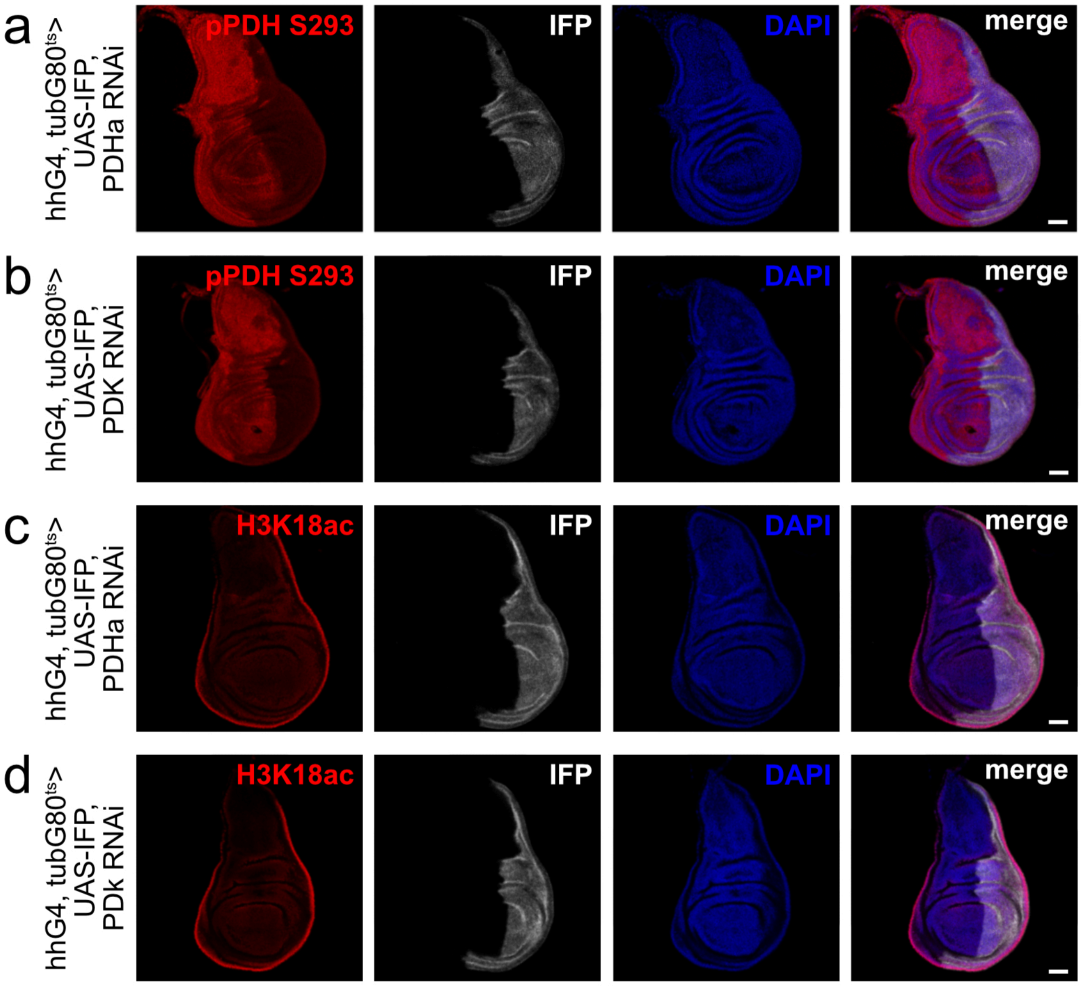

Fig. 44: H3K18ac is independent of glycolysis

Knockdown of (**a**) pyruvate dehydrogenase α (PDHa) to reduce or (**b**) pyruvate dehydrogenase kinase (PDK) to increase glycolytic acetyl-CoA production in the posterior compartment of the wing disc (infra-red protein+, IFP+, white), driven by hedgehogGAL4 (hhG4), as validated by immunostaining of PDK-dependent target phospho-PDH serine 293 (pPDH S293). Loss of neither enzyme impacts levels of H3K18ac (**c** and **d**, respectively), indicating that glucose-derived acetyl-CoA is not required for acetylation of H3K18. Temperature-sensitive knockdown of PDHa or of PDK was induced for 1 day at 29°C. Levels of pPDH S293 (a and b, red) and of H3K18ac (c and d, red) were assessed by immunostaining in wing discs of wandering third-instar larvae. Nuclei were counterstained with DAPI (blue). Images are given in single or merged channel configurations. Scale bars: 50 µm

To gain further evidence for the importance of fatty acid β-oxidation in maintaining high H3K18ac in the rim, I employed experimental strategies to rescue the loss of H3K18ac upon etomoxir treatment. Etomoxir inhibits fatty acid β-oxidation by preventing mitochondrial import of long-chain fatty acids[87–89]. In contrast, shorter fatty acids, like octanoate, freely diffuse into mitochondria and are able to fuel fatty acid β-oxidation in the presence of etomoxir. In line with this fact, supplementation of wing discs with octanoate rescued etomoxir-induced loss of H3K18ac levels (Fig. 45). Knockdown of HDAC1 in the posterior compartment also prevented etomoxir-induced decrease in H3K18ac levels (Fig. 46), in line with previous observation of HDAC1 being the main deacetylase of H3K18ac (Fig. 39).

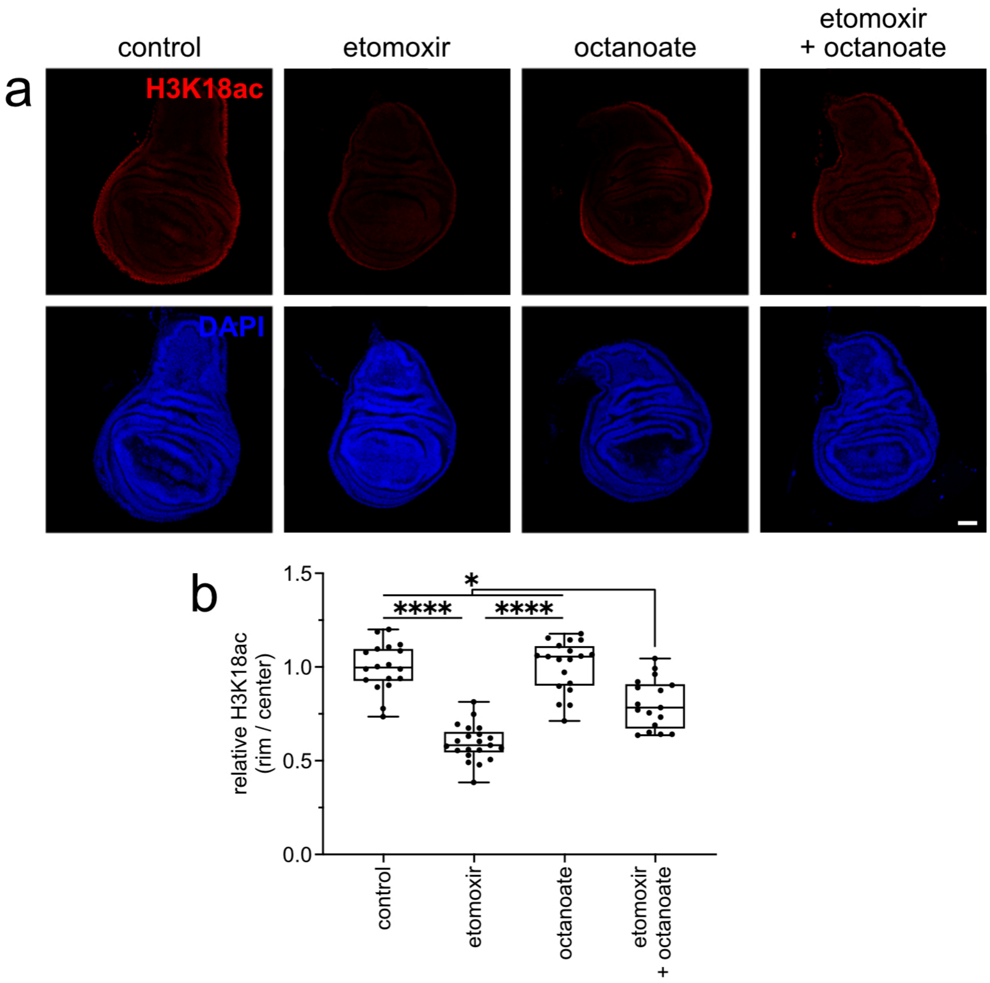

Fig. 45: Octanoate rescues H3K18ac levels upon inhibition of fatty acid β-oxidation
Etomoxir-induced (500 µM) loss of H3K18ac (red) is rescued by supplementation with short-chain fatty acid octanoate (10 mM). Octanoate alone does not impact H3K18ac levels. Wing discs of wandering third-instar larvae were incubated for 2 h in explant cultures with the indicated compounds before immunostaining of H3K18ac and nuclear counterstain with DAPI (blue). Representative images are shown in (**a**) and quantified in (**b**) with relative H3K18ac signal intensity expressed as a ratio of signal in the rim versus center of the disc. Statistical significance was determined by Kruskal-Wallis test with Dunn's multiple comparisons test (n=17-21 discs from 4 independent experiments; * <0.05, ****<0.0001). Scale bar: 50 µm

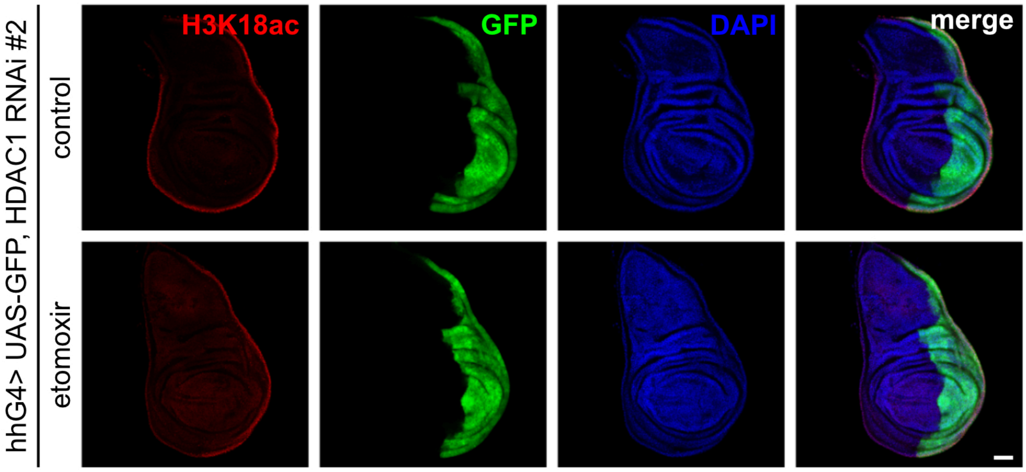

Fig. 46: Histone deacetylase 1 prevents H3K18ac decrease upon inhibition of fatty acid β-oxidation
The decrease in H3K18ac (red) caused by etomoxir treatment (500 µM) is rescued by histone deacetylase 1 (HDAC1) knockdown in the posterior compartment (GFP+, green), driven by hedgehogGAL4 (hhG4; lower panel). As negative control, a disc with HDAC1 knockdown in the absence of etomoxir is shown (upper panel). Wing discs of wandering third-instar larvae were incubated in the presence or absence of etomoxir for 2 h in explant cultures before immunostaining of H3K18ac and nuclear counterstain with DAPI (blue). Images are given in single or merged channel configurations. Scale bar: 50 µm

Interestingly, etomoxir treatment did not only cause a decrease in immunosignals for non-uniform acetylation marks H3K18ac, H4K8ac, and ac-K in the rim of the disc (Fig. 47a-c and f). It also preferentially decreased the signal of uniform H3K9ac and H3K27ac in the rim of the tissue as shown by a reduced ratio of immunosignals in rim versus center of the disc for these marks (Fig. 47 d-f). This finding further indicated that a major portion of acetyl-CoA used for histone acetylation in the rim of the wing disc is derived from fatty acid β-oxidation.

One possible explanation for the co-existence of uniform (H3K9ac and H3K27ac; Fig. 7) and non-uniform acetylation patterns (H3K18ac and H4K8ac; Fig. 7) in the wing disc in the presence of a proposed acetyl-CoA gradient may be competitive modification of lysine residues by methylation (Fig. 48). H3K9 and H3K27 are known to be heavily methylated, whereas H3K18 and H4K8 are not[13,78]. Hence, availability of H3K9 and H3K27 for acetylation may be mainly determined by their methylation status. Indeed, uniform H3K9ac and H3K27ac levels are relatively low in the wing disc, since they do not contribute much to the non-uniform total acetylated-lysine signal (Fig. 7). In contrast, acetylation levels of H3K18 and H4K8 may directly correlate with local acetyl-CoA concentrations.

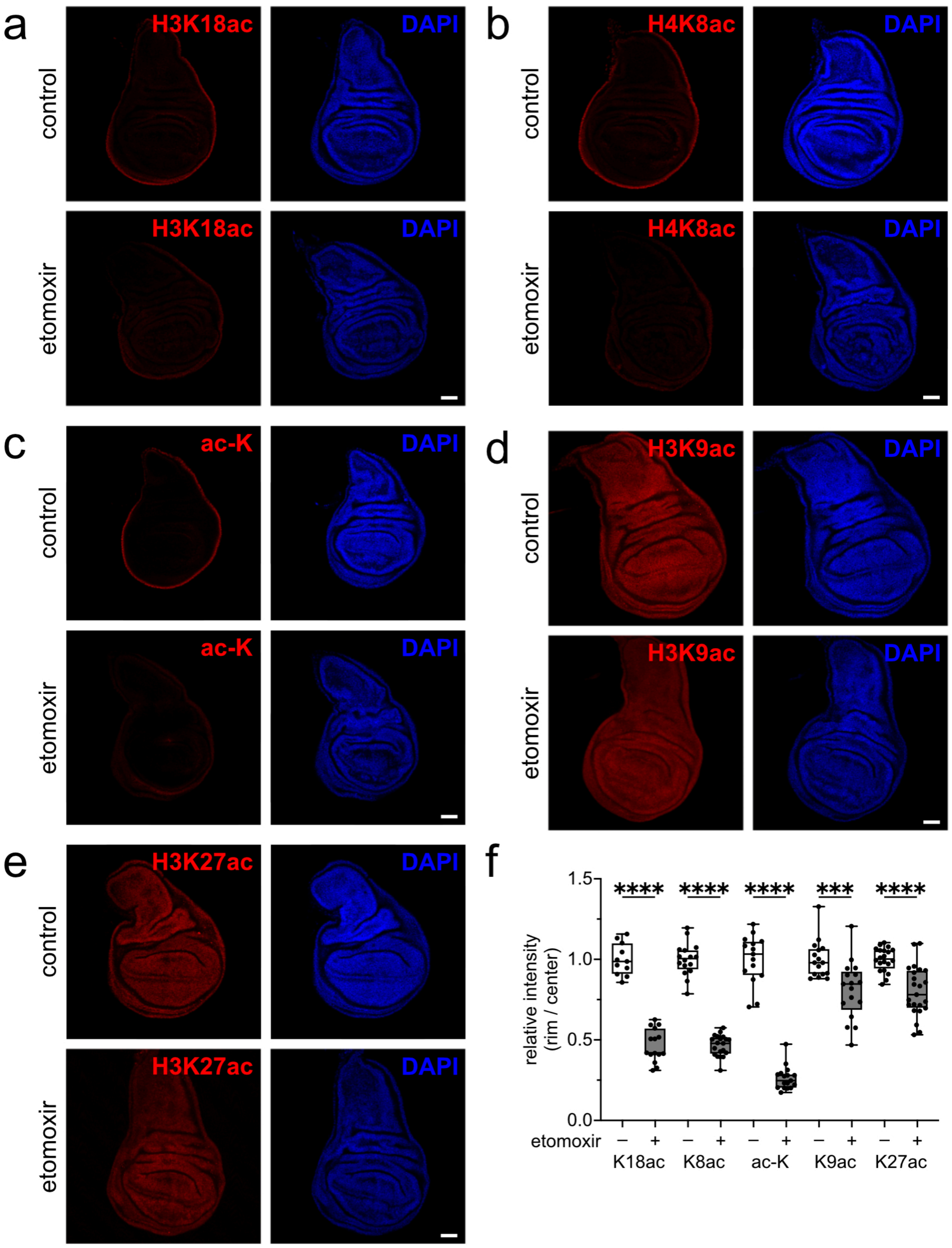

Fig. 47: Inhibition of fatty acid β-oxidation preferentially decreases acetylation in the rim of the wing disc

(**a**-**e**) Etomoxir treatment (500 µM) decreases levels of acetylation in the rim of the disc as shown by immunostaining for (a) H3K18ac, (b) H4K8ac, (c) total acetylated lysine (ac-K), (d) H3K9ac, and (e) H3K27ac. Wing discs of wandering third-instar larvae were incubated in the presence or absence of etomoxir for 2 h in explant cultures before immunostaining of the indicated acetylation marks (red) and nuclear counterstain with DAPI (blue). Representative images are shown in (a-e) and quantified in (**f**) with relative signal intensities expressed as a ratio of signal in the rim versus center of the disc. Statistical significance was determined by Kruskal-Wallis test with Dunn's multiple comparisons test (n=11-23 discs from 3-4 independent experiments; ***<0.001, ****<0.0001). Scale bars: 50 µm

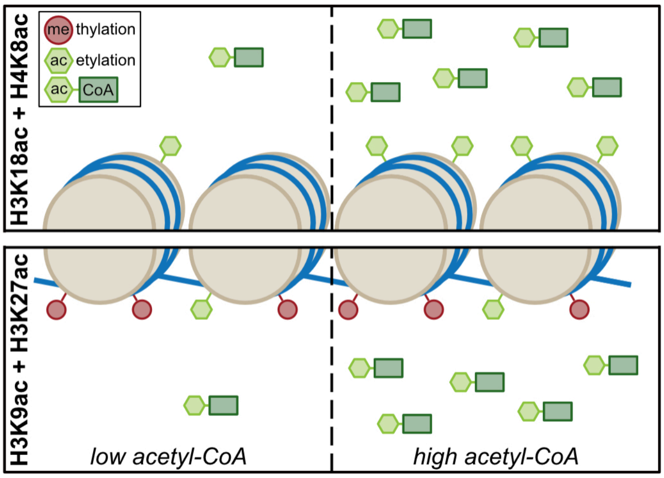

Fig. 48: Model of competitive histone modifications
The schematic describes a proposed mechanism for the distinct effects of acetyl-CoA levels on different histone acetylation marks. For non-methylated H3K18 and H4K8, acetyl-CoA concentrations directly correlate with acetylation levels. For methylated H3K9 and H3K27, acetylation depends on the availability of free lysine residues, and hence, their methylation status whereas acetyl-coA levels have little effect on acetylation stoichiometry.

Having identified fatty acid β-oxidation as the source of acetyl-CoA for non-uniform histone acetylation, I queried the non-uniform distribution of fatty acid β-oxidation in the wing disc. For this purpose, I used the mitochondrial membrane potential as a metabolic read-out as visualized by tetramethylrhodamine-methylester (TMRM) staining. TMRM specifically accumulates in mitochondria with high membrane potential. To counterstain mitochondria, TMRM stainings were performed on discs, ubiquitously expressing mitochondrially-localized GFP (mitoGFP). TMRM staining of wing discs showed high mitochondrial membrane potential in the rim of the tissue (Fig. 49), recapitulating the pattern seen for H3K18ac earlier (Fig. 7). The TMRM signal was lost upon mitochondrial depolarization by carbonyl cyanide-p-trifluoromethoxyphenylhydrazone (FCCP) treatment, validating the specificity of the staining (Fig. 49). The mitochondrial membrane potential is mainly driven by the TCA cycle, which is fueled by different metabolic pathways, including glycolysis, glutaminolysis, and fatty acid β-oxidation. Inhibition of glycolysis with 2DG or glutaminolysis with 968 or DON did not affect the mitochondrial membrane potential as shown by TMRM staining (Fig. 50). Similar to inhibition of glycolysis with 2DG, altering the glycolytic flux by PDHa or PDK knockdown in the posterior compartment of the disc did not impair mitochondrial membrane potential (Fig. 51). In contrast, inhibition of fatty acid β-oxidation by etomoxir caused loss of the TMRM signal in the rim (Fig. 50), identifying the mitochondrial membrane potential as a read-out of non-uniform fatty acid β-oxidation in the wing disc. Lipid droplets are intracellular stores for fatty acids used as metabolic fuel for fatty acid β-oxidation. Interestingly, lipid droplets, visualized by BODIPY staining, were enriched in the wing disc pouch but displayed low levels in the rim (Fig. 52), anti-correlating with the mitochondrial membrane potential (i.e., fatty acid β-oxidation). This finding further supported the idea that catabolic breakdown of lipids by fatty acid β-oxidation predominates in cells in the wing disc rim.

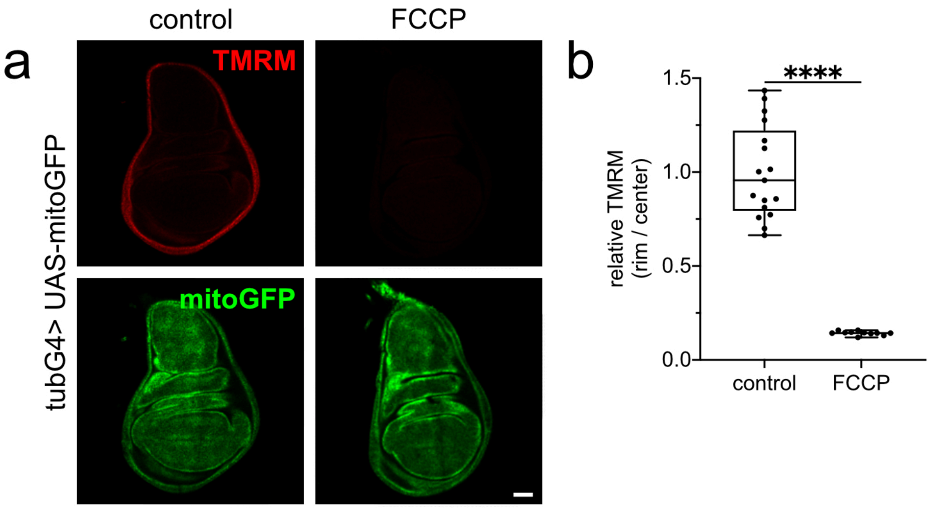

Fig. 49: Non-uniform mitochondrial membrane potential in the wing disc
High mitochondrial membrane potential, as visualized by mitochondrial accumulation of tetramethylrhodamine-methylester (TMRM, red), is specific to the rim of the wing disc. Loss of the membrane potential upon treatment with mobile ion carrier carbonyl cyanide-p-trifluoromethoxyphenylhydrazone (FCCP, 10 µM) validated specificity of TMRM in visualizing the mitochondrial membrane potential in the disc. Mitochondria are visualized by ubiquitous tubulinGAL4 (tubG4)-driven expression of mitochondrially-localized GFP (mitoGFP, green). Wing discs of wandering third-instar larvae were incubated for 30 min in explant cultures with TMRM in the presence or absence of FCCP. Representative images are shown in (**a**) and quantified in (**b**) with TMRM signal intensity expressed as a ratio of signal in the rim versus center of the disc. Statistical significance was determined by Mann-Whitney test (n=11-17 discs from 2 independent experiments; ****<0.0001). Scale bar: 50 µm

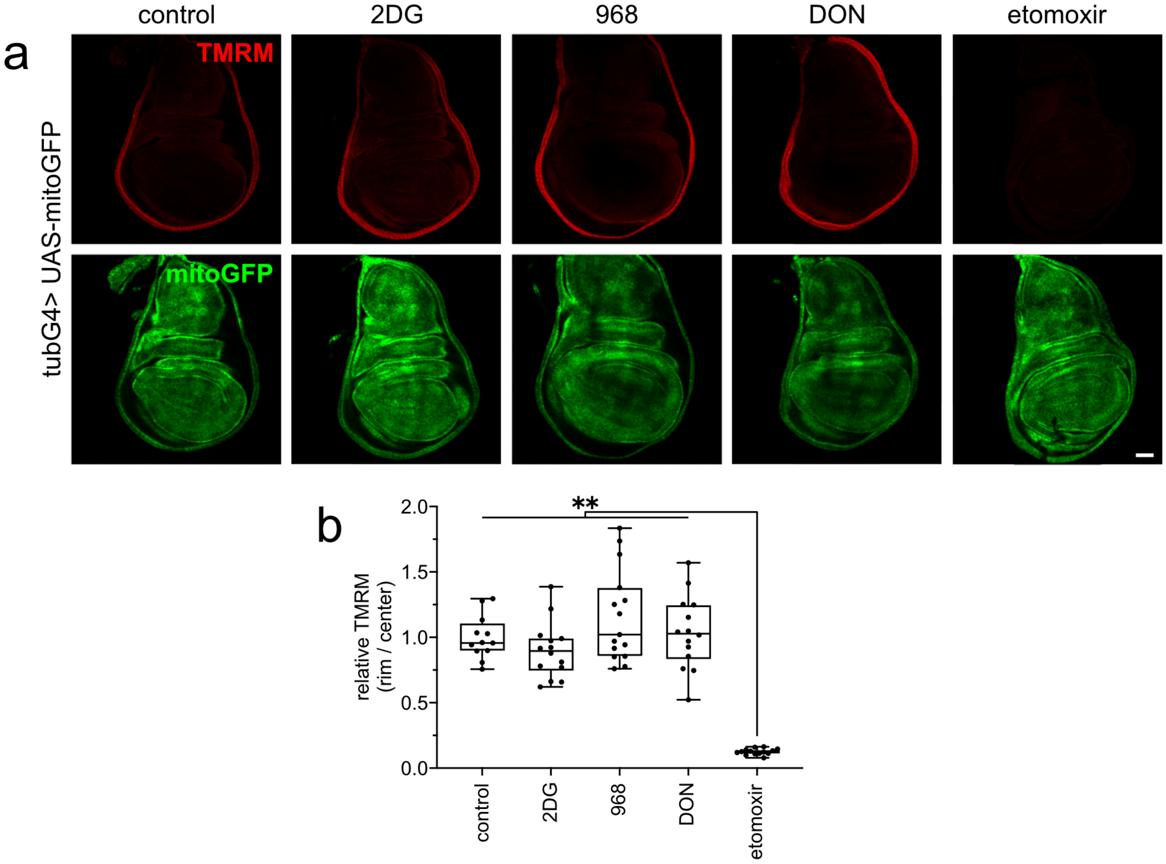

Fig. 50: Mitochondrial membrane potential depends on fatty acid β-oxidation

High mitochondrial membrane potential in the rim of the disc, as visualized by mitochondrial accumulation of tetramethylrhodamine-methylester (TMRM, red), decreases upon inhibition of fatty acid β-oxidation (500 µM etomoxir) but not of glycolysis (10 mM 2-deoxy-glucose, 2DG) or glutaminolysis (50 µM glutaminase inhibitor 968 (968) or 500 µM 6-diazo-5-oxo-L-norleucin (DON)). Mitochondria are visualized by ubiquitous tubulinG4 (tubG4)-driven expression of mitochondrially-localized GFP (mitoGFP, green). Wing discs of wandering third-instar larvae were incubated for 1 h in explant cultures with TMRM and the indicated inhibitors. Representative images are shown in (**a**) and quantified in (**b**) with TMRM signal intensity expressed as a ratio of signal in the rim versus center of the disc. Statistical significance was determined by Mann-Whitney test (n=12-15 discs from 2 independent experiments; **<0.01). Scale bar: 50 µm

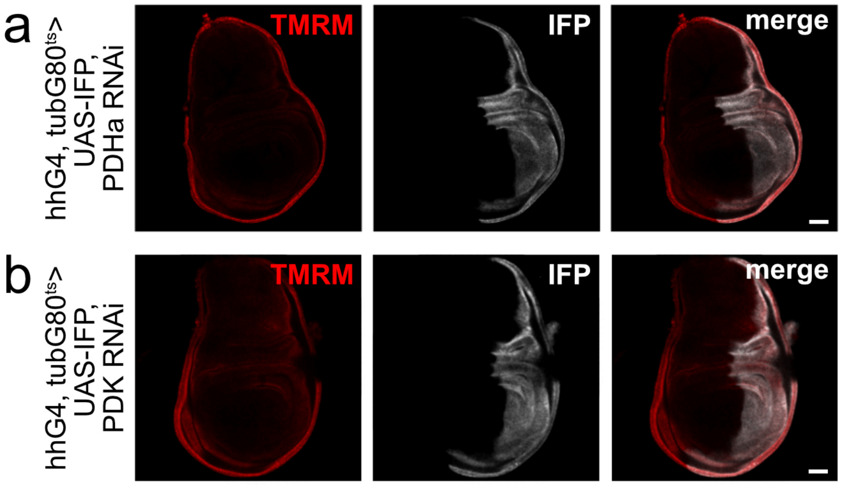

Fig. 51: Mitochondrial membrane potential is independent of glycolysis
Knockdown of (**a**) pyruvate dehydrogenase α (PDHa) to reduce or (**b**) pyruvate dehydrogenase kinase (PDK) to increase glycolytic acetyl-CoA production in the posterior compartment of the wing disc (infra-red protein+, IFP+, white), driven by hedgehogGAL4 (hhG4), does not impact tetramethylrhodamine-methylester (TMRM) staining (red), dismissing a role for glycolysis in the high mitochondrial membrane potential in the rim of the wing disc. Temperature-sensitive knockdown of PDHa and of PDK was induced for 1 day at 29°C. Wing discs of wandering third-instar larvae were incubated for 30 min in explant cultures with TMRM. Images are given in single or merged channel configurations. Scale bars: 50 µm

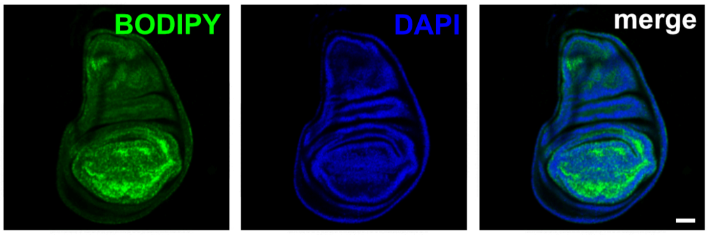

Fig. 52: Non-uniform distribution of lipid droplets in the wing disc
BODIPY staining (green) shows enrichment of lipid droplets in the pouch of the wing disc, anti-correlating with high fatty acid β-oxidation in the rim of the disc. Nuclei were counterstained with DAPI (blue). Images are given in single or merged channel configurations. Scale bar: 50 µm

To verify the non-uniform distribution of the mitochondria membrane potential in the wing disc with an independent approach, I ubiquitously expressed the mitochondrially-localized pH-sensor SypHer3s-dmito in the wing disc. As the mitochondrial membrane potential is generated through a proton gradient, high membrane potential causes an increase in mitochondrial pH. Ratiometric images of sensor-expressing discs (see Material and Methods section 2.2 for details) phenocopied the high membrane potential in the rim of the disc (Fig. 53) observed by TMRM staining before (Fig. 49). Loss of the mitochondrial membrane potential upon treatment with FCCP validated the specificity of the sensor SypHer3s-dmito (Fig. 53a). Similar to TMRM staining, inhibition of glycolysis with 2DG or glutaminolysis with 968 or DON did not affect the mitochondrial pH whereas inhibition of fatty acid β-oxidation with etomoxir caused its drop (Fig. 53b), substantiating the dependency of the mitochondrial membrane potential on the latter metabolic pathway.

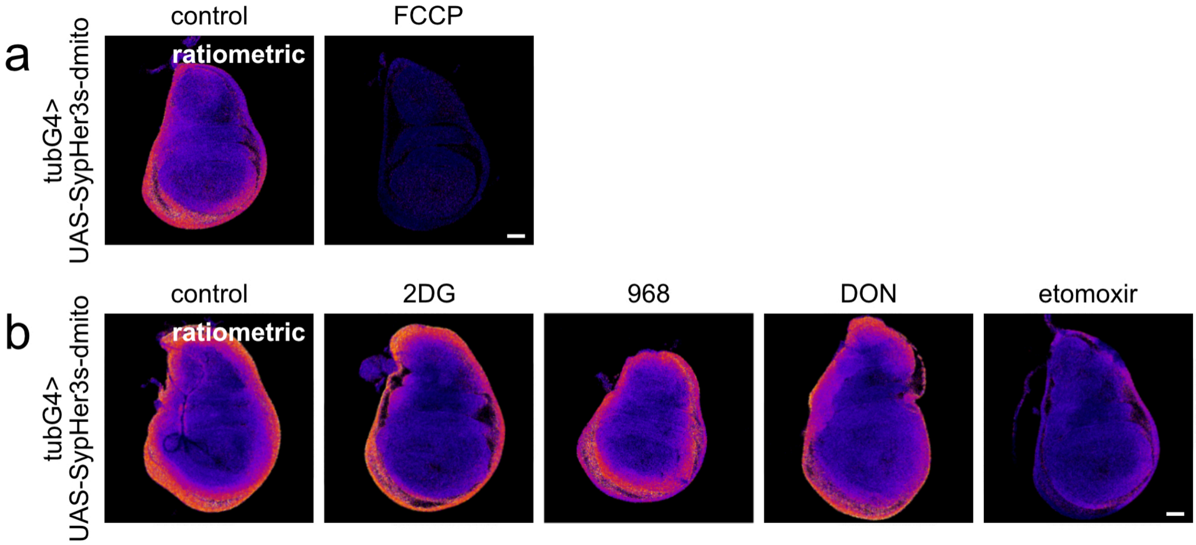

Fig. 53: Genetically-encoded, mitochondrially-localized pH-sensor validates non-uniform and fatty acid β-oxidation-dependent mitochondrial membrane potential

(**a**) Ubiquitous tubulinGAL4 (tubG4)-driven expression of a genetically-encoded, mitochondrially-localized pH-sensor (SypHer3s-dmito) shows elevated mitochondrial membrane potential (yellow to white) in the rim of the wing disc. Details on ratiometric imaging are given in the method section (2.2). Specificity of the sensor was validated by loss of the membrane potential upon treatment with mobile ion carrier carbonyl cyanide-p-trifluoromethoxyphenylhydrazone (FCCP, 10 µM). (**b**) Inhibition of fatty acid β-oxidation (500 µM etomoxir) but not of glycolysis (10 mM 2-deoxy-glucose, 2DG) or glutaminolysis (50 µM glutaminase inhibitor 968 (968) or 500 µM 6-diazo-5-oxo-L-norleucin (DON)) caused a drop in the high mitochondrial membrane potential in the rim of the disc, validating the importance of fatty acid β-oxidation in maintaining the membrane potential. Wing discs of wandering third-instar larvae were incubated for 1 h in explant cultures with the indicated inhibitors. Scale bars: 50 µm

To further investigate the causal relationship between fatty acid β-oxidation and non-uniform histone acetylation, I tested if H3K18ac was just downstream of fatty acid β-oxidation-derived acetyl-CoA or may also have an instructive role in regulating fatty acid β-oxidation via epigenetic control of gene expression as these biological processes are often interconnected. Therefore, I knocked down nej in the posterior compartment of the wing disc using two independent RNAi lines, causing loss of H3K18ac as shown before (Fig. 23). Loss of nej activity did not impact the mitochondrial membrane potential as evidenced by TMRM staining (Fig. 54), arguing against a role for histone acetylation in regulating fatty acid β-oxidation.

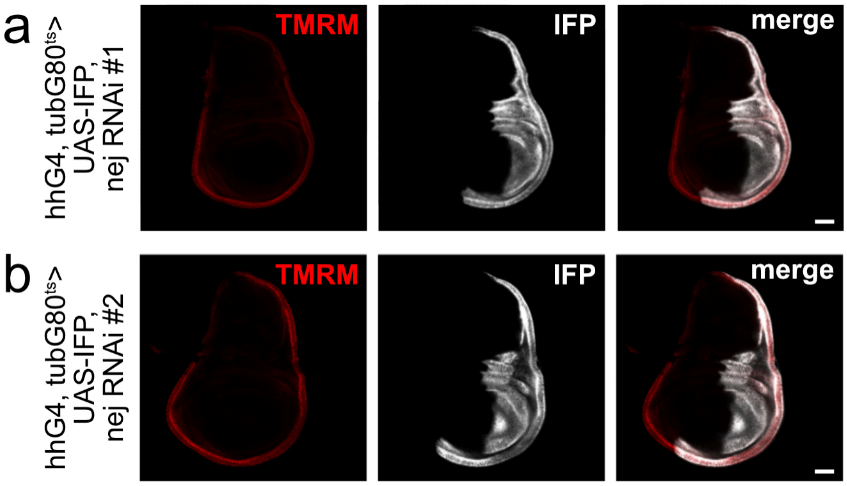

Fig. 54: Histone acetylation is not upstream of fatty acid β-oxidation
Nejire (nej)-dependent histone acetylation is not upstream of fatty acid β-oxidation because nej knockdown in the posterior compartment (infra-red protein+, IFP+, white), driven by hedgehogGAL4 (hhG4), does not impact mitochondrial membrane potential, visualized by tetramethylrhodamine-methylester (TMRM) staining (red). This effect is seen with two independent RNAi lines (**a**, **b**). Temperature-sensitive knockdown of nej was induced for 1 day at 29°C. Wing discs of wandering third-instar larvae were incubated for 30 min in explant cultures with TMRM. Images are given in single or merged channel configurations. Scale bars: 50 µm

Next, I assessed if non-uniform fatty acid β-oxidation was the determining factor defining local patterns of high versus low acetylation in the wing disc. Local regulation may be achieved by enrichment of mitochondria in the outward-facing tissue regions, facilitating spatially restricted production of acetyl-CoA and driving histone acetylation specifically in the wing disc rim. However, ubiquitous tubulinGAL4 (tubG4)-driven expression of mitoGFP showed a uniform distribution of mitochondria within the wing disc tissue (Fig. 55). I also tested whether a non-uniform distribution of mitochondria within a cell may regulate the H3K18ac pattern, with cells with high H3K18ac having outward-facing mitochondria with high membrane potential while cells with low H3K18ac levels having inward-facing mitochondria with lower membrane potential. However, heat shock-induced clones in the wing disc (see Material and Methods section 2.7 for details) with differing levels of H3K18ac showed both apical (Fig. 56, solid arrowheads) and basal mitochondria (Fig. 56, open arrowheads) as visualized by mitoGFP expression. Also, cross-sections of TMRM-stained wing discs showed a rim of high mitochondrial membrane potential that was much broader than that of high H3K18ac (Fig. 57a). Similar to H3K18ac (Fig. 13), high TMRM signal is also present in the peripodial membrane (Fig. 57b, arrowheads). Collectively, these data argued that even though fatty acid β-oxidation was non-uniform in the wing disc and provided acetyl-CoA required for histone acetylation in the rim of the disc, it was likely not the determining factor for the non-uniform histone acetylation pattern seen in this tissue.

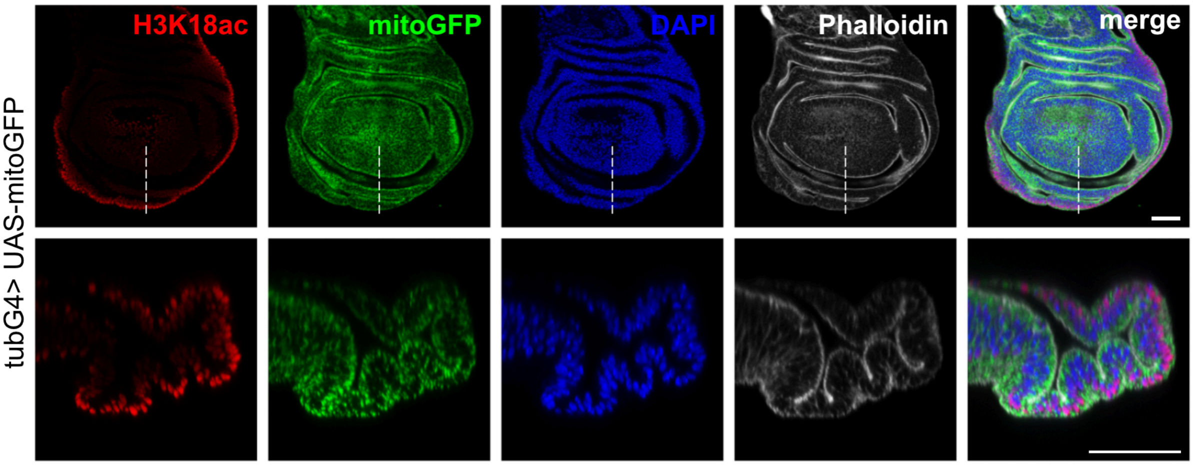

Fig. 55: Uniform distribution of mitochondria in the wing disc
High H3K18ac (red) in the rim of the wing disc is not caused by a higher concentration of mitochondria in this tissue, since mitochondrial distribution is rather uniform throughout the wing disc. Mitochondria are visualized by ubiquitous tubulinGAL4 (tubG4)-driven expression of mitochondrially-localized GFP (mitoGFP, green). The dashed lines in the overview images indicate the position of the cross-sections shown in the panels below. H3K18ac levels were assessed by immunostaining in wing discs of wandering third-instar larvae. Nuclei were counterstained with DAPI (blue). The disc outline is visualized by Phalloidin staining (white). Images are given in single or merged channel configurations. Scale bars: 50 µm

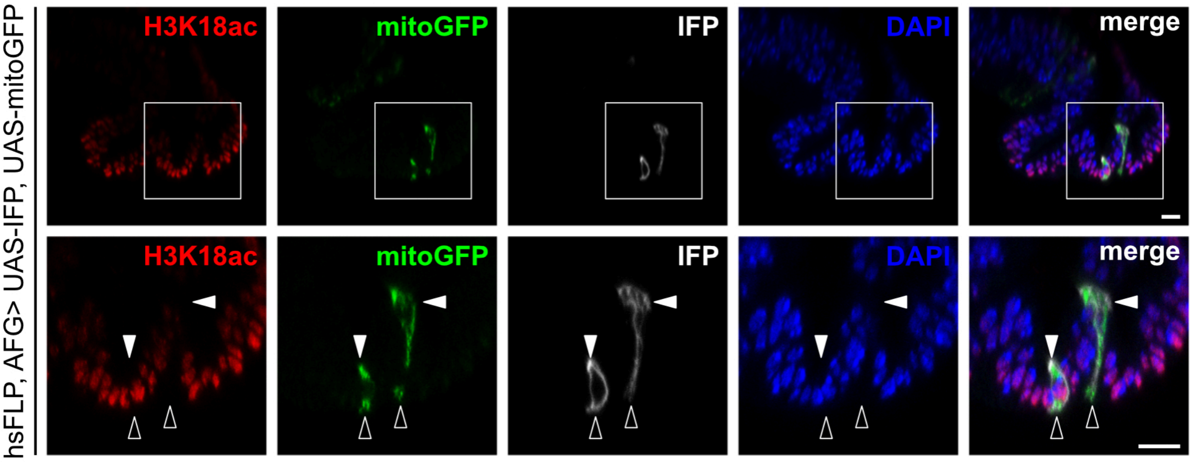

Fig. 56: Uniform subcellular distribution of mitochondria in the wing disc
Wing disc cells have apical (solid arrowheads) and basal mitochondria (open arrowheads) independent of nuclear position in the tissue and H3K18ac levels (red), arguing against a regulatory role for mitochondrial position in determining the non-uniform H3K18ac pattern. The white boxes in the overview images indicate the zoomed-in areas shown in the panels below. Mitochondria of individual cells were labeled by heat shock induced expression of mitochondrially-localized GFP (mitoGFP, green). The clones are marked by expression of membrane-tethered infra-red protein (IFP, white; see Material and Methods section 2.7 for details). H3K18ac levels were assessed by immunostaining in wing discs of wandering third-instar larvae. Nuclei were counterstained with DAPI (blue). Scale bars: 10 µm

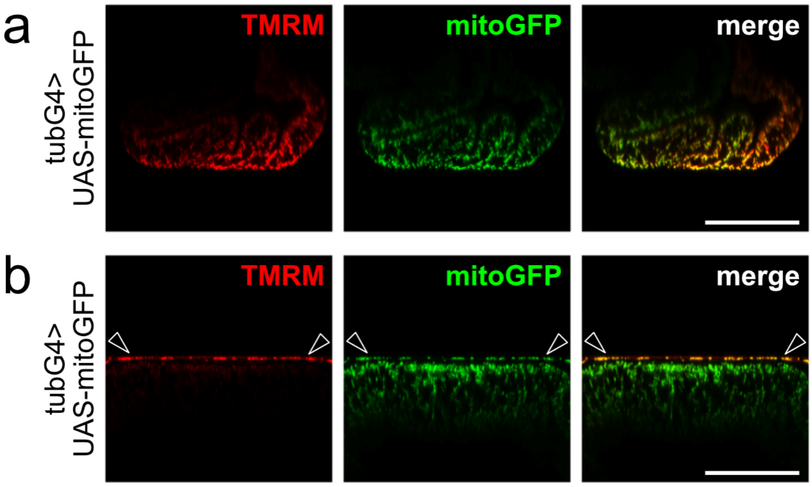

Fig. 57: Broad rim of high mitochondrial membrane potential in the wing disc
Cross-sections of wing discs show high mitochondrial membrane potential, visualized by mitochondrial accumulation of tetramethylrhodamine-methylester (TMRM, red), in (**a**) the proximal folds as well as (**b**) the peripodial membrane (arrowheads), indicating a broader distribution than that of high H3K18ac. Mitochondria are visualized by ubiquitous tubulinGAL4 (tubG4)-driven expression of mitochondrially-localized GFP (mitoGFP, green). Wing discs of wandering third-instar larvae were incubated for 30 min in explant cultures with TMRM. Images are given in single or merged channel configurations. Scale bars: 50 µm

3.5 Acetyl-CoA synthase generates acetyl-CoA for H3K18ac preferentially in outward-facing nuclei

Acetyl-CoA produced by fatty acid β-oxidation is localized in mitochondria and is typically converted to citrate or acetate for export into the cytoplasm[90] (Fig. 58). Citrate or acetate is then converted back to acetyl-CoA by ATP citrate lyase (ATPCL) or acetyl-CoA synthase (AcCoAS), respectively, for use in the nucleus.

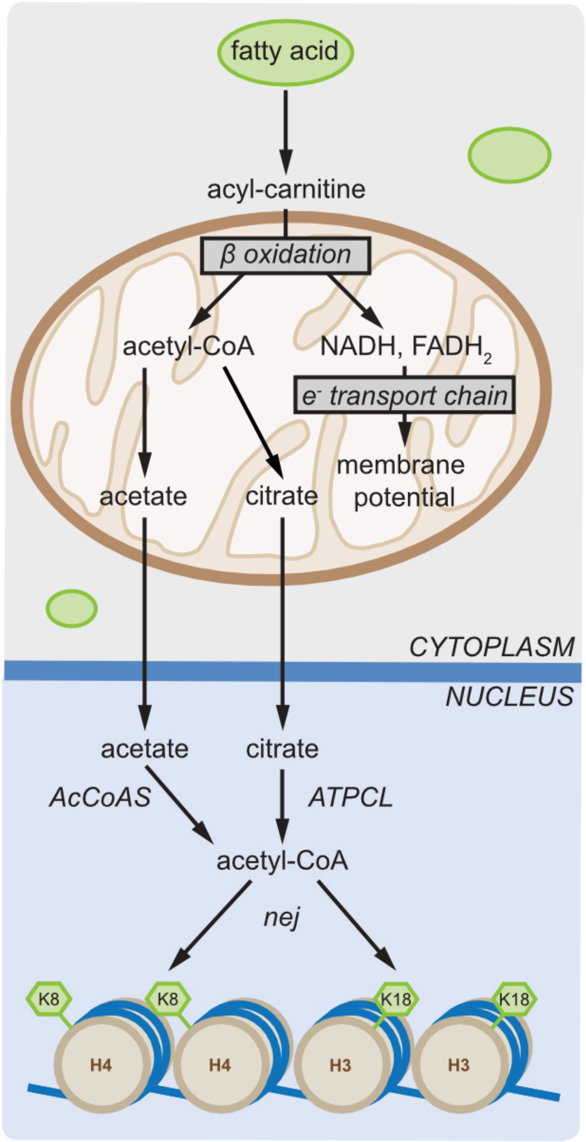

Fig. 58: Cellular acetyl-CoA metabolism
In mitochondria, fatty acid β-oxidation produces acetyl-CoA which is converted to acetate or citrate for export from this organelle. Acetate and citrate, in turn, are used to generate nuclear acetyl-CoA by acetyl-CoA synthase (AcCoAS) or ATP citrate lyase (ATPCL). Nuclear acetyl-CoA acts as essential metabolic substrate for acetyltransferases, such as nejire (nej), for acetylation of histones.

To determine which of the two enzymes is required for H3K18ac in the wing disc, I knocked down ATPCL in the posterior compartment, as validated by loss of the ATPCL immunosignal (Fig. 59a). However, this manipulation did not alter H3K18ac levels (Fig. 59b). Furthermore, citrate was not able to act as source for acetyl-CoA and rescue etomoxir-induced loss of H3K18ac when added exogenously to wing discs (Fig. 60). In line with these observations, pharmacological inhibition of ATPCL with BMS303141 failed to decrease H3K18ac levels (Fig. 61). Jointly, these results excluded involvement of ATPCL and its substrate citrate in the non-uniform histone acetylation pattern. In contrast, inhibition of AcCoAS with ACSS2 inhibitor (ACSS2i) strongly decreased H3K18ac levels (Fig. 61). Additionally, exogenous acetate was able to increase H3K18ac in the rim of the wing disc following etomoxir treatment (Fig. 62). Of note, acetate treatment alone significantly increased the ratio of H3K18ac in the rim versus the center of the disc. Blocking conversion of acetate to acetyl-CoA by AcCoAS inhibition with ACSS2i prevented acetate from rescuing H3K18ac levels in etomoxir-treated discs, validating specificity of the acetate rescue (Fig. 63).

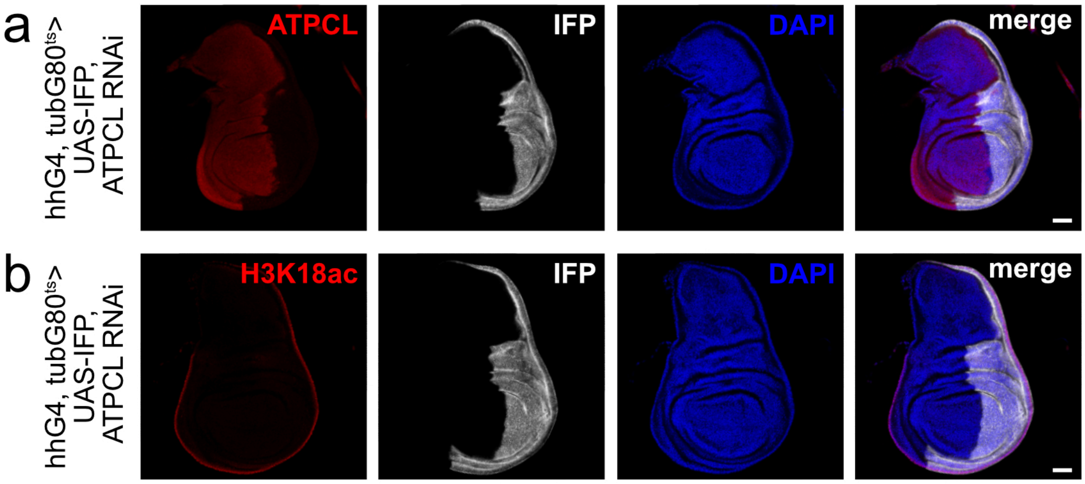

Fig. 59: H3K18ac does not require ATP citrate lyase-derived acetyl-CoA
Knockdown of ATP citrate lyase (ATPCL) in the posterior compartment (infra-red protein+, IFP+, white), driven by hedgehogGAL4 (hhG4) and validated by ATPCL immunostaining (**a**; red), does not impact H3K18ac levels (**b**; red). Temperature-sensitive knockdown of ATPCL was induced for 2 days at 29°C. ATPCL and H3K18ac levels were assessed by immunostaining in wing discs of wandering third-instar larvae. Nuclei were counterstained with DAPI (blue). Images are given in single or merged channel configurations. Scale bars: 50 µm

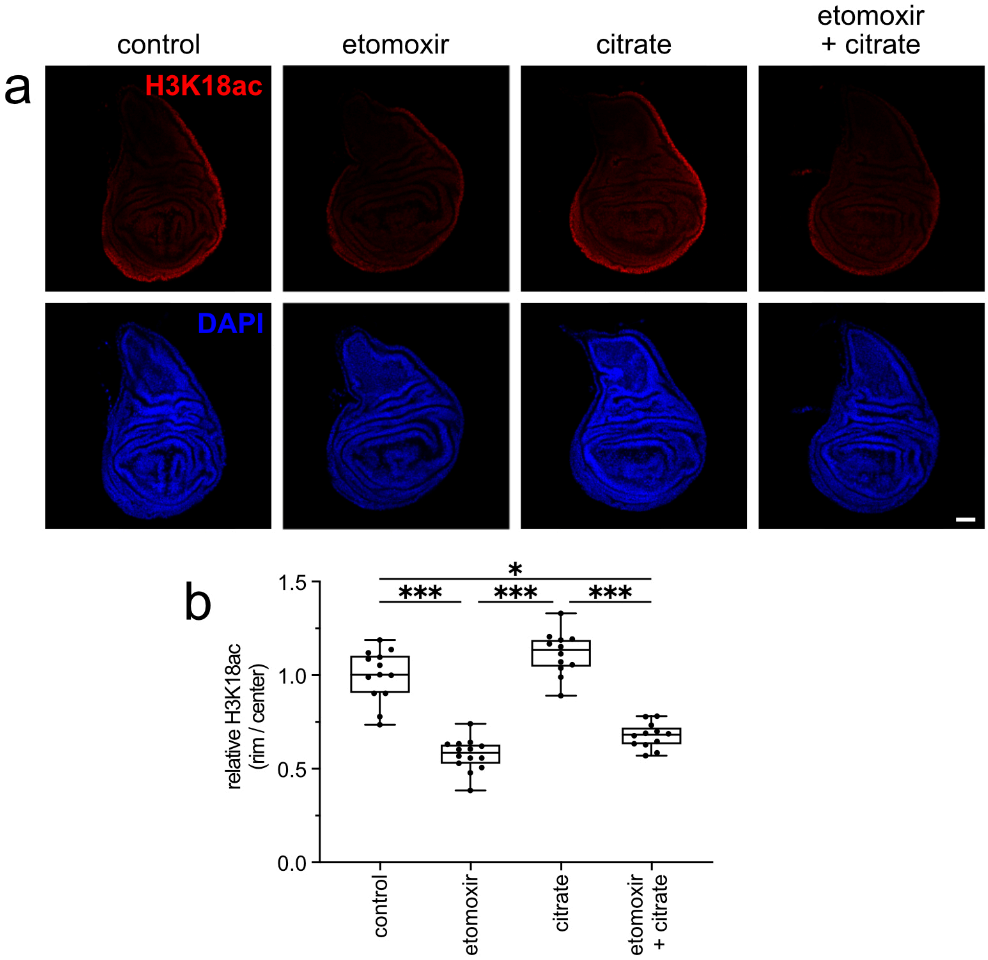

Fig. 60: Citrate does not rescue H3K18ac levels upon inhibition of fatty acid β-oxidation
Acetyl-CoA required for acetylation of H3K18 (red) is not derived from citrate, as citrate treatment (10 mM) does not rescue loss of H3K18ac upon inhibition of fatty acid β-oxidation (500 µM etomoxir). Also, citrate treatment in the absence of etomoxir does not impact H3K18ac levels. Wing discs of wandering third-instar larvae were incubated for 2 h in explant cultures with the indicated compounds before immunostaining of H3K18ac and nuclear counterstain with DAPI (blue). Representative images are shown in (**a**) and quantified in (**b**) with relative H3K18ac signal intensity expressed as a ratio of signal in the rim versus center of the disc. Statistical significance was determined by Kruskal-Wallis test with Dunn's multiple comparisons test (n=12-14 discs from 3 independent experiments; *<0.05, ***<0.001). Scale bar: 50 µm

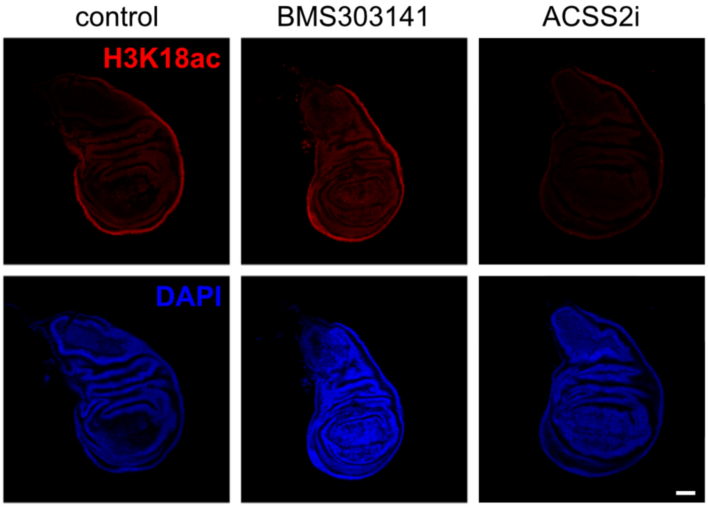

Fig. 61: H3K18ac depends on acetyl-CoA synthase-derived acetyl-CoA
Acetyl-CoA synthase (AcCoAS) provides acetyl-CoA for H3K18ac (red) as inhibition of AcCoAS (20 µM ACSS2 inhibitor, ACSS2i), but not of ATP citrate lyase (ATPCL; 50 µM BMS303141), causes loss of H3K18ac. Wing discs of wandering third-instar larvae were incubated for 2 h in explant cultures with the indicated inhibitors before immunostaining of H3K18ac and nuclear counterstain with DAPI (blue). Scale bar: 50 µm

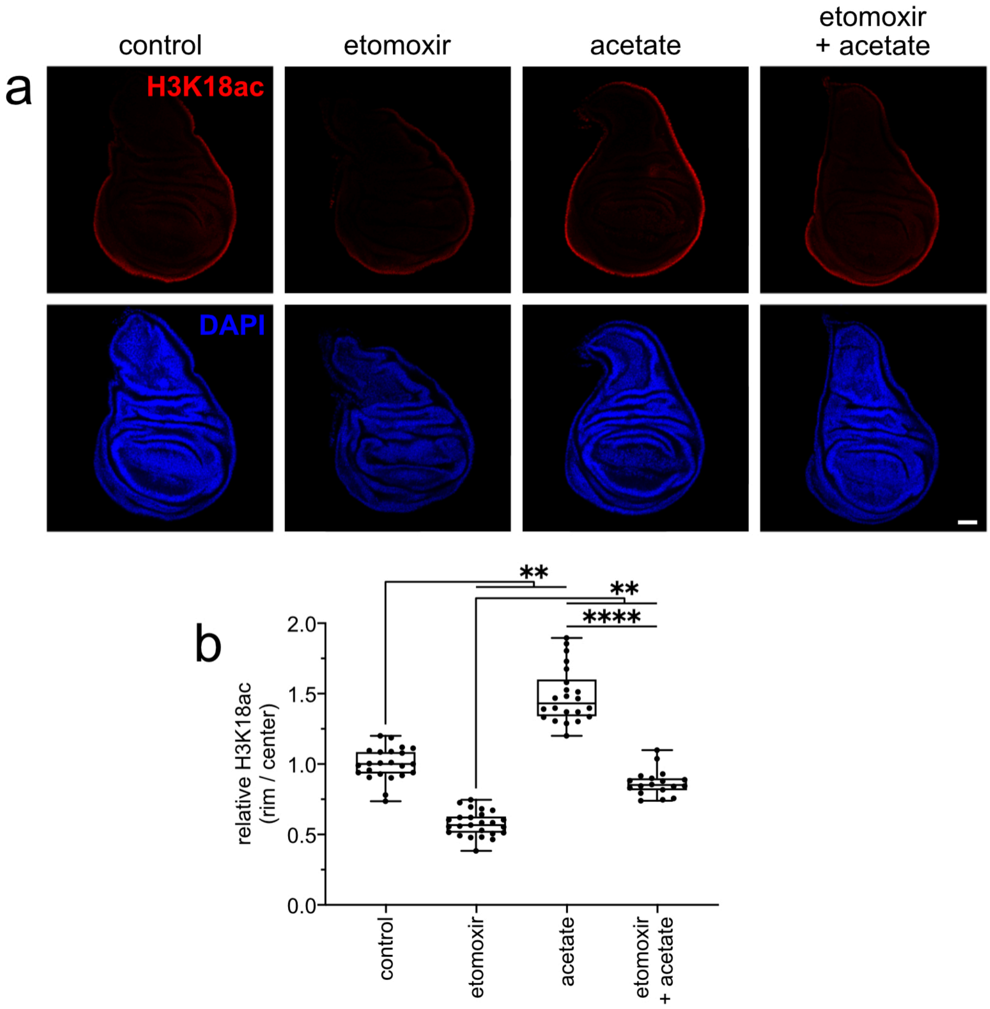

Fig. 62: Acetate rescues H3K18ac levels upon inhibition of fatty acid β-oxidation
Loss of H3K18ac (red) upon inhibition of fatty acid β-oxidation (500 µM etomoxir) is rescued by acetate (10 mM). Also, acetate treatment in the absence of etomoxir is sufficient to increase H3K18ac levels in the rim of the wing disc. Wing discs of wandering third-instar larvae were incubated for 2 h with the indicated compounds before immunostaining of H3K18ac and nuclear counterstain with DAPI (blue). Representative images are shown in (**a**) and quantified in (**b**) with relative H3K18ac signal intensity expressed as a ratio of signal in the rim versus center of the disc. Statistical significance was determined by Kruskal-Wallis test with Dunn's multiple comparisons test (n=18-25 discs from 5 independent experiments; **<0.01, ****<0.0001). Scale bar: 50 µm

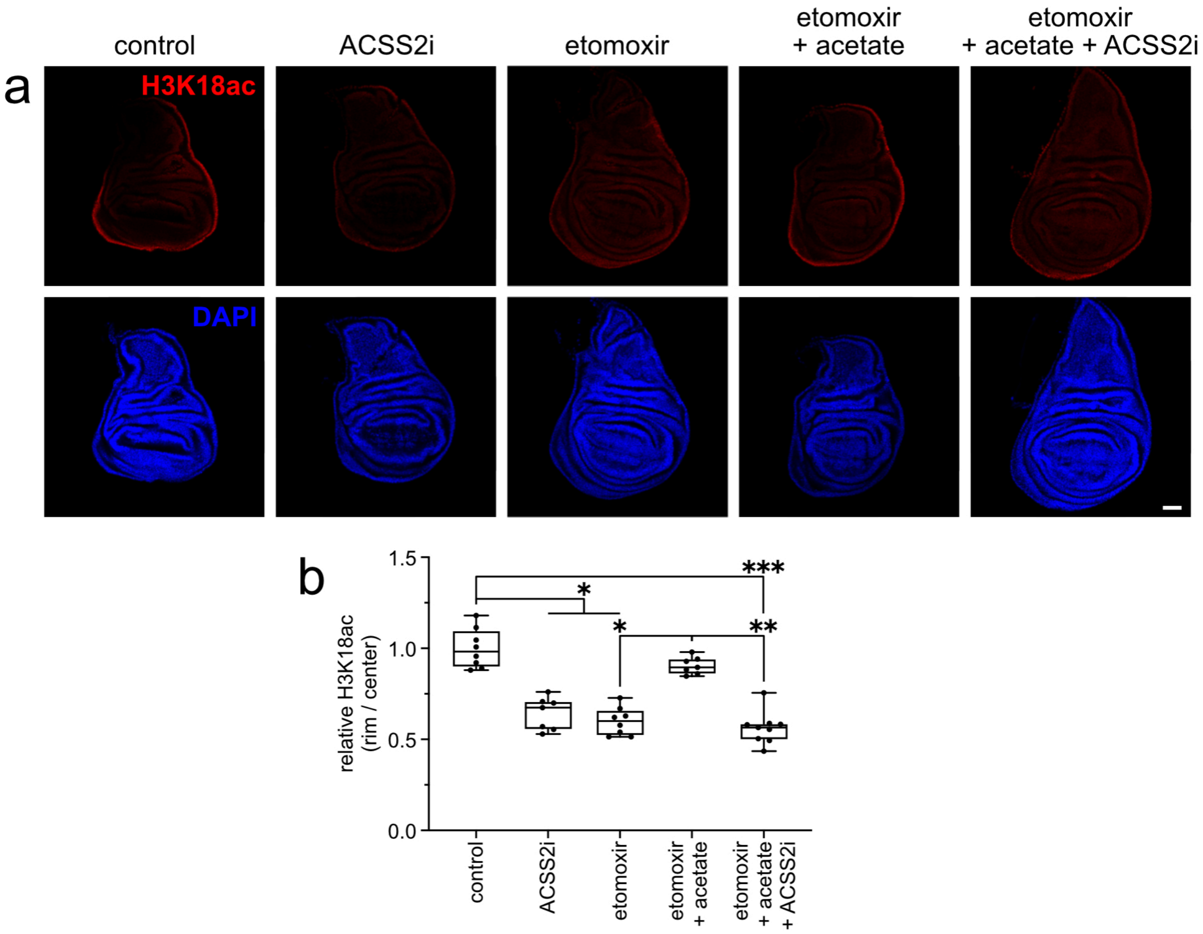

Fig. 63: Rescue of H3K18ac by acetate upon inhibition of fatty acid β-oxidation requires acetyl-CoA synthase activity

Rescue of etomoxir-induced (500 µM) loss of H3K18ac (red) by acetate (10 mM; panel etomoxir + acetate) is prevented by inhibition of acetyl-CoA synthase (AcCoAS) by ACSS2 inhibitor (ACSS2i, 20 µM; panel etomoxir + acetate +ACSS2i). As a control, loss of H3K18ac by treatment with etomoxir or ACSS2i alone is shown as well. Wing discs of wandering third-instar larvae were incubated for 2 h in explant cultures with the indicated compounds before immunostaining of H3K18ac and nuclear counterstain with DAPI (blue). Representative images are shown in (**a**) and quantified in (**b**) with relative H3K18ac signal intensity expressed as a ratio of signal in the rim versus center of the disc. Statistical significance was determined by Kruskal-Wallis test with Dunn's multiple comparisons test (n=7-9 discs from 2 independent experiments; *<0.05, **<0.01, ***<0.001). Scale bar: 50 µm

The above-mentioned results showed that acetate supplementation specifically increases H3K18ac in the rim of the disc, rather than uniformly throughout the tissue. To exclude inefficient tissue penetration rather than local conversion of acetate to acetyl-CoA as the reason for the local effect of acetate treatment on H3K18ac, I examined acetylation of α-tubulin lysine 40 (tubK40ac), which depends on cytosolic but not nuclear acetyl-CoA. Acetate treatment increased levels of tubK40ac throughout the disc (Fig. 64), documenting that exogenously added acetate is available to all cells in the tissue. The apparent difference in the response of cytosolic and nuclear acetylation to acetate implied fundamental differences in acetyl-CoA production in the two cell compartments. To query this hypothesis further, I tested the effect of acetate treatment on other non-uniform (H4K8ac and ac-K) and uniform acetylation marks (H3K9ac and H3K27ac). Interestingly, acetate did not only increase levels of non-uniform acetylation marks (Fig. 65a-c and f) but also levels of the normally uniform H3K9ac and H3K27ac specifically in the rim of the wing disc (Fig. 65d-f). Cross-sections of discs immunostained for H3K18ac and H3K9ac illustrated this rim-specific effect of acetate, showing increased histone acetylation in nuclei facing the tissue surface (Fig. 66, solid arrowheads) but no change in inward-facing nuclei (Fig. 66, open arrowheads) upon acetate treatment. As this specific increase in histone acetylation in the rim was seen for targets of nej (H3K18ac) and Gcn5 (H3K9ac; Figs. 20 and 21, respectively), local nuclear production of acetyl-CoA from acetate likely represents a regulatory principle for multiple acetyltransferases.

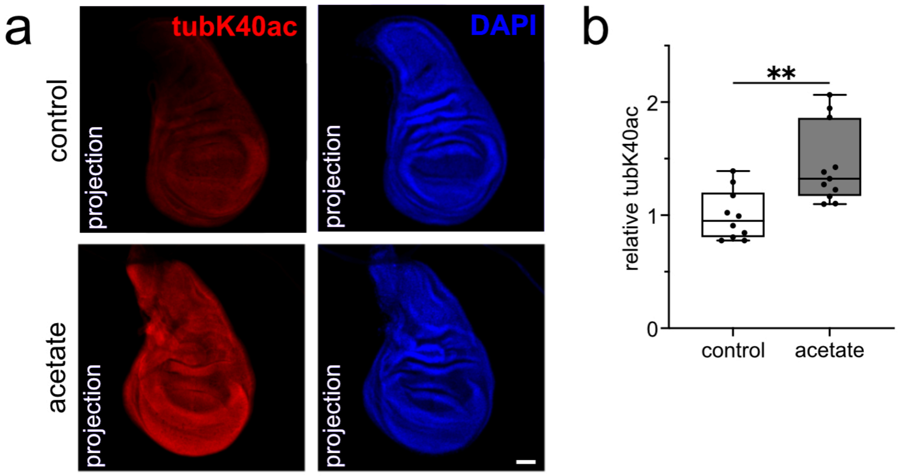

Fig. 64: Exogenous acetate is able to penetrate the entire wing disc tissue
Acetate treatment (10 mM) increases acetylation of cytoplasmic α-tubulin lysine 40 (tubK40ac, red) in the entire wing disc, excluding insufficient tissue penetration as the reason for the rim-specific effects of acetate treatment on H3K18ac. Wing discs of wandering third-instar larvae were incubated for 2 h in explant cultures in the presence or absence of acetate before immunostaining of tubK40ac and nuclear counterstain with DAPI (blue). Representative images of sum projections are shown in (**a**) and quantified in (**b**) as relative tubK40ac intensities. Statistical significance was determined by Kruskal-Wallis test with Dunn’s multiple comparisons test (n=10-11 discs from 2 independent experiments; **<0.01). Scale bar: 50 µm

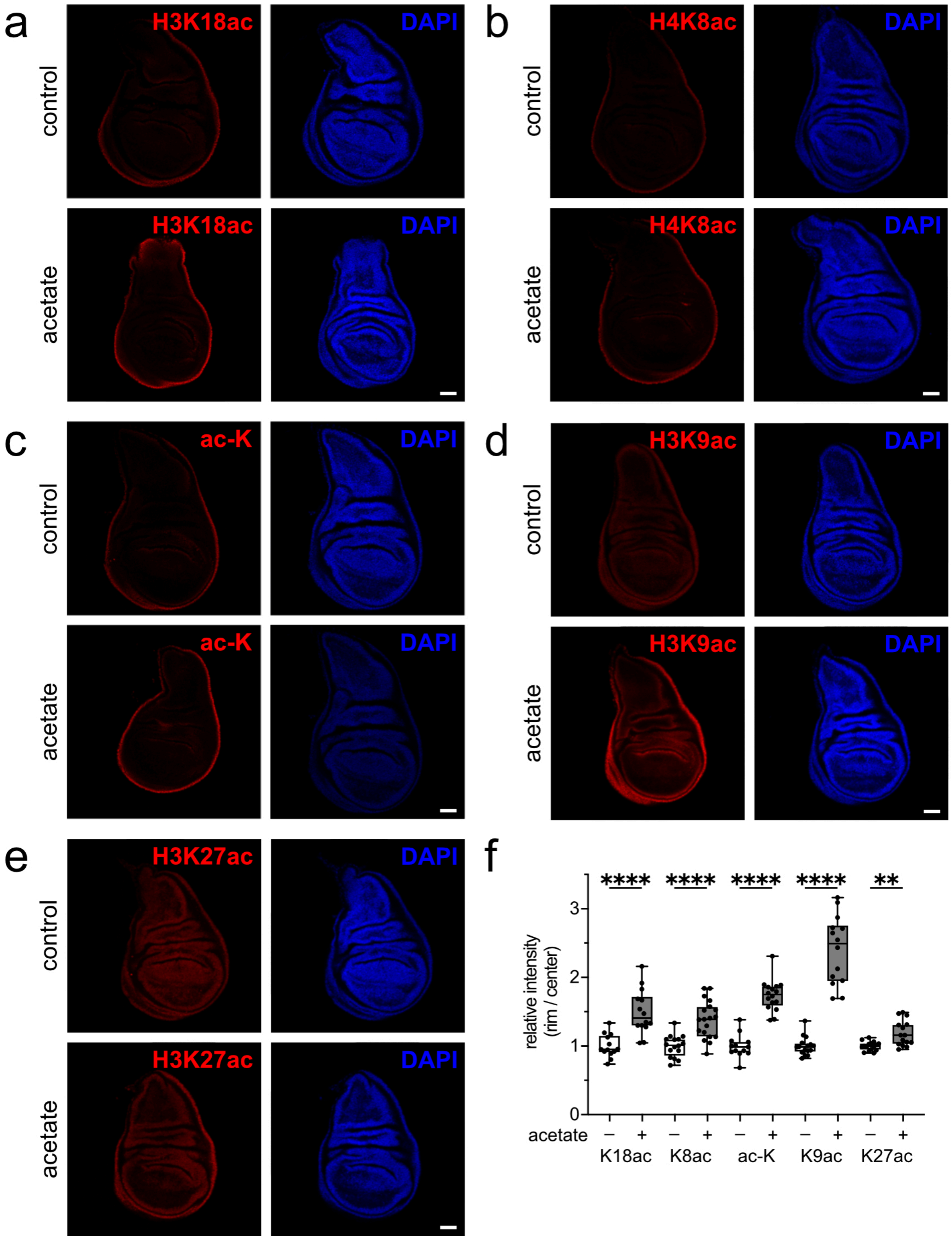

Fig. 65: Acetate preferentially increases acetylation in the rim of the wing disc
(**a-e**) Incubation with acetate (10 mM) causes an increase in histone acetylation in the rim but not in the pouch of the wing disc, as shown for (a) H3K18ac, (b) H4K8ac, (c) total acetylated lysine (ac-K), (d) H3K9ac, and (e) H3K27ac. Wing discs of wandering third-instar larvae were incubated for 2 h in explant cultures in the presence or absence of acetate before immunostaining of the indicated acetylation marks (red) and nuclear counterstain with DAPI (blue). Representative images are shown in (a-e) and quantified in (**f**) with relative signal intensities expressed as a ratio of signal in the rim versus center of the disc. Statistical significance was determined by Mann-Whitney test (n=13-19 discs from 3 independent experiments; **<0.01, ****<0.0001). Scale bars: 50 µm

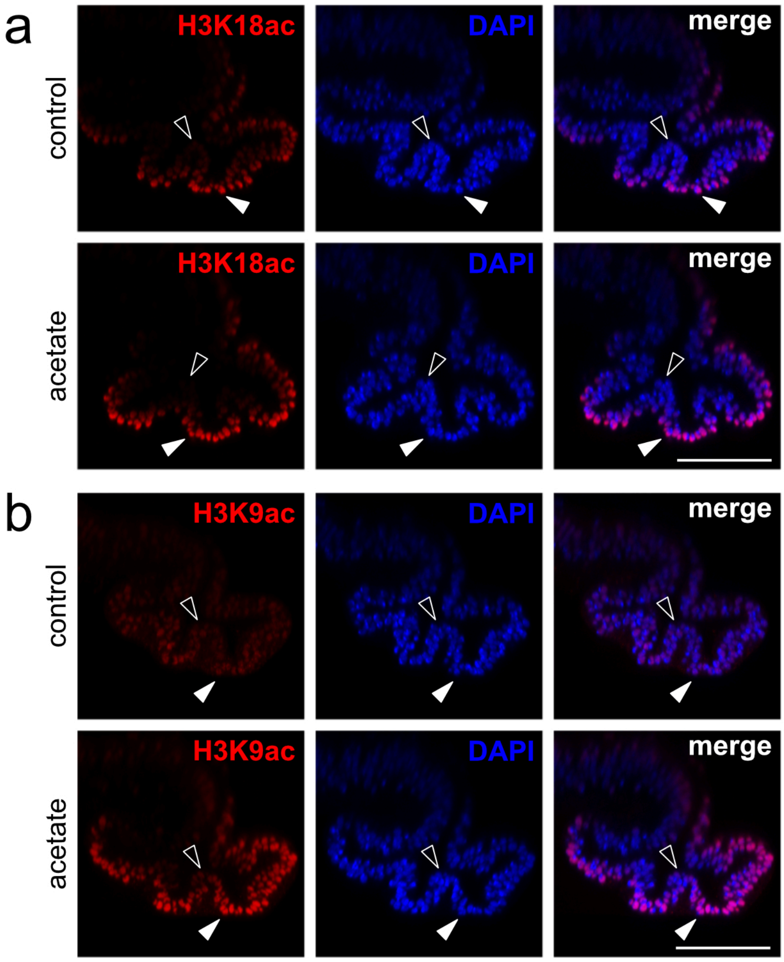

Fig. 66: Local nuclear conversion of acetate to acetyl-CoA in outward-facing nuclei
Acetate treatment only increases acetylation of histones in outward-facing nuclei. Cross-sections of acetate-treated (10 mM) discs immunostained for (**a**) H3K18ac or (**b**) H3K9ac show increased histone acetylation in nuclei facing the tissue surface (solid arrowheads) but not the tissue interior (open arrowheads). Wing discs of wandering third-instar larvae were incubated for 2 h in explant cultures in the presence or absence of acetate before immunostaining of the indicated acetylation marks (red) and nuclear counterstain with DAPI (blue). Images are given in single or merged channel configurations. Scale bars: 50 µm

AcCoAS can localize to the nucleus to locally generate acetyl-CoA for histone acetylation[91–93]. To examine if this mechanism was responsible for the rim-specific impact of acetate on histone acetylation in the disc, I analyzed the distribution of AcCoAS in the wing disc by immunostaining. Specificity of the AcCoAS antibody was validated by overexpression of AcCoAS in the posterior disc, resulting in increased immunosignal of the enzyme as compared to the anterior tissue (Fig. 67a). X-y sections of wing discs revealed a rather uniform distribution of endogenous AcCoAS in the wing disc tissue (Fig. 67b). However, upon closer inspection of cross-sections of AcCoAS over-expressing wing discs, a non-uniform subcellular distribution of AcCoAS was evident with higher nuclear levels in outward-facing nuclei as compared to nuclei facing the tissue interior (Fig. 68). The same subcellular pattern was observed when inspecting levels of endogenous AcCoAS (Fig. 69), excluding an artefact from protein over-expression.

Correlation of nuclear AcCoAS levels with nuclear distance to the tissue surface, and hence, H3K18ac levels, suggested nuclear AcCoAS activity as a possible determining factor for the non-uniform histone acetylation pattern in the disc.

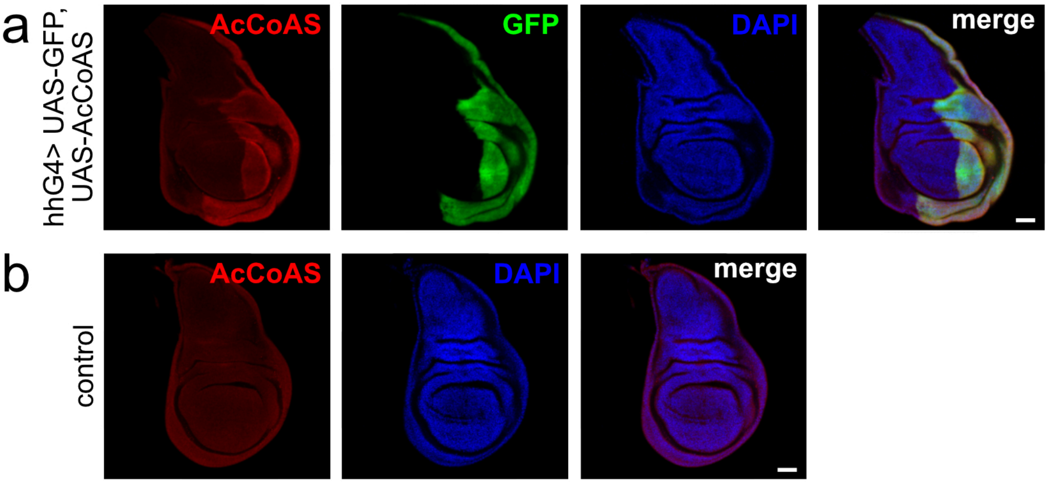

Fig. 67: Uniform distribution of acetyl-CoA synthase in the wing disc
(**a**) Specificity of the antibody directed against acetyl-CoA synthase (AcCoAS, red) was validated by hedgehogGAL4 (hhG4)-driven overexpressing of AcCoAS in the posterior compartment (GFP+, green), causing increased immunosignal. (**b**) Endogenous AcCoAS protein is uniformly distributed in the wing disc. AcCoAS levels were assessed by immunostaining in wing discs of wandering third-instar larvae. Nuclei were counterstained with DAPI (blue). Images are given in single or merged channel configurations. Scale bars: 50 µm

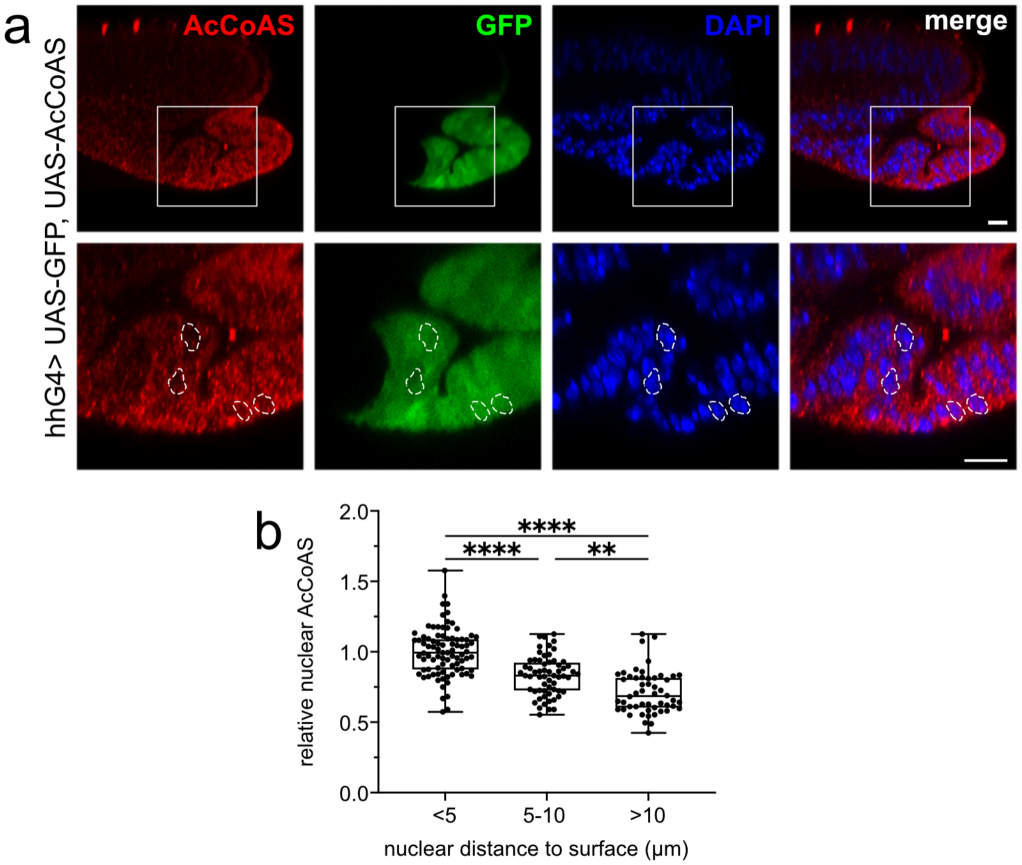

Fig. 68: Enrichment of over-expressed acetyl-CoA synthase in outward-facing nuclei
Levels of acetyl-CoA synthase (AcCoAS, red) overexpressed in the posterior compartment (GFP+, green), driven by hedgehogG4 (hhG4), are higher in nuclei facing the surface of the disc tissue but lower in nuclei facing the tissue interior. The white boxes in the overview images indicate the position of the zoom-ins shown in the panels below. AcCoAS levels were assessed by immunostaining in wing discs of wandering third-instar larvae. Nuclei were counterstained with DAPI (blue). Representative images are shown in (**a**) and quantified in (**b**) with nuclear AcCoAS levels plotted against nuclear distance to the tissue surface. Statistical significance was determined by Kruskal-Wallis test with Dunn's multiple comparisons test (n=56-86 nuclei from 4 wing discs with 2-3 sections each; **<0.01, ****<0.0001). Scale bars: 10 µm

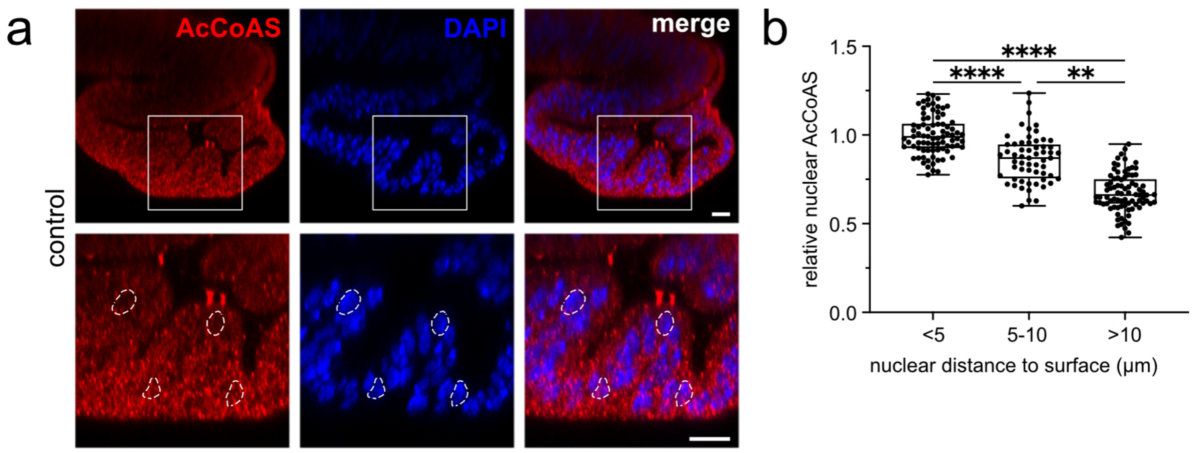

Fig. 69: Enrichment of endogenous acetyl-CoA synthase in outward-facing nuclei
Levels of endogenous acetyl-CoA synthase (AcCoAS, red) are higher in nuclei facing the surface of the disc tissue but lower in nuclei facing the tissue interior. The white boxes in the overview image indicate the position of the zoom-ins shown in the panels below. AcCoAS levels were assessed by immunostaining in wing discs of wandering third-instar larvae. Nuclei were counterstained with DAPI (blue). Representative images are shown in (**a**) and quantified in (**b**) with nuclear AcCoAS levels plotted against nuclear distance to the tissue surface. Statistical significance was determined by Kruskal-Wallis test with Dunn's multiple comparisons test (n=59-83 nuclei from 4 wing discs with 2 sections each; **<0.01, ****<0.0001). Scale bars: 10 μm

3.6 Non-uniform histone acetylation regulates gene expression in the wing disc

So far, my data suggested that mitochondrial acetyl-CoA derived from fatty acid β-oxidation is converted to acetate, which, in turn, is used for acetyl-CoA production specifically by nuclear AcCoAS in outward-facing nuclei. This locally restricted process determines the non-uniform activity of histone acetyltransferases, such as nej (Fig. 70). These data raise the intriguing possibility that localization of cells in the developing tissue, as sensed by nuclear position relative to the tissue surface, may exert metabolic control of epigenetic gene expression, potentially regulating cell function and fate and, hence, tissue development.

To confirm the effect of H3K18ac on gene expression, I performed cleavage under targets and release using nuclease (Cut&Run)[64] on wing discs, a method similar to chromatin immunoprecipitation to assess the distribution of histone modifications in the genome. Cut&Run is based on a fusion protein containing a protein A domain, which binds to the primary antibody, here an antibody against H3K18ac, and a micrococcal nuclease, cutting the DNA around the binding site. Genomic DNA fragments generated by nuclease cleavage at

H3K18ac sites are purified and identified by sequencing (see Material and Methods section 2.6 for details).

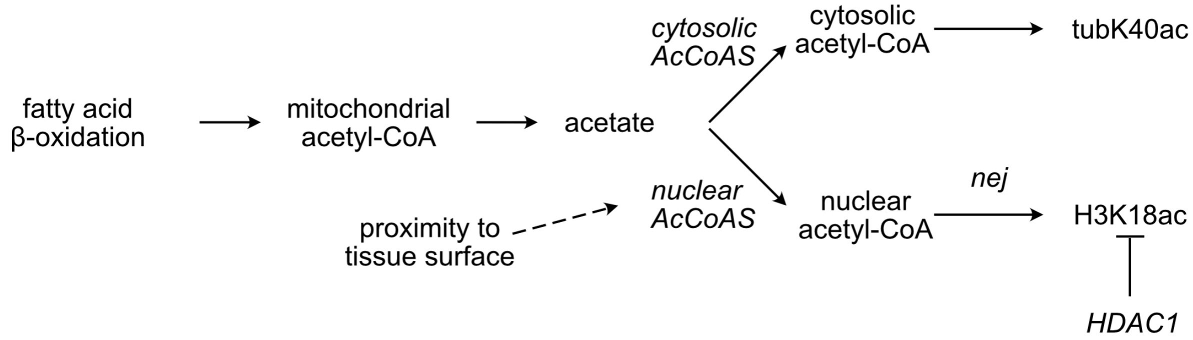

Fig. 70: Proposed model for regulation of H3K18ac in the wing disc
Mitochondrial fatty acid β-oxidation generates acetyl-CoA which is converted to acetate and exported. Acetate, in turn, is used to produce nuclear acetyl-CoA required for histone acetylation. In addition, nuclear conversion of acetate depends on nuclear acetyl-CoA synthase (AcCoAS) activity, which may be induced in outward-facing nuclei due to the proximity to the tissue surface. High nuclear acetyl-CoA levels cause nejire (nej)-dependent acetylation of H3K18, which is counter-regulated by histone deacetylase 1 (HDAC1).

Using Cut&Run, I specifically determined the genomic distribution of H3K18ac in discs either non-treated or treated with etomoxir to identify genes with fatty acid β-oxidation-dependent histone acetylation marks. Principle component analysis of the data set showed clear clustering of treated (n=2) and control replicates (n= 3) within each condition group (Fig. 71a), validating the robustness of my data set.

Identified H3K18ac peaks (9621) were mostly localized in promoter regions, especially in proximal promoters (≤ 1 kb; Fig. 71b), as expected for histone acetylation[78,94], verifying the validity of my experimental procedure. Fatty acid β-oxidation dependent peaks (2194) mostly showed the expected decreased H3K18ac levels upon etomoxir treatment (Fig. 71c). These downregulated peaks corresponded to 1469 individual genes. Typically, genes with strongly decreased H3K18ac peaks upon etomoxir treatment, and hence, high gene rank in the hit list, were associated with multiple peaks (Fig. 72), further validating the dependency of their histone acetylation on fatty acid β-oxidation. Gene ontology (GO) enrichment analysis of this subset of genes revealed their involvement in biological processes of tissue development, regulation of gene expression as well as in signaling pathways regulating cell fate in the wing disc, including Hippo, Notch, Mitogen-activated protein kinase (MAPK), and Hh (Fig. 73).

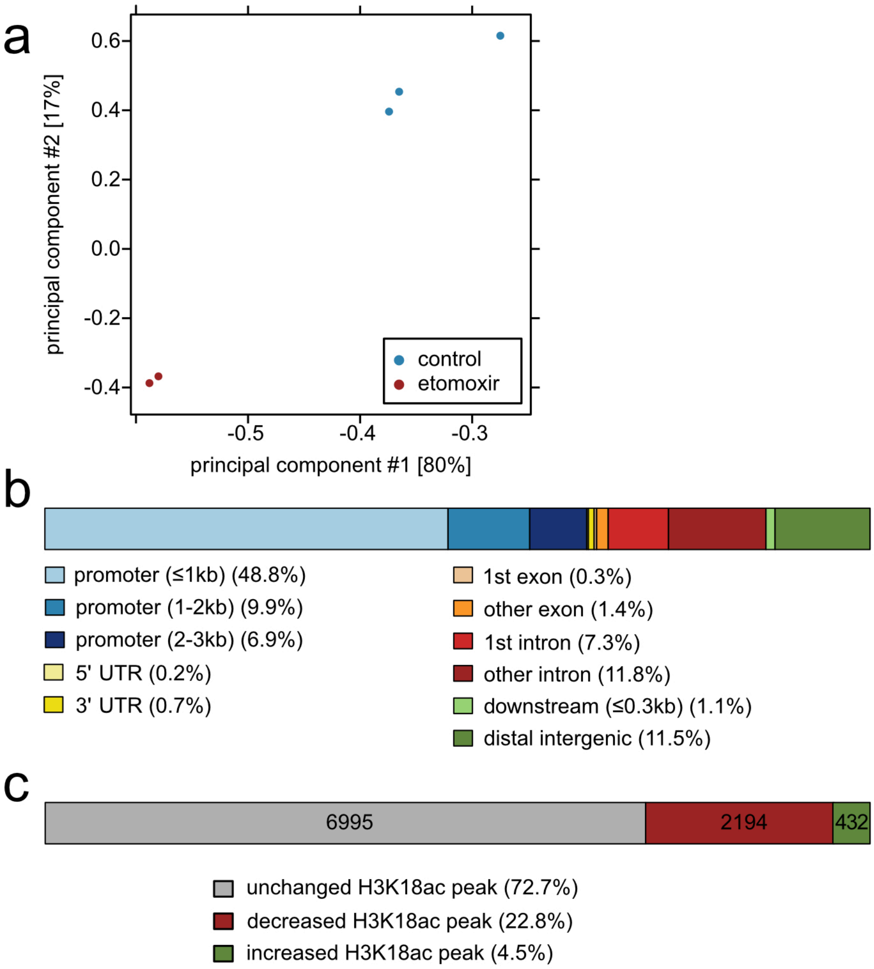

Fig. 71: Analysis of genomic distribution of H3K18ac in the wing disc
Cleavage under targets and release using nuclease (Cut&Run) was used to identify fatty acid β-oxidation-dependent histone acetylation in the wing disc. To do so, wing discs of wandering third-instar larvae were incubated for 2 h in explant cultures in the presence or absence of etomoxir or directly used to determine H3K18ac peaks in the genome by Cut&Run (see Material and Methods section 2.6 for details). (**a**) Principal component analysis of Cut&Run samples reveals clustering of control (blue) and etomoxir-treated samples (red). (**b**) Analysis of the genomic distribution of H3K18ac peaks shows the expected enrichment of the mark in promoter regions (blue). (**c**) Comparison of H3K18ac peak distribution in control and etomoxir-treated samples documents that inhibition of fatty acid β-oxidation preferentially decreases (2194 gene peaks) rather than increases (432 gene peaks) H3K18ac marks.

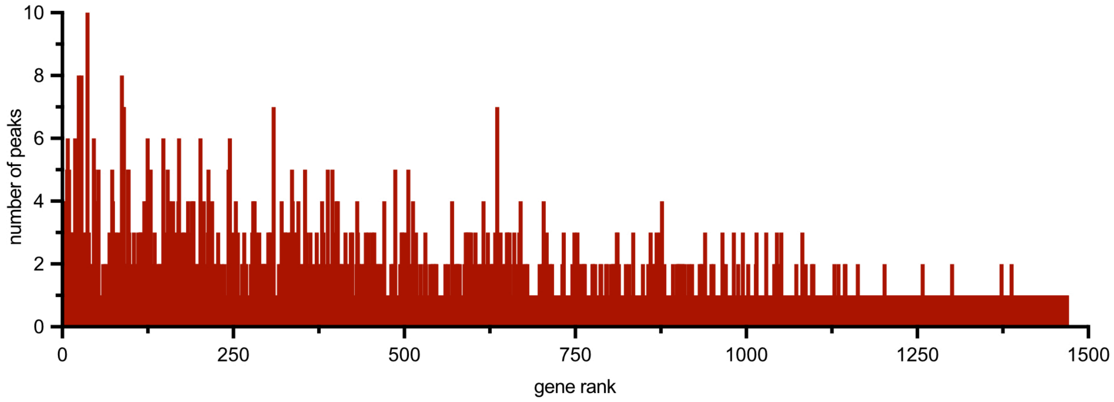

Fig. 72: Genes with fatty acid β-oxidation-dependent H3K18ac peaks are often associated with multiple peaks

Gene rank is plotted against number of peaks associated with a specific gene. Genes are sorted in a descending manner by fold-change of the most strongly decreased peak associated with the specific gene.

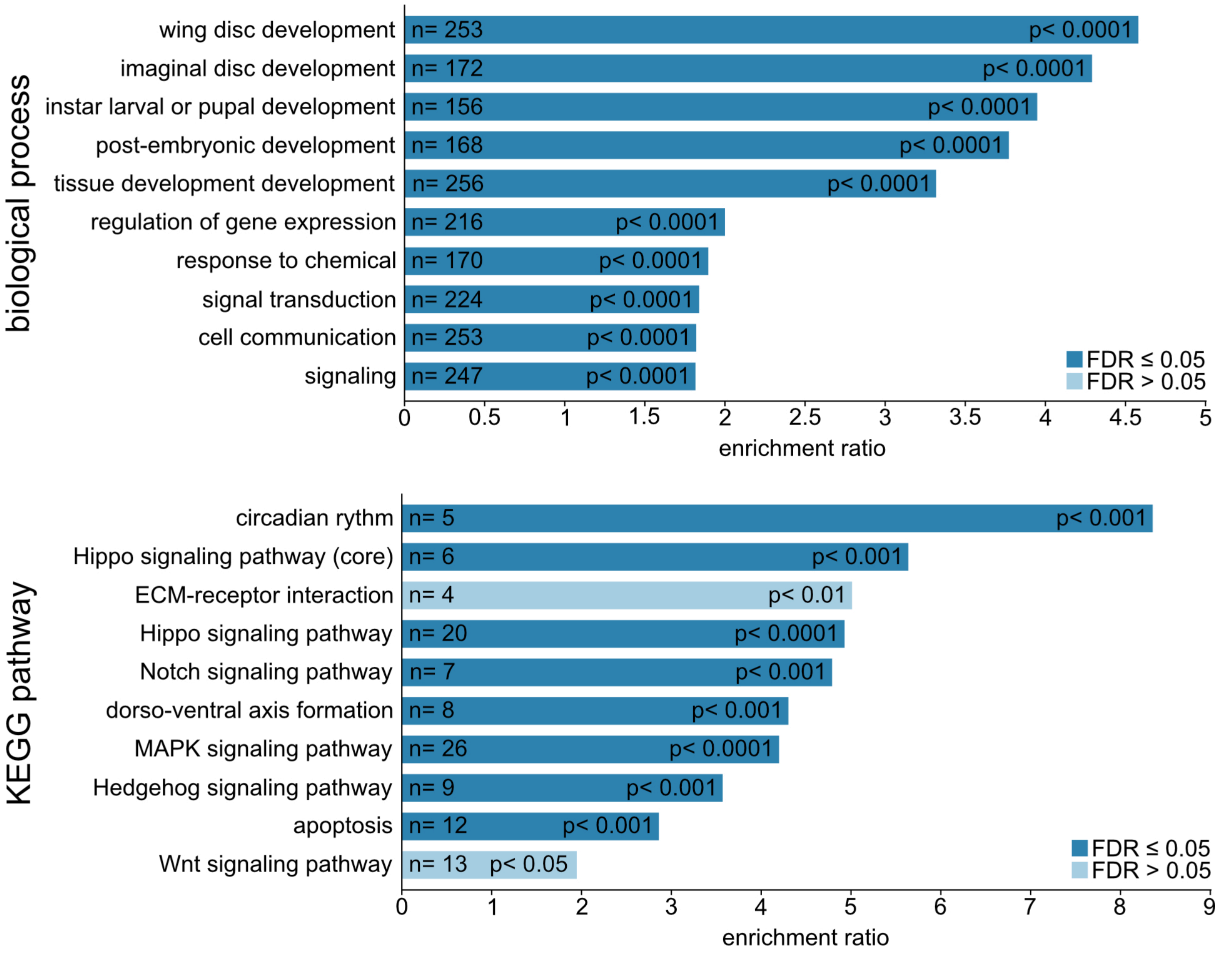

Fig. 73: Genes with fatty acid β-oxidation-dependent H3K18ac peaks are involved in tissue development and signaling

Gene ontology enrichment analysis of genes with fatty acid β-oxidation-dependent H3K18ac peaks documents involvement in biological processes of tissue development, gene expression, cell communication, and signal transduction. Involved signaling pathways encompass Hippo, Notch, Mitogen-activated protein kinase (MAPK), as well as Hedgehog. Number of genes (n) in the different groups as well as the p value (p) and false discovery rate (FDR) of their enrichment are indicated.

The list of genes with etomoxir-downregulated peaks contained multiple proximally expressed genes, including mirror (mirr; Fig. 74a), Sox box protein 15 (Sox15; Fig. 74b), homothorax (hth; Fig. 74c), drumstick (drm; Fig. 75a), E5 (Fig. 75b), grain (grn, Fig. 75c), maternal gene required for meiosis (mamo; Fig. 76a), and Zn finger homeodomain 2 (zfh2; Fig. 76b). I confirmed the dependency of transcription of these genes on non-uniform histone acetylation. Downregulation of histone acetylation with etomoxir, as used for Cut&Run, was not feasible for assessing the effect of decreased acetylation on transcript levels by FISH as the prolonged drug treatment required to see changes in transcription caused loss of tissue integrity. Instead, I knocked down nej in the posterior compartment, which had a similar effect on H3K18ac and ac-K as inhibition of fatty acid β-oxidation (Figs. 20a, 23-24, and 43). All tested transcripts were strongly down regulated in the affected compartment (Figs. 74a'-c', 75a'-c', and 76a'-b', arrowheads), indicating requirement of nej-dependent histone acetylation for proper gene expression. In contrast, transcription of the gene encoding glyceraldehyde 3 phosphate dehydrogenase 2 (Gapdh2), used as a negative control, was not impacted (Fig. 76c-c').

Taken together, my data indicate that metabolite-dependent, non-uniform histone acetylation in the wing disc induces transcription of a subset of genes involved in tissue development and signaling, suggesting epigenetic control of cell and wing disc fate.

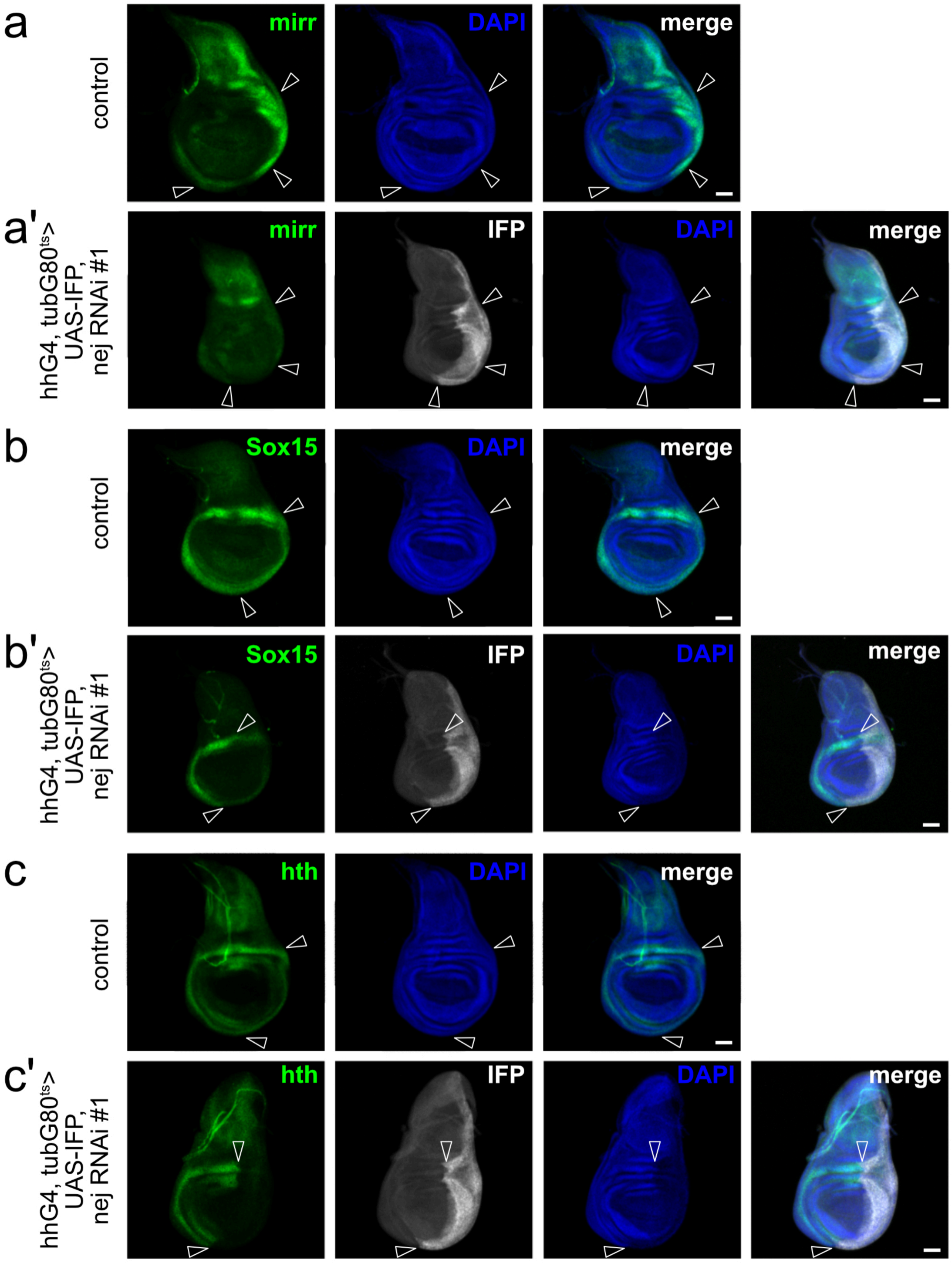

Fig. 74: Nejire regulates transcription of proximal genes with fatty acid β-oxidation-dependent H3K18ac peaks

(**a**-**c**) Multiple genes with fatty acid β-oxidation-dependent H3K18ac peaks have a proximal expression pattern, as documented by fluorescence *in situ* hybridization (FISH; green) for (a) mirror (mirr), (b) Sox box protein 15 (Sox15), and (c) homothorax (hth). (**a'**-**c'**) Transcription of these proximal genes requires nejire (nej)-dependent histone acetylation, as knockdown of nej in the posterior compartment (infra-red protein+, IFP+, white), driven by hedgehogGAL4 (hhG4) causes a strong decrease of FISH signal (arrowheads). Temperature-sensitive knockdown of nej was induced for 1.5 days at 29°C. Nuclei were counterstained with DAPI (blue). Images are given in single or merged channel configurations. Scale bars: 50 µm

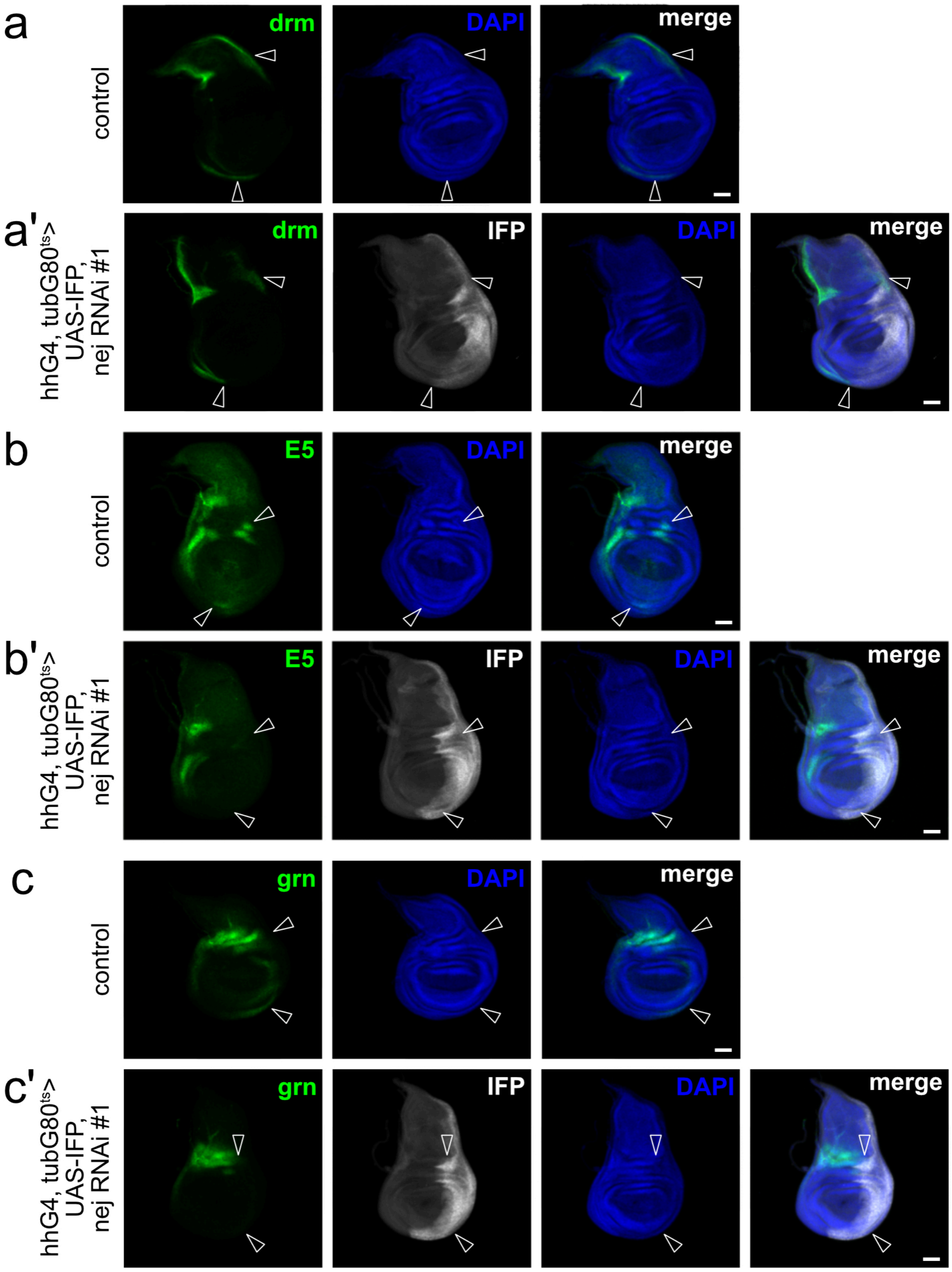

Fig. 75: Nejire regulates transcription of proximal genes with fatty acid β-oxidation-dependent H3K18ac peaks

(**a-c**) Additional genes with fatty acid β-oxidation-dependent H3K18ac peaks have a proximal expression pattern, as documented by fluorescence *in situ* hybridization (FISH; green) for (a) drumstick (drm), (b) E5, and (c) grain (grn). (**a'-c'**) Transcription of these genes requires nejire (nej)-dependent histone acetylation, as knockdown of nej in the posterior compartment (infra-red protein+, IFP+, white), driven by hedgehogGAL4 (hhG4) causes a strong decrease of fluorescence signal (arrowheads). Temperature-sensitive knockdown of nej was induced for 1.5 days at 29°C. Nuclei were counterstained with DAPI (blue). Images are given in single or merged channel configurations. Scale bars: 50 µm

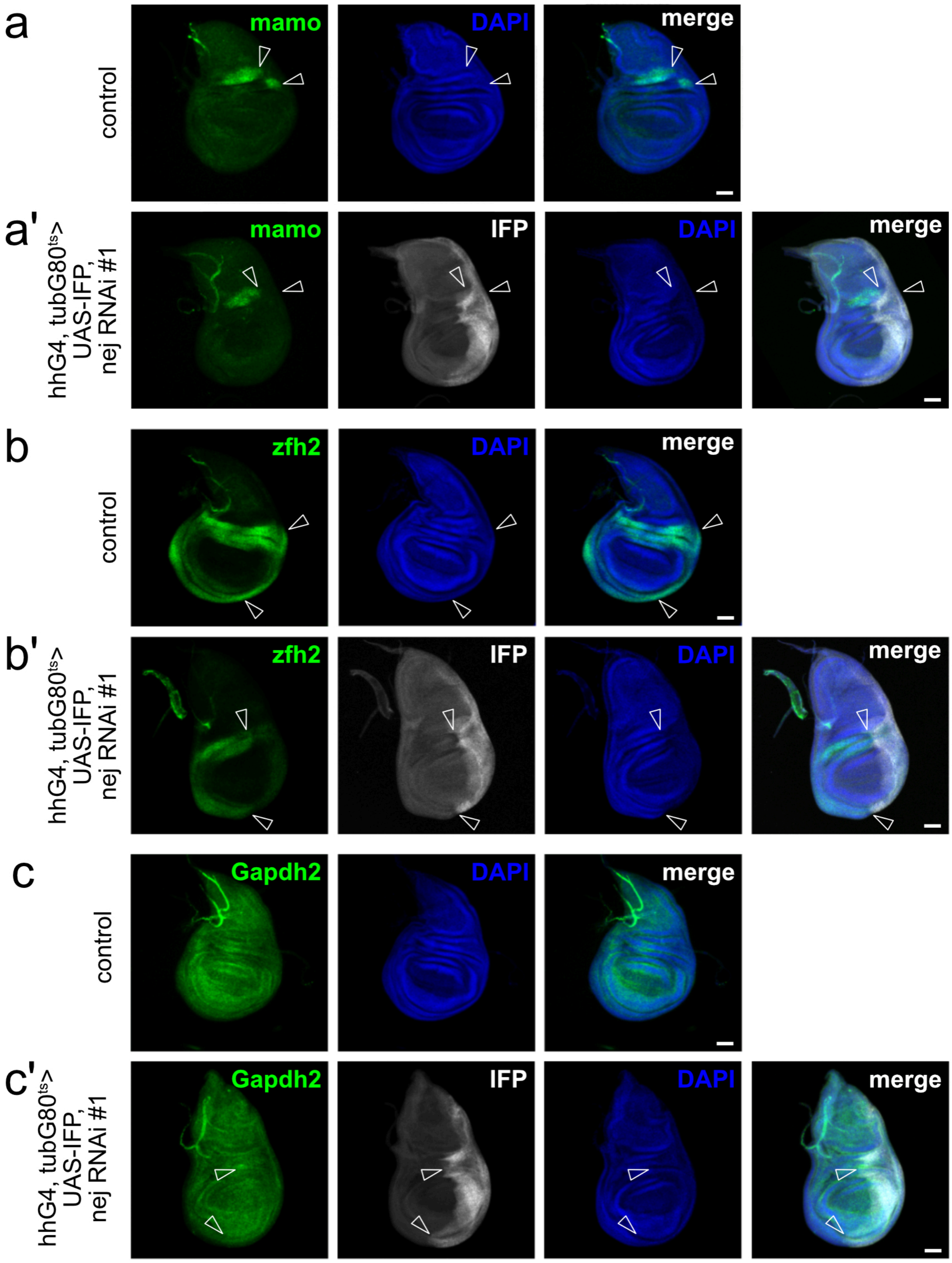

Fig. 76: Nejire regulates transcription of proximal genes with fatty acid β-oxidation-dependent H3K18ac peaks

(**a-b**) Additional genes with fatty acid β-oxidation-dependent H3K18ac peaks have a proximal expression pattern, as documented by fluorescence *in situ* hybridization (FISH; green) of (a) maternal gene required for meiosis (mamo) and (b) Zn finger homeodomain 2 (zfh2). (**a**'-**b'**) Transcription of these genes requires nejire (nej)-dependent histone acetylation, as knockdown of nej in the posterior compartment (infra-red protein+, IFP+, white), driven by hedgehogGAL4 (hhG4) causes a strong decrease of fluorescence signal (arrowheads). (**c-c'**) As a negative control, expression of the house-keeping gene glyceraldehyde-3-phosphate dehydrogenase 2 (Gapdh2) is not impacted by nej knockdown. Temperature-sensitive knockdown of nej was induced for 1.5 days at 29°C. Nuclei were counterstained with DAPI (blue). Images are given in single or merged channel configurations. Scale bars: 50 µm

4. Discussion

4.1 Nuclear positioning and a non-uniform metabolism exert epigenetic control of gene expression in the wing disc

The aim of this PhD project was to investigate the relevance of cellular metabolism and nuclear positioning in tissue development using the wing imaginal disc as a model of a pseudostratified epithelium. My findings are summarized in figure 77. In detail, I document a non-uniform distribution of histone acetylation in the wing disc, exemplified by H3K18ac, with high acetylation levels in the rim of the disc. High levels of H3K18ac specifically in nuclei facing the tissue exterior are not determined by cell cycle or clonal heritage but by the relative position of the nuclei within the wing disc tissue. Outside-facing nuclei display higher levels of nuclear AcCoAS, which produces nuclear acetyl-CoA from acetate required as metabolic substrate for histone acetylation. This rim acetylation pattern is dependent on acetate derived from fatty acid β-oxidation, which is also non-uniform in the wing disc, as visualized by high mitochondrial membrane potential in the rim of the tissue. This acetylation pattern, regulated by nuclear position and aligned with cellular metabolism, exerts epigenetic control of developmentally important signaling pathways in the developing wing disc.

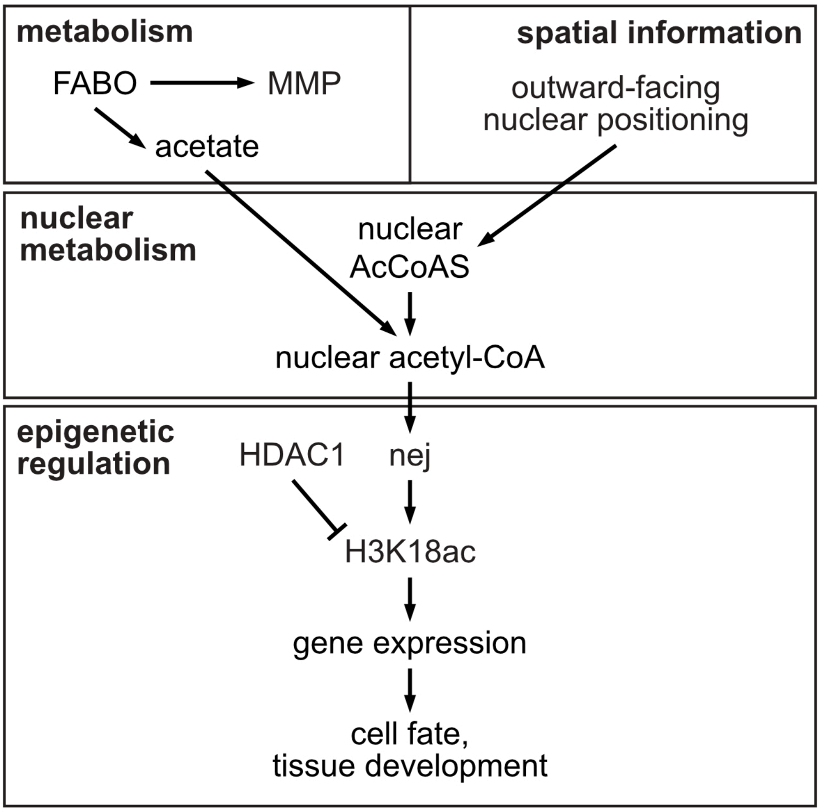

Fig. 77: Nuclear positioning and a non-uniform metabolism exert epigenetic control of gene expression in the wing disc
This schematic summarizes the data obtained in my PhD project. Spatial cues to nuclei facing the wing disc surface induce nuclear translocation of acetyl-CoA synthase (AcCoAS) which uses acetate to produce nuclear acetyl-CoA. This nuclear pool of acetyl-CoA enables the spatially restricted action of histone acetyltransferase nejire (nej) to modify H3K18 and additional acetylation marks in the rim of the wing disc. This process is counteracted by histone deacetylase 1 (HDAC1). Rim histone acetylation also dependents on a non-uniform metabolism with high fatty acid β-oxidation (FABO) in the rim of the disc generating acetate for use by AcCoAS. Ultimately, the concerted action of nuclear positioning and non-uniform metabolism impacts the epigenome of the developing wing discs, regulating gene expression and, possibly, affecting cell fate and tissue development.

4.2 Nuclear positioning as a regulator of the epigenetic state of a cell

Patterning of complex developmental tissues typically depends on compartment-specific gene expression. For example in the wing disc, expression of Hh or apterous define the posterior or dorsal wing disc compartment, respectively (Fig. 5a)[34,95,96]. In my project, however, I identified a H3K18ac pattern specific to the rim of the disc that is not dependent on classical wing disc compartments or even cell identities. Clonal tracing experiments in the wing disc show that neighboring cells within one disc compartment, separated by only one or two cell cycles, have varying levels of H3K18ac dependent on their nuclear position (Fig. 15). Furthermore, genetic ablation of the entire proximal wing disc compartment, encompassing most of the cells with high H3K18ac, causes the formation of a new acetylation rim from previously non-proximal cells (Fig. 16).

One developmentally important process that regulates cell function in neighboring cells within the same compartment of the wing disc is the cell cycle. Among other processes, it affects nuclear localization within a cell or levels of histone phosphorylation[24,25,97,98]. However, in the case of histone acetylation, the cell cycle has no instructive role in the non-uniform acetylation pattern in the wing disc identified herein. No correlation is seen between cell cycle phase and H3K18ac levels and mitotic cells can have high or low H3K18ac depending on their position within the disc tissue (Fig. 14).

The rim H3K18ac pattern is also likely not determined by the relative position of the nucleus towards mitochondria with high membrane potential, which could provide a local, cytosolic acetate gradient to generate acetyl-CoA for histone acetylation. Mitochondria are uniformly distributed in the wing disc (Fig. 55) and the rim of mitochondria with high membrane potential is broader than the rim pattern of H3K18ac pattern (Fig. 13 and 57). Even though all nuclei with high H3K18ac are close to mitochondria with high membrane potential, such mitochondria are also found in proximity of nuclei with lower H3K18ac (Fig. 56-57).

Jointly, the results above argue that the instructive factor for the non-uniform acetylation pattern in the wing disc is the nuclear position relative to the tissue surface. To the best of my knowledge, such an instructive role of nuclear positioning on the epigenome has not been recognized as yet. One hypothesis, how the nuclear position relative to the tissue surface may be sensed, is the exposure of the nucleus to hemolymph-derived signal(s) (Fig. 78). Conceptually, receptors on hemolymph-exposed cell membranes may bind a hemolymph-derived signaling molecule, generating an inward-facing signaling gradient in the tissue. As nuclei face this gradient depending on their relative position towards the tissue surface, a signaling cascade would be activated that induces histone acetylation, ultimately through the nuclear translocation of AcCoAS. Such a cellular signaling gradient sensed by nuclei is described for Notch in the neuroepithelium. In the neuroepithelium of the zebrafish, displaying an apico-basal Notch gradient, interkinetic nuclear migration causes changing nuclear exposure to Notch regulating cell proliferation and differentiation[31].

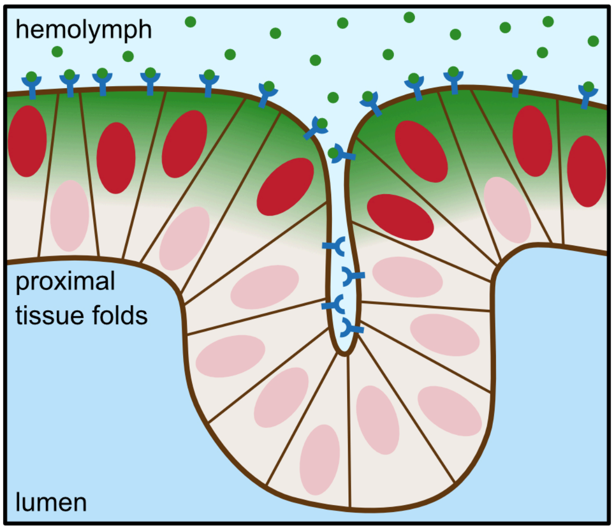

Fig. 78: Hypothetical model of hemolymph-derived signal(s) determining the rim histone acetylation pattern in the wing disc
In my model, the rim histone acetylation pattern in the wing disc is induced by an external signal from the hemolymph (green circle), sensed by receptors (dark blue) on outward-facing cell membranes and translated in an inward-facing cytoplasmic signaling gradient (green). Nuclei in signal-receiving cells, typically in outward-facing proximal folds, are exposed to this signaling gradient as they locate in a position close to the outward-facing cell membrane (e.g., during the cell cycle). In contrast, nuclei from cells less exposed to the hemolymph, typically in inward-facing proximal folds, do not face such a signaling gradient irrespective of their position within the cell. Nuclear exposure to this proposed signaling gradient induces downstream pathways to increase histone acetylation (red) through nuclear translocation of acetyl-CoA synthase (AcCoAS).

My hypothesis of exposure to hemolymph-derived signals as a possible cue for nuclear positioning close to the rim of the wing disc is supported by immunostaining of lpp (Figs. 17-18). Lpp is taken up by wing disc cells from the hemolymph and, hence, can be used as a read-out of hemolymph-exposure. Immunosignals of lpp are enriched on outward-facing cell membranes in close proximity to nuclei with high H3K18ac levels (Figs. 17-18). This correlation even persists in wing discs after formation of a new H3K18ac rim following genetic ablation of the proximal disc compartment (Fig. 19).

The nature of the hemolymph-derived signaling molecule(s) conveying positional information to outward-facing nuclei is presently unknown, but lpp itself may carry such a function. Lpp is the main lipid transporter in the hemolymph that shuttles fatty acids from the fat body to the wing imaginal discs to be used for fatty acid β-oxidation[82]. In addition, lpp serves as a carrier for lipidated morphogens, such as Hh and Wingless[99]. It is intriguing to speculate that cellular uptake of lpp by cells exposed to the hemolymph may provide both metabolites (i.e., fatty acids) as well as signaling molecule(s) to initiate the downstream cascades leading to the observed rim acetylation pattern. To further investigate the relevance of lpp-derived signals, it might be interesting to knock down surface receptors in the proximal wing disc and to analyze the effect on histone acetylation.

4.3 Local acetyl-CoA production by nuclear acetyl-CoA synthase

Acetyltransferases require acetyl-CoA for protein modification. However, fatty acid β-oxidation-derived acetyl-CoA is localized in mitochondria and cannot be directly used for histone acetylation in the nucleus. Rather, it has to be first metabolized to citrate or acetate for mitochondrial export and then re-converted back to acetyl-CoA by ATPCL or AcCoAS, respectively. ACLY, the human ATP citrate lyase orthologue, has been shown to impact histone acetylation levels in human cells[20]. However in *Drosophila*, I identified AcCoAS as the enzyme responsible for generating acetyl-CoA for histone acetylation. Pharmacological inhibition of AcCoAS causes loss of H3K18ac and prevents acetate-dependent rescue of H3K18ac levels upon etomoxir treatment (Figs. 61 and 63). In contrast, knockdown or pharmacological inhibition of ATPCL do not alter H3K18ac levels (Figs. 59 and 61). These findings are supported by the study of Morciano *et al.*[100] that shows decreased total acetyl-CoA levels upon ATPCL knockdown in *Drosophila* but no effect on histone acetylation, raising also the question whether nuclear and cytosolic pools of acetyl-CoA are in fact independent. It has been long believed that only the mitochondrial acetyl-CoA pool is distinct but that cytosolic and nuclear acetyl-CoA pools are common as the cytoplasm is physically linked to the nucleoplasm through nuclear pores, allowing passive diffusion of small metabolites between the two cell compartments. However, a series of recent studies provide evidence for independent acetyl-CoA pools to exist in cytoplasm and nucleus (reviewed in [77,90]). Trefely *et al.*[101] show varying levels of acyl-CoAs in different subcellular compartments including the nucleus using mass spectrometry, suggesting at least partially separated acyl-CoA pools. Furthermore, Sivanand *et al.*[102] verify the requirement of nuclear ACLY localization and activity for histone acetylation involved in DNA damage repair. The concept of metabolically disjointed cytosolic and nuclear compartments is further supported by a growing number of newly identified nuclear metabolic processes (reviewed in [74]). For example, Sun *et al.*[103] confirm the presence of nuclear *de novo* synthesis of glycogen which supports histone acetylation through nuclear glycogenolysis.

Results obtained in my PhD project provide additional support for the existence of disconnected cytosolic and nuclear acetyl-CoA pools. The total ac-K immunosignal is strongly enriched in the rim of the disc, suggesting increased acetyl-CoA levels in this tissue region, but the signal is almost exclusively nuclear (rather than also cytosolic; Figs. 7 and 9). Although the abundance of histones clearly favors immunodetection of nuclear protein acetylation, a joint cytosolic/nuclear acetyl-CoA pool is expected to also increase cytosolic acetylation in the rim. Instead, tubK40ac, as an example of a cytosolic acetylation, does not display a pattern of high acetylation in the rim of the disc as shown for H3K18ac (Fig. 64). The fact that acetate treatment specifically increases acetylation in nuclei facing the tissue surface (Figs. 62 and 65-66) and that nuclear AcCoAS is enriched in these nuclei (Figs. 68-69), further supports the idea of local nuclear conversion of acetate to acetyl-CoA by nuclear AcCoAS. The importance of nuclear translocation of AcCoAS for nuclear acetylation is supported by experimental evidence from several studies[91–93,104]. Takahashi *et al.*[93] show that nuclear Acs2p, the yeast AcCoAS homologue, is required for global histone acetylation and suggest that nuclear acetyl-CoA synthesis is a rate-limiting step in histone acetylation. Li *et al.*[91] document the relevance of nuclear translocation of the human acetyl-CoA synthase orthologue ACSS2 upon nutrient stress to induce lysosomal biogenesis and autophagy through epigenetic control of gene expression.

Conceptually, nuclear translocation of AcCoAS in outward-facing nuclei in the wing disc provides a mechanistic explanation for a connection of the nuclear position with its histone acetylation status. Although the underlying regulatory mechanisms in the wing disc were not elucidated in my project, studies in mammalian cell types provide interesting precedents for mechanisms regulating nuclear ACSS2 localization and activity. Li *et al.*[91] identified an AMP-activated protein kinase-dependent phosphorylation site on ACSS2 that exposes a nuclear localization signal and causes nuclear translocation of the enzyme. Mews *et al.*[92] show recruitment of ACSS2 to chromatin for local acetyl-CoA production that correlates with increased histone acetylation around the bound sites. Interestingly, these authors also document physical interaction between ACSS2 and cyclic adenosine monophosphate response element binding protein (CREB) binding protein, the human orthologue of nej. Such an interaction between AcCoAS and nej may also be relevant for the nej-dependent rim histone acetylation pattern in the wing disc. To identify the *in vivo* translocation signal, future experiments might include generation of AcCoAS variants with phosphomimetic mutations or mutations blocking potential phosphorylation sites and analysis of their subcellular localizations.

4.4 Fatty acid β-oxidation provides the metabolic substrate for rim histone acetylation

As well as non-uniform histone acetylation, I also uncovered that the wing disc is characterized by a non-uniform metabolism with high levels of fatty acid β-oxidation specific to cells in the rim of the disc. This finding suggests a metabolic program aligned with the epigenome in this tissue.

Metabolic reprogramming is a key feature of proliferative cells and growing tissues including tumors. Different metabolic pathways are activated or repressed to balance energetical needs and requirements for biosynthetic building blocks as well as metabolic co-factors and substrates. Proliferative cells have mostly been described to undergo a glycolytic shift allowing for high rates of ATP production as well as high concentrations of metabolic intermediates to maintain growth[1–3]. However, recent studies highlight an important role of fatty acid β-oxidation in growth and survival of stem cells and tumor cells (reviewed in [87,105,106]). Fatty acid β-oxidation has the capacity to sustain high rates of energy production under normal but especially under stress conditions, such as glucose or oxygen deprivation[88,107]. In line with this fact, energy-demanding tissues, like heart or muscles, heavily rely on fatty acid β-oxidation for energy production[88]. Apart from its bioenergetical benefits, fatty acid β-oxidation is also required for the synthesis of co-factors and substrates, especially nicotinamide adenine dinucleotide phosphate (NADPH), which counteracts oxidative stress (reviewed in [87,105,106]). Pike *et al.*[108] show that inhibition of fatty acid β-oxidation decreases NADPH levels causing increased levels of reactive oxygen species and, consequently, cell death in human glioblastoma cells. A similar mechanism was described by Lee *at al.*[109] in leukemia cells. Even though proliferative cells often rely on a glycolytic metabolism, Sullivan *et al.*[110] document the necessity of a certain amount of respiration in these cells to generate electron acceptors for aspartate biosynthesis. Highly glycolytic cells convert pyruvate to lactate to generate NAD^+ required for maximal glycolytic flux, thereby blocking pyruvate to enter the TCA cycle. Under such conditions, fatty acid β-oxidation can fuel the TCA cycle independent of glycolysis to maintain respiration. The emerging role of fatty acid β-oxidation in proliferating cells to provide energy but also metabolic co-factors and substrates is in line with my observations of increased fatty acid β-oxidation in the rim of the wing disc required to sustain high levels of histone acetylation (Figs. 43-47). More distal cells of the wing disc lack a high mitochondrial membrane potential indicating low rates of oxidative phosphorylation (Figs. 49-50, 53, and 57). This observation suggests energy production in these cells mainly through glycolysis, likely to support rapid growth of the tissue. The requirement of glycolysis for maintaining the fast growth of the larva has been shown by Tennessen *et al.*[4].

My observations that H3K18ac is dependent both on fatty acid β-oxidation (Figs. 43-45) to produce acetyl-CoA and on the (nuclear) conversion of acetate to acetyl-CoA by AcCoAS (Figs. 61 and 63) raise the question, how fatty acid β-oxidation-derived acetyl-CoA is metabolized to acetate. One possible mechanism is acetyl-CoA hydrolysis to acetate by the mitochondrial acetyl-CoA hydrolase. This mechanism was shown in porcine and rat livers[111–113]. Lin *et al.*[111] furthermore show that acetyl-CoA hydrolysis in porcine liver releases CoA required for maintaining a high rate of fatty acid β-oxidation. Additionally, Yamashita *et al.*[112] document activation of acetyl-CoA hydrolase by NADH but inhibition by CoA in rat liver. Hypothetically, a similar regulatory mechanism may exist in the rim of the wing disc with high fatty acid β-oxidation flux increasing acetyl-CoA and NADH levels while decreasing the concentration of free CoA. This consequently activates the acetyl-CoA hydrolase to produce acetate used by the AcCoAS to drive histone acetylation.

4.5 Epigenetic control of developmentally important genes by rim histone acetylation

Epigenetic marks, such as histone acetylation and methylation, modulate gene expression. In particular, histone acetylation increases transcription by reducing chromatin compaction and by recruiting transcriptional co-activators to gene regulatory regions[12,13]. This fact raised the interesting hypothesis that the rim histone acetylation pattern, identified in this project, may serve to control gene expression in the developing wing disc. I confirmed this assumption by analyzing the genomic distribution of H3K18ac using Cut&Run as well as by determining its transcriptional effect using FISH. As previously described for histone acetylation[11], H3K18ac peaks, as analyzed by Cut&Run, are mostly localized in promoter regions, particularly in proximal promoters (≤ 1 kb; Fig. 71b), supporting a possible role for this histone mark in gene expression control. Many H3K18ac peaks do not change upon inhibition of fatty acid β-oxidation but the ones, that display altered H3K18ac levels upon etomoxir treatment, mostly decrease (Fig. 71c). These decreasing peaks are likely located in nuclei in the rim of the disc, as etomoxir treatment specifically reduces rim acetylation. In line with these observations, I show that expression of exemplary genes depends on nej activity, as enzyme knockdown causes strongly decreased transcript levels (Figs. 74-76). In contrast, H3K18ac peaks not impacted by inhibition of fatty acid β-oxidation likely represent basic H3K18ac marks present throughout the entire disc.

Conceptually, histone acetylation in the rim of the disc may serve to globally increase gene transcription by reducing chromatin condensation, a mechanism that may enable the disc to swiftly adapt gene expression profiles to the demands of tissue growth and morphogenesis. Histone acetylation as a general promoter of transcription has been documented in yeast and during early differentiation of human and mouse embryonic stem cells[93,114]. This function of histone acetylation is supported by my findings, that, additionally to non-uniform histone acetylation, also euchromatin-associated H3K36me3 is slightly enriched in rim of the disc while heterochromatin-associated H3K9me2 shows an inverse pattern (Figs. 7 and 9-11).

More exciting might be the alternative explanation that fatty acid β-oxidation-dependent H3K18ac peaks control expression of a specific set of genes, essential to guide wing disc development. Histone acetylation has been shown to control genes involved in growth, replication, and metabolism (reviewed in[90]). In line with this function, my GO enrichment analysis of genes with fatty acid β-oxidation-dependent H3K18ac peaks includes genes involved in tissue development, regulation of gene expression, as well as signal transduction (Fig. 73). Fittingly, increased H3K18ac and H4K8ac in the rim of the disc is present throughout wing disc development (Fig. 8). Furthermore, knockdown of nej strongly decreases wing disc size (Fig. 20). In detail, GO enrichment analysis identifies components of several signaling pathways involved in tissue patterning and development to have fatty acid β-oxidation-depend H3K18ac peaks (Fig. 73). These pathways include Hippo, Notch, MAPK, and Hh. Especially Hippo signaling is an interesting target as it senses cues from mechanical forces appearing in growing tissues to regulate cell proliferation. Furthermore, it has been shown that mechanical stresses, such as compression or stretching, depend on the position of a cell in the tissue and that Hippo signaling can affect fatty acid β-oxidation[33,35,115].

4.6 Nuclear positioning as a novel regulator of the epigenome – a perspective

In my study, I have identified the physical position of a nucleus within a tissue as a novel regulator of its epigenetic state, a process that requires metabolic co-regulation. Based on my findings, I propose this mechanism to provide spatial control of gene expression in the developing wing disc, specifying cell fate and regulating tissue development. Conceptually, this novel regulatory process may not be restricted to the control of tissue growth during normal development but could also be relevant for aberrant tissue growth as tumors display atypical tissue architecture and undergo metabolic reprogramming[1,116,117]. Furthermore, misregulated histone acetylation causing irregular gene expression has been linked to cancer development and progression (reviewed in[118–120]). Thus, further studies may not only be directed at understanding the regulatory role of nuclear positioning in the epigenetic control of tissue development but also of tumor formation.

5. Abbreviations

ac	acetylation
ac-K	acetylated lysine
AcCoAS	*Drosophila* acetyl-CoA synthase
acetyl-CoA	acetyl coenzyme A
ACLY	human ATP citrate lyase
ACSS2	human acetyl-CoA synthase
ACSS2i	ACSS2 inhibitor
Acs2p	yeast acetyl-CoA synthase
AFG	actin flip-out GAL4
AMP	adult muscle precursors
ap	apterous
ATP	Adenosine triphosphate
ATPCL	*Drosophila* ATP citrate lyase
BBT	PBS containing 0.3% Triton and 5% BSA
BODIPY	boron-dipyrromethene
CREB	cyclic adenosine monophosphate response element binding protein
crot	crotonylation
Cut&Run	cleavage under targets and release using nuclease
Cy5	cyanine 5
DAPI	4′,6-diamidino-2-phenylindole
DON	6-diazo-5-oxo-L-norleucin
dpp	decapentapleigic
drm	drumstick
Elp3	Elongator complex protein 3
FA	formaldehyde
FABO	fatty acid β-oxidation
FAD	flavin adenine dinucleotide
FCCP	carbonyl cyanide-p-trifluoromethoxyphenylhydrazone
FDR	false discovery rate
FISH	fluorescent *in situ* hybridization
FITC	fluorescein isothiocyanate

G4	GAL4
G80	GAL80
G80^{ts}	temperature-sensitive GAL80
Gapdh2	glyceraldehyde 3 phosphate dehydrogenase 2
Gcn5	general control non-repressed protein 5
GFP	green fluorescent protein
GO	gene ontology
grn	grain
H3	histone 3
H3K18	histone 3 lysine 18
H3K27	histone 3 lysine 27
H3K36	histone 3 lysine 36
H3K9	histone 3 lysine 9
H4K8	histone 4 lysine 8
HAT	histone acetyltransferase
HDAC	histone deacetylase
HDM	histone demethylase
hh	hedgehog
HMT	histone methyltransferase
HS	hybridization buffer
hsFLP	heat-shock-inducible flipase
hth	homothorax
IFP	infra-red protein
IIS	insulin/insulin-like growth factor signaling
L3	third-instar larval stage
LDH	lactate dehydrogenase
lpp	lipoprotein
mamo	maternal gene required for meiosis
MAPK	mitogen-activated protein kinase
me1	mono-methylation
me2	di-methylation
me3	tri-methylation
mirr	mirror
mitoGFP	mitochondrially-targeted GFP

MNase	micrococcal nuclease
MPC	mitochondrial pyruvate carrier
NAD	nicotinamide adenine dinucleotide
NADP	nicotinamide adenine dinucleotide phosphate
NAM	nicotinamide
nej	nejire
nt	nucleotide
OAA	oxaloacetate
p	p value
PB	panobinostat
PBS	phosphate-buffered saline
PBTr	PBS containing 0.3% Triton
PBTw	PBS containing 0.1% Tween-20
PDH	pyruvate dehydrogenase
PDHa	pyruvate dehydrogenase α
PDK	pyruvate dehydrogenase kinase
pH3 S10	phospho-histone 3 serine 10
pPDH S293	phospho-pyruvate dehydrogenase serine 293
RNAi	RNA interference
SAM	S-adenosyl methionine
Sirt	sirtuin
Sox15	Sox box protein 15
split	splitomicin
TCA	tricarboxylic acid
TMRM	tetramethylrhodamine-methylester
TRITC	tetramethylrhodamine
TSA	trichostatin A
tsh	teashirt
tub	tubulin
tubK40ac	α-tubulin lysine 40 acetylation
UAS	upstream activating sequence
vol	volume
w	weight
wg	wingless

zfh2	Zn finger homeodomain 2
αKG	α-ketoglutarate
968	glutaminase inhibitor 968
2DG	2-deoxy-glucose

6. References

1. DeBerardinis RJ, Lum JJ, Hatzivassiliou G, Thompson CB. The biology of cancer: metabolic reprogramming fuels cell growth and proliferation. *Cell Metab*. 2008;7(1):11-20. doi:10.1016/j.cmet.2007.10.002

2. Locasale JW, Cantley LC. Metabolic flux and the regulation of mammalian cell growth. *Cell Metab*. 2011;14(4):443-451. doi:10.1016/j.cmet.2011.07.014

3. Lunt SY, Vander Heiden MG. Aerobic Glycolysis: Meeting the Metabolic Requirements of Cell Proliferation. *Annu Rev Cell Dev Biol*. 2011;27(1):441-464. doi:10.1146/annurev-cellbio-092910-154237

4. Tennessen JM, Baker KD, Lam G, Evans J, Thummel CS. The Drosophila estrogen-related receptor directs a metabolic switch that supports developmental growth. *Cell Metab*. 2011;13(2):139-148. doi:10.1016/j.cmet.2011.01.005

5. Jang H, Yang J, Lee E, Cheong JH. Metabolism in embryonic and cancer stemness. *Arch Pharm Res*. 2015;38(3):381-388. doi:10.1007/s12272-015-0558-y

6. Shyh-Chang N, Ng HH. The metabolic programming of stem cells. *Genes Dev*. 2017;31(4):336-346. doi:10.1101/gad.293167.116

7. Suda T, Takubo K, Semenza GL. Metabolic regulation of hematopoietic stem cells in the hypoxic niche. *Cell Stem Cell*. 2011;9(4):298-310. doi:10.1016/j.stem.2011.09.010

8. Ryall JG, Dell'Orso S, Derfoul A, et al. The NAD(+)-dependent SIRT1 deacetylase translates a metabolic switch into regulatory epigenetics in skeletal muscle stem cells. *Cell Stem Cell*. 2015;16(2):171-183. doi:10.1016/j.stem.2014.12.004

9. Bulusu V, Prior N, Snaebjornsson MT, et al. Spatiotemporal Analysis of a Glycolytic Activity Gradient Linked to Mouse Embryo Mesoderm Development. *Dev Cell*. 2017;40(4):331-341.e4. doi:10.1016/j.devcel.2017.01.015

10. Figlia G, Willnow P, Teleman AA. Metabolites Regulate Cell Signaling and Growth via Covalent Modification of Proteins. *Dev Cell*. 2020;54(2):156-170. doi:10.1016/j.devcel.2020.06.036

11. Zhou VW, Goren A, Bernstein BE. Charting histone modifications and the functional organization of mammalian genomes. *Nat Rev Genet*. 2011;12(1):7-18. doi:10.1038/nrg2905

12. Nitsch S, Zorro Shahidian L, Schneider R. Histone acylations and chromatin dynamics: concepts, challenges, and links to metabolism. *EMBO Reports*. 2021;22(7). doi:10.15252/embr.202152774

13. Kouzarides T. Chromatin Modifications and Their Function. *Cell*. 2007;128(4):693-705. doi:10.1016/j.cell.2007.02.005

14. Liu J, Kim J, Oberdoerffer P. Metabolic modulation of chromatin: implications for DNA repair and genomic integrity. *Front Genet*. 2013;4. doi:10.3389/fgene.2013.00182

15. Martinez-Pastor B, Cosentino C, Mostoslavsky R. A tale of metabolites: the cross-talk between chromatin and energy metabolism. *Cancer Discov*. 2013;3(5):497-501. doi:10.1158/2159-8290.CD-13-0059

16. Smith BC, Denu JM. Chemical mechanisms of histone lysine and arginine modifications. *Biochim Biophys Acta*. 2009;1789(1):45-57. doi:10.1016/j.bbagrm.2008.06.005

17. Teperino R, Schoonjans K, Auwerx J. Histone methyl transferases and demethylases; can they link metabolism and transcription? *Cell Metab*. 2010;12(4):321-327. doi:10.1016/j.cmet.2010.09.004

18. Dokmanovic M, Clarke C, Marks PA. Histone Deacetylase Inhibitors: Overview and Perspectives. *Molecular Cancer Research*. 2007;5(10):981-989. doi:10.1158/1541-7786.MCR-07-0324

19. Yamamoto H, Schoonjans K, Auwerx J. Sirtuin Functions in Health and Disease. *Molecular Endocrinology*. 2007;21(8):1745-1755. doi:10.1210/me.2007-0079

20. Wellen KE, Hatzivassiliou G, Sachdeva UM, Bui TV, Cross JR, Thompson CB. ATP-citrate lyase links cellular metabolism to histone acetylation. *Science*. 2009;324(5930):1076-1080. doi:10.1126/science.1164097

21. McDonnell E, Crown SB, Fox DB, et al. Lipids Reprogram Metabolism to Become a Major Carbon Source for Histone Acetylation. *Cell Reports*. 2016;17(6):1463-1472. doi:10.1016/j.celrep.2016.10.012

22. Zhang D, Tang Z, Huang H, et al. Metabolic regulation of gene expression by histone lactylation. *Nature*. 2019;574(7779):575-580. doi:10.1038/s41586-019-1678-1

23. Sabari BR, Zhang D, Allis CD, Zhao Y. Metabolic regulation of gene expression through histone acylations. *Nat Rev Mol Cell Biol*. 2017;18(2):90-101. doi:10.1038/nrm.2016.140

24. Gundersen GG, Worman HJ. Nuclear Positioning. *Cell*. 2013;152(6):1376-1389. doi:10.1016/j.cell.2013.02.031

25. Meyer EJ, Ikmi A, Gibson MC. Interkinetic Nuclear Migration Is a Broadly Conserved Feature of Cell Division in Pseudostratified Epithelia. *Curr Biol*. 2011;21(6):485-491. doi:10.1016/j.cub.2011.02.002

26. Spear PC, Erickson CA. Interkinetic nuclear migration: A mysterious process in search of a function. *Develop Growth Differ*. 2012;54(3):306-316. doi:10.1111/j.1440-169X.2012.01342.x

27. Lee HO, Norden C. Mechanisms controlling arrangements and movements of nuclei in pseudostratified epithelia. *Trends in Cell Biology*. 2013;23(3):141-150. doi:10.1016/j.tcb.2012.11.001

28. Cagan R. Principles of Drosophila Eye Differentiation. *Curr Top Dev Biol*. 2009;89:115-135. doi:10.1016/S0070-2153(09)89005-4

29. Nikolopoulou E, Galea GL, Rolo A, Greene NDE, Copp AJ. Neural tube closure: cellular, molecular and biomechanical mechanisms. *Development*. 2017;144(4):552-566. doi:10.1242/dev.145904

30. Kosodo Y, Suetsugu T, Suda M, et al. Regulation of interkinetic nuclear migration by cell cycle-coupled active and passive mechanisms in the developing brain. *EMBO J*. 2011;30(9):1690-1704. doi:10.1038/emboj.2011.81

31. Del Bene F, Wehman AM, Link BA, Baier H. Regulation of Neurogenesis by Interkinetic Nuclear Migration through an Apical-Basal Notch Gradient. *Cell*. 2008;134(6):1055-1065. doi:10.1016/j.cell.2008.07.017

32. Klein T. Wing disc development in the fly: the early stages. *Current Opinion in Genetics & Development*. 2001;11(4):470-475. doi:10.1016/S0959-437X(00)00219-7

33. Shingleton AW. The regulation of organ size in Drosophila: physiology, plasticity, patterning and physical force. *Organogenesis*. 2010;6(2):76-87.

34. Beira JV, Paro R. The legacy of Drosophila imaginal discs. *Chromosoma*. 2016;125(4):573-592. doi:10.1007/s00412-016-0595-4

35. Hariharan IK. Organ Size Control: Lessons from Drosophila. *Dev Cell*. 2015;34(3):255-265. doi:10.1016/j.devcel.2015.07.012

36. Diaz de la Loza MC, Thompson BJ. Forces shaping the Drosophila wing. *Mech Dev*. 2017;144(Pt A):23-32. doi:10.1016/j.mod.2016.10.003

37. Aldaz S, Escudero LM, Freeman M. Live imaging of Drosophila imaginal disc development. *Proc Natl Acad Sci U S A*. 2010;107(32):14217-14222. doi:10.1073/pnas.1008623107

38. Irvine KD, Harvey KF. Control of organ growth by patterning and hippo signaling in Drosophila. *Cold Spring Harb Perspect Biol*. 2015;7(6). doi:10.1101/cshperspect.a019224

39. Bryant PJ. Pattern formation in the imaginal wing disc of Drosophila melanogaster: Fate map, regeneration and duplication. *J Exp Zool*. 1975;193(1):49-77. doi:10.1002/jez.1401930106

40. Cadigan KM. Regulating morphogen gradients in the Drosophila wing. *Seminars in Cell & Developmental Biology*. 2002;13(2):83-90. doi:10.1016/S1084-9521(02)00014-9

41. Ashe HL, Briscoe J. The interpretation of morphogen gradients. *Development*. 2006;133(3):385-394. doi:10.1242/dev.02238

42. Burke R, Basler K. Dpp receptors are autonomously required for cell proliferation in the entire developing Drosophila wing. *Development*. 1996;122(7):2261-2269.

43. Martín-Castellanos C, Edgar BA. A characterization of the effects of Dpp signaling on cell growth and proliferation in the Drosophila wing. *Development*. 2002;129(4):1003-1013.

44. Staley BK, Irvine KD. Warts and Yorkie mediate intestinal regeneration by influencing stem cell proliferation. *Curr Biol*. 2010;20(17):1580-1587. doi:10.1016/j.cub.2010.07.041

45. Staley BK, Irvine KD. Hippo signaling in Drosophila: recent advances and insights. *Dev Dyn*. 2012;241(1):3-15. doi:10.1002/dvdy.22723

46. Enderle L, McNeill H. Hippo gains weight: added insights and complexity to pathway control. *Sci Signal*. 2013;6(296):re7. doi:10.1126/scisignal.2004208

47. Kannan K, Fridell YWC. Functional implications of Drosophila insulin-like peptides in metabolism, aging, and dietary restriction. *Front Physiol*. 2013;4:288. doi:10.3389/fphys.2013.00288

48. Brogiolo W, Stocker H, Ikeya T, Rintelen F, Fernandez R, Hafen E. An evolutionarily conserved function of the Drosophila insulin receptor and insulin-like peptides in growth control. *Curr Biol*. 2001;11(4):213-221.

49. Böhni R, Riesgo-Escovar J, Oldham S, et al. Autonomous control of cell and organ size by CHICO, a Drosophila homolog of vertebrate IRS1-4. *Cell*. 1999;97(7):865-875.

50. Puig O, Marr MT, Ruhf ML, Tjian R. Control of cell number by Drosophila FOXO: downstream and feedback regulation of the insulin receptor pathway. *Genes Dev*. 2003;17(16):2006-2020. doi:10.1101/gad.1098703

51. Goberdhan DC, Paricio N, Goodman EC, Mlodzik M, Wilson C. Drosophila tumor suppressor PTEN controls cell size and number by antagonizing the Chico/PI3-kinase signaling pathway. *Genes Dev*. 1999;13(24):3244-3258.

52. Walkiewicz MA, Stern M. Increased Insulin/Insulin Growth Factor Signaling Advances the Onset of Metamorphosis in Drosophila. *PLoS ONE*. 2009;4(4):e5072. doi:10.1371/journal.pone.0005072

53. Oldham S, Stocker H, Laffargue M, Wittwer F, Wymann M, Hafen E. The Drosophila insulin/IGF receptor controls growth and size by modulating PtdInsP(3) levels. *Development*. 2002;129(17):4103-4109.

54. Brand AH, Perrimon N. Targeted gene expression as a means of altering cell fates and generating dominant phenotypes. *Development*. 1993;118(2):401-415.

55. Duffy JB. GAL4 system in drosophila: A fly geneticist's swiss army knife. *genesis*. 2002;34(1-2):1-15. doi:10.1002/gene.10150

56. Suster ML, Seugnet L, Bate M, Sokolowski MB. Refining GAL4-driven transgene expression in Drosophila with a GAL80 enhancer-trap. *genesis*. 2004;39(4):240-245. doi:10.1002/gene.20051

57. Lee T, Luo L. Mosaic analysis with a repressible cell marker for studies of gene function in neuronal morphogenesis. *Neuron*. 1999;22(3):451-461. doi:10.1016/s0896-6273(00)80701-1

58. McGuire SE, Mao Z, Davis RL. Spatiotemporal gene expression targeting with the TARGET and gene-switch systems in Drosophila. *Sci STKE*. 2004;2004(220):pl6. doi:10.1126/stke.2202004pl6

59. Strassburger K, Teleman AA. Protocols to Study Growth and Metabolism in Drosophila. In: *Drosophila*. Methods in Molecular Biology. Humana Press, New York, NY; 2016:279-290. doi:10.1007/978-1-4939-6371-3_17

60. Ermakova YG, Pak VV, Bogdanova YA, et al. SypHer3s: a genetically encoded fluorescent ratiometric probe with enhanced brightness and an improved dynamic range. *Chem Commun*. 2018;54(23):2898-2901. doi:10.1039/C7CC08740C

61. Belousov VV, Fradkov AF, Lukyanov KA, et al. Genetically encoded fluorescent indicator for intracellular hydrogen peroxide. *Nat Methods*. 2006;3(4):281-286. doi:10.1038/nmeth866

62. Bischof J, Maeda RK, Hediger M, Karch F, Basler K. An optimized transgenesis system for *Drosophila* using germ-line-specific φC31 integrases. *Proc Natl Acad Sci USA*. 2007;104(9):3312-3317. doi:10.1073/pnas.0611511104

63. Eugster C, Panáková D, Mahmoud A, Eaton S. Lipoprotein-Heparan Sulfate Interactions in the Hh Pathway. *Dev Cell*. 2007;13(1):57-71. doi:10.1016/j.devcel.2007.04.019

64. Skene PJ, Henikoff S. An efficient targeted nuclease strategy for high-resolution mapping of DNA binding sites. *eLife*. 2017;6:e21856. doi:10.7554/eLife.21856

65. Ahmad K, Spens AE. Separate Polycomb Response Elements control chromatin state and activation of the vestigial gene. Cavalli G, ed. *PLoS Genet*. 2019;15(8):e1007877. doi:10.1371/journal.pgen.1007877

66. Skene PJ, Henikoff JG, Henikoff S. Targeted in situ genome-wide profiling with high efficiency for low cell numbers. *Nat Protoc*. 2018;13(5):1006-1019. doi:10.1038/nprot.2018.015

67. Afgan E, Baker D, Batut B, et al. The Galaxy platform for accessible, reproducible and collaborative biomedical analyses: 2018 update. *Nucleic Acids Research*. 2018;46(W1):W537-W544. doi:10.1093/nar/gky379

68. Langmead B, Trapnell C, Pop M, Salzberg SL. Ultrafast and memory-efficient alignment of short DNA sequences to the human genome. *Genome Biol*. 2009;10(3):R25. doi:10.1186/gb-2009-10-3-r25

69. Langmead B, Salzberg SL. Fast gapped-read alignment with Bowtie 2. *Nat Methods*. 2012;9(4):357-359. doi:10.1038/nmeth.1923

70. Feng J, Liu T, Qin B, Zhang Y, Liu XS. Identifying ChIP-seq enrichment using MACS. *Nat Protoc*. 2012;7(9):1728-1740. doi:10.1038/nprot.2012.101

71. Zhang Y, Liu T, Meyer CA, et al. Model-based Analysis of ChIP-Seq (MACS). *Genome Biol*. 2008;9(9):R137. doi:10.1186/gb-2008-9-9-r137

72. Ross-Innes CS, Stark R, Teschendorff AE, et al. Differential oestrogen receptor binding is associated with clinical outcome in breast cancer. *Nature*. 2012;481(7381):389-393. doi:10.1038/nature10730

73. Yu G, Wang LG, He QY. ChIPseeker: an R/Bioconductor package for ChIP peak annotation, comparison and visualization. *Bioinformatics*. 2015;31(14):2382-2383. doi:10.1093/bioinformatics/btv145

74. Boon R, Silveira GG, Mostoslavsky R. Nuclear metabolism and the regulation of the epigenome. *Nat Metab*. 2020;2(11):1190-1203. doi:10.1038/s42255-020-00285-4

75. Cai L, Sutter BM, Li B, Tu BP. Acetyl-CoA Induces Cell Growth and Proliferation by Promoting the Acetylation of Histones at Growth Genes. *Mol Cell*. 2011;42(4):426-437. doi:10.1016/j.molcel.2011.05.004

76. Wellen KE, Hatzivassiliou G, Sachdeva UM, Bui TV, Cross JR, Thompson CB. ATP-Citrate Lyase Links Cellular Metabolism to Histone Acetylation. *Science*. 2009;324(5930):1076-1080. doi:10.1126/science.1164097

77. Sivanand S, Viney I, Wellen KE. Spatiotemporal Control of Acetyl-CoA Metabolism in Chromatin Regulation. *Trends in Biochemical Sciences*. 2018;43(1):61-74. doi:10.1016/j.tibs.2017.11.004

78. Zhou VW, Goren A, Bernstein BE. Charting histone modifications and the functional organization of mammalian genomes. *Nat Rev Genet*. 2011;12(1):7-18. doi:10.1038/nrg2905

79. Kirkland NJ, Yuen AC, Tozluoglu M, Hui N, Paluch EK, Mao Y. Tissue Mechanics Regulate Mitotic Nuclear Dynamics during Epithelial Development. *Curr Biol*. 2020;30(13):2419-2432.e4. doi:10.1016/j.cub.2020.04.041

80. Goyal L, McCall K, Agapite J, Hartwieg E, Steller H. Induction of apoptosis by Drosophila reaper, hid and grim through inhibition of IAP function. *EMBO J*. 2000;19(4):589-597. doi:10.1093/emboj/19.4.589

81. Tait SWG, Werner AB, de Vries E, Borst J. Mechanism of action of Drosophila Reaper in mammalian cells: Reaper globally inhibits protein synthesis and induces apoptosis independent of mitochondrial permeability. *Cell Death Differ*. 2004;11(8):800-811. doi:10.1038/sj.cdd.4401410

82. Palm W, Sampaio JL, Brankatschk M, et al. Lipoproteins in Drosophila melanogaster—Assembly, Function, and Influence on Tissue Lipid Composition. P. Kühnlein R, ed. *PLoS Genet*. 2012;8(7):e1002828. doi:10.1371/journal.pgen.1002828

83. Close P, Hawkes N, Cornez I, et al. Transcription Impairment and Cell Migration Defects in Elongator-Depleted Cells: Implication for Familial Dysautonomia. *Mol Cell*. 2006;22(4):521-531. doi:10.1016/j.molcel.2006.04.017

84. Kristjuhan A, Walker J, Suka N, et al. Transcriptional Inhibition of Genes with Severe Histone H3 Hypoacetylation in the Coding Region. *Mol Cell*. 2002;10(4):925-933. doi:10.1016/S1097-2765(02)00647-0

85. Xue-Franzén Y, Henriksson J, Bürglin TR, Wright AP. Distinct roles of the Gcn5 histone acetyltransferase revealed during transient stress-induced reprogramming of the genome. *BMC Genomics*. 2013;14(1):479. doi:10.1186/1471-2164-14-479

86. Kelly RDW, Chandru A, Watson PJ, et al. Histone deacetylase (HDAC) 1 and 2 complexes regulate both histone acetylation and crotonylation in vivo. *Sci Rep*. 2018;8(1):14690. doi:10.1038/s41598-018-32927-9

87. Carracedo A, Cantley LC, Pandolfi PP. Cancer metabolism: fatty acid oxidation in the limelight. *Nat Rev Cancer*. 2013;13(4):227-232. doi:10.1038/nrc3483

88. Houten SM, Violante S, Ventura FV, Wanders RJA. The Biochemistry and Physiology of Mitochondrial Fatty Acid β-Oxidation and Its Genetic Disorders. *Annu Rev Physiol*. 2016;78(1):23-44. doi:10.1146/annurev-physiol-021115-105045

89. Longo N, Frigeni M, Pasquali M. Carnitine transport and fatty acid oxidation. *Biochimica et Biophysica Acta (BBA) - Mol Cell Research*. 2016;1863(10):2422-2435. doi:10.1016/j.bbamcr.2016.01.023

90. Pietrocola F, Galluzzi L, Bravo-San Pedro JM, Madeo F, Kroemer G. Acetyl Coenzyme A: A Central Metabolite and Second Messenger. *Cell Metab*. 2015;21(6):805-821. doi:10.1016/j.cmet.2015.05.014

91. Li X, Yu W, Qian X, et al. Nucleus-Translocated ACSS2 Promotes Gene Transcription for Lysosomal Biogenesis and Autophagy. *Mol Cell*. 2017;66(5):684-697.e9. doi:10.1016/j.molcel.2017.04.026

92. Mews P, Donahue G, Drake AM, Luczak V, Abel T, Berger SL. Acetyl-CoA synthetase regulates histone acetylation and hippocampal memory. *Nature*. 2017;546(7658):381-386. doi:10.1038/nature22405

93. Takahashi H, McCaffery JM, Irizarry RA, Boeke JD. Nucleocytosolic Acetyl-Coenzyme A Synthetase Is Required for Histone Acetylation and Global Transcription. *Mol Cell*. 2006;23(2):207-217. doi:10.1016/j.molcel.2006.05.040

94. Wang Z, Zang C, Rosenfeld JA, et al. Combinatorial patterns of histone acetylations and methylations in the human genome. *Nat Genet*. 2008;40(7):897-903. doi:10.1038/ng.154

95. Tabata T. Genetics of morphogen gradients. *Nat Rev Genet*. 2001;2(8):620-630. doi:10.1038/35084577

96. Michel M, Dahmann C. Regulating mechanical tension at compartment boundaries in Drosophila. *Fly (Austin)*. 2016;10(4):204-209. doi:10.1080/19336934.2016.1207028

97. Rossetto D, Avvakumov N, Côté J. Histone phosphorylation: a chromatin modification involved in diverse nuclear events. *Epigenetics*. 2012;7(10):1098-1108. doi:10.4161/epi.21975

98. Hans F, Dimitrov S. Histone H3 phosphorylation and cell division. *Oncogene*. 2001;20(24):3021-3027. doi:10.1038/sj.onc.1204326

99. Panáková D, Sprong H, Marois E, Thiele C, Eaton S. Lipoprotein particles are required for Hedgehog and Wingless signalling. *Nature*. 2005;435(7038):58-65. doi:10.1038/nature03504

100. Morciano P, Di Giorgio ML, Porrazzo A, et al. Depletion of ATP-Citrate Lyase (ATPCL) Affects Chromosome Integrity Without Altering Histone Acetylation in Drosophila Mitotic Cells. *Front Physiol*. 2019;10:383. doi:10.3389/fphys.2019.00383

101. Trefely S, Lovell CD, Snyder NW, Wellen KE. Compartmentalised acyl-CoA metabolism and roles in chromatin regulation. *Molecular Metabolism*. 2020;38:100941. doi:10.1016/j.molmet.2020.01.005

102. Sivanand S, Rhoades S, Jiang Q, et al. Nuclear Acetyl-CoA Production by ACLY Promotes Homologous Recombination. *Mol Cell*. 2017;67(2):252-265.e6. doi:10.1016/j.molcel.2017.06.008

103. Sun RC, Dukhande VV, Zhou Z, et al. Nuclear Glycogenolysis Modulates Histone Acetylation in Human Non-Small Cell Lung Cancers. *Cell Metab*. 2019;30(5):903-916.e7. doi:10.1016/j.cmet.2019.08.014

104. Xu M, Nagati JS, Xie J, et al. An acetate switch regulates stress erythropoiesis. *Nat Med*. 2014;20(9):1018-1026. doi:10.1038/nm.3587

105. Ma Y, Temkin SM, Hawkridge AM, et al. Fatty acid oxidation: An emerging facet of metabolic transformation in cancer. *Cancer Lett*. 2018;435:92-100. doi:10.1016/j.canlet.2018.08.006

106. Qu Q, Zeng F, Liu X, Wang QJ, Deng F. Fatty acid oxidation and carnitine palmitoyltransferase I: emerging therapeutic targets in cancer. *Cell Death Dis*. 2016;7:e2226. doi:10.1038/cddis.2016.132

107. Casals N, Zammit V, Herrero L, Fadó R, Rodríguez-Rodríguez R, Serra D. Carnitine palmitoyltransferase 1C: From cognition to cancer. *Prog Lipid Res*. 2016;61:134-148. doi:10.1016/j.plipres.2015.11.004

108. Pike LS, Smift AL, Croteau NJ, Ferrick DA, Wu M. Inhibition of fatty acid oxidation by etomoxir impairs NADPH production and increases reactive oxygen species resulting in ATP depletion and cell death in human glioblastoma cells. *Biochimica et Biophysica Acta (BBA) - Bioenergetics*. 2011;1807(6):726-734. doi:10.1016/j.bbabio.2010.10.022

109. Lee EA, Angka L, Rota SG, et al. Targeting Mitochondria with Avocatin B Induces Selective Leukemia Cell Death. *Cancer Res*. 2015;75(12):2478-2488. doi:10.1158/0008-5472.CAN-14-2676

110. Sullivan LB, Gui DY, Hosios AM, Bush LN, Freinkman E, Vander Heiden MG. Supporting Aspartate Biosynthesis Is an Essential Function of Respiration in Proliferating Cells. *Cell*. 2015;162(3):552-563. doi:10.1016/j.cell.2015.07.017

111. Lin X, Shim K, Odle J. Carnitine palmitoyltransferase I control of acetogenesis, the major pathway of fatty acid {beta}-oxidation in liver of neonatal swine. *Am J Physiol Regul Integr Comp Physiol*. 2010;298(5):R1435-1443. doi:10.1152/ajpregu.00634.2009

112. Yamashita H, Kaneyuki T, Tagawa K. Production of acetate in the liver and its utilization in peripheral tissues. *Biochim Biophys Acta*. 2001;1532(1-2):79-87. doi:10.1016/s1388-1981(01)00117-2

113. Yamashita H, Itsuki A, Kimoto M, Hiemori M, Tsuji H. Acetate generation in rat liver mitochondria; acetyl-CoA hydrolase activity is demonstrated by 3-ketoacyl-CoA thiolase. *Biochim Biophys Acta*. 2006;1761(1):17-23. doi:10.1016/j.bbalip.2006.01.001

114. Moussaieff A, Rouleau M, Kitsberg D, et al. Glycolysis-mediated changes in acetyl-CoA and histone acetylation control the early differentiation of embryonic stem cells. *Cell Metab*. 2015;21(3):392-402. doi:10.1016/j.cmet.2015.02.002

115. Watt KI, Henstridge DC, Ziemann M, et al. Yap regulates skeletal muscle fatty acid oxidation and adiposity in metabolic disease. *Nat Commun*. 2021;12(1):2887. doi:10.1038/s41467-021-23240-7

116. Almagro J, Messal HA, Elosegui-Artola A, van Rheenen J, Behrens A. Tissue architecture in tumor initiation and progression. *Trends Cancer*. 2022;8(6):494-505. doi:10.1016/j.trecan.2022.02.007

117. Pavlova NN, Thompson CB. The Emerging Hallmarks of Cancer Metabolism. *Cell Metab*. 2016;23(1):27-47. doi:10.1016/j.cmet.2015.12.006

118. Audia JE, Campbell RM. Histone Modifications and Cancer. *Cold Spring Harb Perspect Biol*. 2016;8(4):a019521. doi:10.1101/cshperspect.a019521

119. Dawson MA, Kouzarides T. Cancer epigenetics: from mechanism to therapy. *Cell*. 2012;150(1):12-27. doi:10.1016/j.cell.2012.06.013

120. Timmermann S, Lehrmann H, Polesskaya A, Harel-Bellan A. Histone acetylation and disease. *Cell Mol Life Sci*. 2001;58(5-6):728-736. doi:10.1007/pl00000896

7. Own publications

During the course of my PhD project, I co-authored the following publications:

Bageritz J, Willnow P, Valentini E, Leible S, Boutros M, Teleman AA. Gene expression atlas of a developing tissue by single cell expression correlation analysis. *Nat Methods*. 2019;16(8):750-756. doi:10.1038/s41592-019-0492-x

Figlia G, Willnow P, Teleman AA. Metabolites Regulate Cell Signaling and Growth via Covalent Modification of Proteins. *Dev Cell*. 2020;54(2):156-170. doi:10.1016/j.devcel.2020.06.036

8. Acknowledgements

Foremost, I wish to thank my supervisor Prof. Dr. Aurelio Teleman for the opportunity to work on this exciting project in his laboratory. I would like to express my sincere gratitude for his guidance, insightful scientific discussions, and his commitment to my work during my PhD studies.

I also wish to thank Prof. Dr. Michael Boutros and Prof. Dr. Rüdiger Hell for acting as members in my thesis advisory committee providing guidance and valuable input to my ongoing work.

I am grateful to the Heidelberg Biosciences International Graduate School for supporting my work with a PhD fellowship.

I want to thank the current and past members of the Teleman laboratory for the wonderful experience of working with such dedicated researchers and of enjoying this unique collegial working environment. I would like to specifically thank Dr. Julieta Acevedo for her mentorship during my Master's thesis and the introduction into the world of *Drosophila* as well as Sandra Müller for her help in the generation of transgenic fly lines. I also wish to thank Dr. Gianluca Figlia, Fabiola Garcia, Dr. Hana Nůsková, and Mykola Roiuk for their support and many great memories.

Last but not least, I want to thank my wife Antonia and my family. Without their support and affection this work would not have been possible.